COMPUTATIONAL DISCOVERY OF METAL-ORGANIC FRAMEWORKS FOR SEPARATIONS OF ORGANIC MOLECULES

A Thesis
Presented to
The Academic Faculty

by

Jason A. Gee

In Partial Fulfillment
of the Requirements for the Degree
Doctor of Philosophy in the
School of Chemical & Biomolecular Engineering

Georgia Institute of Technology
August 2015

Copyright © 2015 by Jason A. Gee

COMPUTATIONAL DISCOVERY OF METAL-ORGANIC FRAMEWORKS FOR SEPARATIONS OF ORGANIC MOLECULES

Approved by:

Dr. David S. Sholl, Advisor
School of Chemical and Biomolecular Engineering
Georgia Institute of Technology

Dr. Yoshiaki Kawajiri
School of Chemical and Biomolecular Engineering
Georgia Institute of Technology

Dr. Sankar Nair
School of Chemical and Biomolecular Engineering
Georgia Institute of Technology

Dr. Thomas Orlando
School of Chemistry and Biochemistry
Georgia Institute of Technology

Dr. Krista S. Walton
School of Chemical and Biomolecular Engineering
Georgia Institute of Technology

Date Approved: May 20, 2015

To the Gee family for their love and support.

ACKNOWLEDGEMENTS

I would first like to thank my academic advisor, Dr. David Sholl, for his guidance during my thesis. I feel fortunate to have had an advisor that constantly challenged my technical ability and encouraged me to push the limits of the practical insight that could be gleaned from our modeling work. His mentorship went well beyond our typical research talks to constructive advice on how to improve my technical writing and speaking abilities, manage a research project, and develop my career. I am truly inspired by his moral character and ability to master many different scientific topics and I am grateful to have had this opportunity to learn from him.

I also feel fortunate to have had the opportunity to work with several leaders in the field of chemical separations during my time at Georgia Tech. I would like to thank Dr. Krista Walton, Dr. Yoshiaki Kawajiri, and Dr. Thomas Orlando for their helpful suggestions throughout my thesis. I would especially like to thank Dr. Sankar Nair for his experimental collaborations and support. He introduced me to some of the challenges associated with experimental work and his unique perspective greatly influenced the relevance of this work to practical applications.

I must also express gratitude to my undergraduate research advisor and professor, Dr. Scott Shell at the University of California Santa Barbara, for introducing me to scientific research and molecular modeling. I greatly appreciate his patience and understanding during the beginning of my research career and his inspiration to continue my education in graduate school.

I also appreciate the education and support provided by the School of Chemical and Biomolecular Engineering at Georgia Tech. The research program and facilities at Tech are some of the finest in the world and they provided me ample opportunities to expand my knowledge of chemical engineering. This work would also not have been possible without the generous support provided by ExxonMobil Chemical Company and many helpful discussions with Dr. Meha Rungta and Dr. Jeevan Abichandani.

During my time at Georgia Tech, I had the opportunity to work with many great scientists and engineers in the Sholl group. I would specifically like to acknowledge Dr. Taku Watanabe, Dr. Emmanuel Haldoupis, Dr. Ambarish Kulkarni, and Dr. Salah Eddine Boulfelfel for their helpful discussions about science and life in general. I would also like to thank my experimental collaborators, Jaeyub Chung, Dr. Chen Zhang, and Dr. Ke Zhang, for their hard work and insights on the practical aspects of this work.

Finally, I would like to extend the deepest gratitude to my family because I would never have been able to pursue my doctorate without their love and support. Last but certainly not least, I would like to thank my girlfriend Samantha for her motivation and support throughout the rollercoaster ride of graduate school. The time spent we have spent together in Atlanta has been the most enjoyable of my life.

Jason Gee, Atlanta, May 2015

TABLE OF CONTENTS

LIST OF TABLES

Page

LIST OF FIGURES

Page

SUMMARY

The separation of *para*-xylene from a stream of mixed xylenes and ethylbenzene is critical for the large-scale production of plastics in the petrochemical industry. Several groups have identified metal-organic frameworks (MOFs) as having desirable characteristics for this separation. In this thesis, we demonstrate that molecular simulations can be used to efficiently screen large databases of MOFs to identify promising materials for this separation. We validated our approach in conjunction with our experimental collaborators and discovered that two of the top-performing materials from our screening procedure have similar performance to the zeolites used in industrial practice for xylene separations. We also developed a classical force field parameterization approach for refining the interactions between C_8 alkyl aromatic hydrocarbons and MOFs using Density Functional Theory (DFT) calculations. We demonstrate that our DFT-based force field gives better predictions of some adsorption properties than generic force fields.

A major technological hurdle to using small alcohols as biofuels is in their separation from aqueous fermentation broths. To address this issue, we developed classical models to identify hydrophobic MOFs capable of efficiently performing this separation. We were then able to use our models in a different context to understand the factors governing the thermodynamic stability and structural flexibility of MOFs. The methods developed in this thesis provide unique insight into chemical separations and material properties that would be challenging to obtain from experiments and promote the development of MOFs for industrial applications.

CHAPTER 1

INTRODUCTION

1.1 Metal-Organic Frameworks (MOFs)

Metal-organic frameworks (MOFs) are crystalline nanoporous materials consisting of inorganic cations and organic linkers. MOFs have a number of applications in gas storage,[1,2] chemical separations,[3,4] drug delivery,[5] catalysis,[6,7] and molecular sensing.[7,8] In contrast to traditional adsorbents such as activated carbons and zeolites, the dimensionality, pore sizes, and access to open metal sites of MOFs can be adjusted by the appropriate selection of precursors and synthesis conditions. The enormous number of potential MOF structures has resulted in studies focused on screening of large databases of real and hypothetical MOFs for separations of small molecules.[9-13]

An interesting feature of MOFs is that they allow preferential adsorption of xylene isomers. For example, the widely studied MIL-47 material shown in Figure 1.1 is known to preferentially adsorb *ortho*-xylene from a mixture of C_8 aromatic hydrocarbons.[14,15] On the other hand, MIL-125(NH_2)[16] and MAF-X8[17] have been shown to preferentially adsorb *para*-xylene. The separation mechanism of xylene isomers in MOFs has been investigated by viewing adsorbate snapshots taken from simulations. Castillo et al.[15] and Torres-Knoop et al.[17] postulated that the selectivity in these materials is due to the dimensions of the MOF channels which allow for favorable stacking of a single xylene isomer. My aim in this thesis is to provide a quantitative explanation for the mechanism of *para*-xylene adsorption in the top-performing MOFs using molecular simulations.

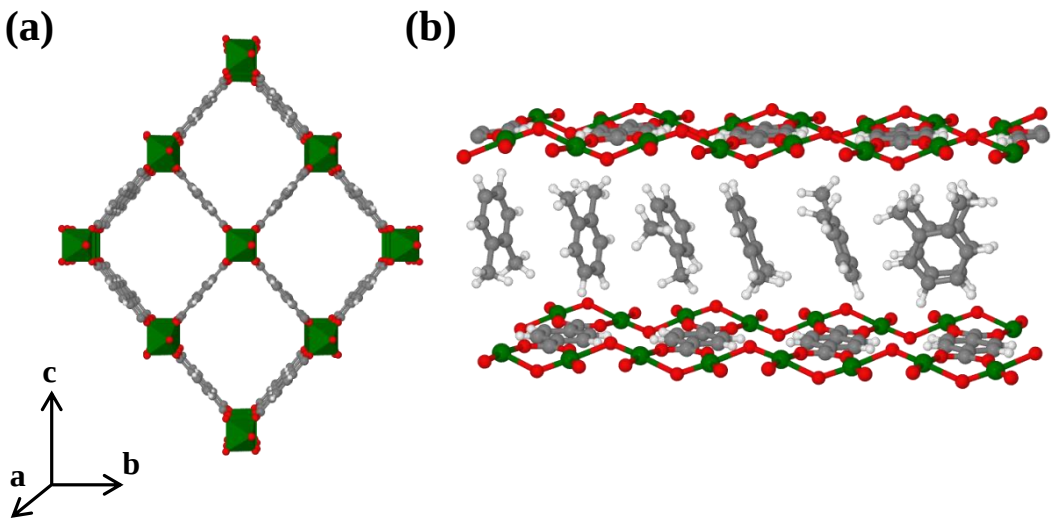

Figure 1.1 (a) Perspective view of the MIL-47 framework and (b) simulated snapshot of *ortho*-xylene molecules adsorbed along the 1-D channels of MIL-47. C atoms are shown in gray, H in white, O in red, and V in green.

1.2 Simulations of Adsorption in MOFs

Adsorption isotherms in MOFs are simulated using Grand Canonical Monte Carlo (GCMC).[18] It is typically assumed in these calculations that the MOF framework atoms are fixed at their crystallographic positions to reduce computational cost. The non-bonded interactions of the framework atoms are modeled using generic force fields available in the literature. The electrostatic charges of the framework atoms are computed using quantum chemistry calculations on small representative clusters of the MOF or the entire periodic framework. Adsorption isotherms computed employing GCMC with these assumptions have generally given good agreement with corresponding experimental measurements for spherical non-polar adsorbates.[19-21] The computation of adsorption isotherms for larger molecules is challenging because of frequent atomic overlaps with framework atoms during insertion and deletion moves. Such systems require the use of Configurational Bias Monte Carlo (CBMC) to efficiently sample configuration space.[22]

Recent studies have employed CBMC to compute adsorption isotherms of aliphatic[23,24] and aromatic hydrocarbons, including xylene isomers,[15] in MOFs and obtained good agreement with experimental data.

A major challenge in accurately computing adsorption isotherms in nanoporous materials is selecting the appropriate the force field. Some studies have attempted to resolve the ambiguity in the force field selection process by parameterizing force fields using experimental data.[25] However, the transferability of this approach to MOFs with different chemical environments has not been clearly demonstrated. Other studies have used quantum chemistry calculations to parameterize force fields.[26,27] For example, McDaniel et al. generated a force field for ZIFs based on *ab initio* calculations that demonstrated good transferability for the adsorption of CO_2 and N_2 in a series of ZIFs.[27] The initial success of the *ab initio*-based force fields for small molecules underscores the value of exploring these types of methods for generating physically accurate and transferable force fields for more complex molecules in MOFs.

1.3 Simulations of Diffusion in MOFs

It is often useful to measure self-diffusion coefficients to probe the effect of mass transport limitations for chemical separations. Diffusion studies in MOFs typically use molecular dynamics (MD) simulations and generic force fields to simulate the motion of the adsorbate through the pores of the MOF.[28-30] The self-diffusivities obtained from MD simulations can be compared to experimental measurement techniques such as pulsed field gradient NMR (PFG-NMR). Recent combined experiment and simulation studies of

the diffusion of hydrocarbons in MOF-5[31] and CuBTC[32] at low loadings have obtained good agreement between self-diffusivity measurements using MD and PFG-NMR.

In simulations of diffusion in MOFs, it is usually assumed that the framework is rigid throughout the course of the simulation. In the case of larger adsorbates whose sizes are commensurate with the pore openings of the MOF, it is often necessary to explicitly account for framework flexibility to accurately measure diffusion.[33-35] In this case, the appropriate choice of force field for the interactions of the framework is critical to accurately capturing the dynamics of the system. Recent studies in the literature have indicated that using generic force fields to parameterize these terms can often produce conflicting results. For example, Hertäg et al. predicted order of magnitude differences in the diffusivities of methane in ZIF-8 between DREIDING and general AMBER (GAFF) force fields.[34] Other studies that have explicitly parameterized force fields to reproduce experimentally determined structural properties of MOFs have predicted diffusivities that are in closer agreement with experiments compared to generic force fields.[35-37] Although these force fields have provided accurate measurements for simple adsorbates, it is unclear whether these models are transferable to study the diffusion of more complex molecules in MOFs.

1.4 Computational Materials Screening in MOFs

Molecular simulations are a valuable tool for calculating adsorption and diffusion properties of a large number of materials to guide experimental efforts towards the most promising materials. Haldoupis et al.[9] used computational screening to investigate hundreds of MOF and zeolite structures for the kinetic separation of light gases (*e.g.*,

CH_4, H_2) and identified many materials with exceptional separation properties. Wilmer et al.[11] used screening to probe a database of ~138,000 hypothetical MOFs for methane storage applications. These authors discovered several hundred materials with predicted methane storage capacities greater than any known material and experimentally confirmed their simulated predictions for a top-performing material**.** Dubbeldam et al. screened a database of MOFs and zeolites and identified a MOF that is predicted to out-perform the existing zeolite for separating linear and branched alkanes by nearly two orders of magnitude.[38] Torres-Knoop et al. used screening to identify a MOF with a predicted xylene capacity that is several times higher than the existing zeolite BaX.[17] Although simulations have identified materials that are predicted to have enhanced performance compared to the state-of-the-art materials, studies in which the candidate materials have been evaluated using experiments are rare.

1.5 Industrial Separation of *para*-Xylene from C_8 Aromatics

The separation of *para*-xylene from a mixture of C_8 alkyl aromatic hydrocarbons is an important intermediate step in the large-scale production of polyethylene terephthalate (PET) in the petrochemical industry.[39] This separation is difficult due to the close boiling points of the C_8 aromatics which makes separation by distillation infeasible. The state-of-the-art technology used in industry for this separation is the UOP Parex® process.[40] The Parex® process is an adsorption-based separation process that exploits the enhanced adsorption selectivity of cation-exchanged faujasite-type zeolites for *para*-xylene.[41] The aim of this project is use molecular simulations to find MOFs with similar or better performance compared to the existing zeolite for this separation.

1.6 Thesis Summary

The objective is this work is to use computational modeling to discover MOFs with exceptional performance for a given chemical separation. This thesis will specifically focus on the industrial separation of *para*-xylene from a mixture of C_8 aromatic hydrocarbons. In Chapter 2, we present an extension of a method developed by Fang et al.[26] to parameterize a force field for C_8 aromatics in MOFs based on adsorption energies calculated using periodic DFT. We show that our force field gives better agreement with experiments for some adsorption properties of C_8 aromatics compared to generic models. In Chapter 3, we develop a materials screening methodology using molecular simulations to identify MOFs for the industrial separation of *para*-xylene. We validate our methodology by comparing to experimental data generated by our experimental collaborators at Georgia Tech. We find that the top-performing materials from our screening have similar performance to the zeolite used industrially for xylene separations. We expect that our screening methodology will be useful in identifying MOFs and zeolites for other chemical separations.

Next, we shift our attention to the technologically-relevant separation of small alcohols in MOFs. In Chapter 4, we validate the applicability of molecular simulations to identify MOFs capable of efficiently separating small alcohols. We also demonstrate the use of flexible framework models to study the adsorption and diffusion of small alcohols. We then extend these flexible models in Chapters 5-6 to understand the factors governing the thermodynamic stability and structural transitions of MOFs under solvothermal conditions.

Finally, we discuss the outlook of using molecular simulations as a tool for screening MOFs for chemical separations in Chapter 7. In this thesis, we demonstrate that molecular simulations can provide insight into chemical separations and material properties that would be challenging to obtain from experiments and promote the development of MOFs for industrial applications.

CHAPTER 2

PREDICTION OF ADSORPTION PROPERTIES OF CYCLIC HYDROCARBONS IN MOFS USING DFT-DERIVED FORCE FIELDS

2.1 Introduction

The separation of C_8 aromatic hydrocarbons is an important step in the large-scale production of plastics in the petrochemical industry. The close boiling points of the xylene isomers (*o*-xylene: 144.5 °C; *m*-xylene: 139.3 °C; *p*-xylene: 138.5 °C at 1 atm[42]) makes it difficult to separate these components using distillation. The state-of-the-art technologies used in industry for this separation are the UOP Parex® and IFP Eluxyl® processes.[43] These processes employ a simulated moving bed (SMB) to separate *p*-xylene from a stream of mixed C_8 aromatics. The zeolite BaX is used as the adsorbent due to its enhanced selectivity towards *p*-xylene at saturation.[44] The development of accurate models to understand and predict adsorption behavior of C_8 aromatics in porous materials is crucial to identifying candidate materials that can improve upon this technology.

Metal-organic frameworks (MOFs) are a class of nanoporous materials composed of inorganic cations and organic linkers. MOFs have a number of potential applications in gas storage, chemical separations, and catalysis.[3] Several experimental studies have investigated the separation of xylene isomers using MOFs. The MOFs MIL-47(V),[14,45] MIL-53(Al),[45] UiO-66,[46,47] HKUST-1,[48] DMOF-1[49] and IRMOF-1[50] have been found to exhibit enhanced adsorption selectivity for *o*-xylene. A recent study by Vermoortele et al. found that MIL-125(NH_2)[51] shows promise for industrial applications due to its high

selectivity towards the *para*- isomer. Although there is considerable interest in using MOFs for this separation, there has not been a critical assessment of the accuracy of modeling to describe experimental adsorption data of C_8 aromatics across a range of MOF materials.

Recent simulation work has focused on using generic force fields to predict the adsorption behavior of C_8 aromatics compared to experimental data in individual MOFs. Castillo et al.[15] used DREIDING[52] to model the framework atoms in MIL-47(V) and found good agreement with experimental adsorption isotherms and heats of adsorption. Granato et al.[53] examined the performance of several generic force fields to predict single- and multi-component adsorption properties of UiO-66. Their study confirmed the experimentally-observed *ortho*-selectivity and heats of adsorption reported for this material. The separation of xylene isomers in HKUST-1 and CPO-27-Ni was investigated computationally by Peralta et al.[48] These authors validated the *ortho*-selectivity observed experimentally for these materials and showed that the origin of this effect is influenced by the topology and electrostatics of the framework. A recent study by Lahoz-Martín et al.[54] examined the adsorption properties of benzene, toluene, ethylbenzene, and xylene mixtures in MOFs using molecular simulations. These authors identified materials that could separate *ortho*- and ethylbenzene from mixtures of cyclic hydrocarbons based on difference in adsorption affinities. Although generic force fields have been shown to provide qualitative agreement with experiments in the cases mentioned above, there has been no effort to reconcile the notable differences between simulations and experiments.

Two strategies have been proposed to develop accurate and transferable classical force fields in MOFs based on either fitting parameters to match experimental adsorption

isotherms or adsorption energies calculated using first-principles-based methods. A comprehensive review on the more general topic of the development of classical force fields in porous materials can be found in Fang et al.[55] Pérez-Pellitero et al. developed a classical force field by directly fitting simulated adsorption isotherms to experimental data in for CO_2, CH_4 and N_2 in zeolitic imidazole frameworks (ZIFs).[25] Although this method was demonstrated to be transferable to other ZIF materials, it is limited by the availability of high quality, reproducible experimental data. On the other hand, first-principles-based force fields do not require experimental data and have been shown to accurately predict the adsorption properties of gases such as H_2, CH_4, H_2O, CO_2, in MOFs.[56-60] These methods usually parameterize classical force fields to the potential energy surface (PES) of a given adsorbate and small fragment of the periodic framework at a level of theory such as density functional theory (DFT) or second-order Møller–Plesset perturbation theory (MP2). Because these methods rely on cluster models of the framework, they can underestimate the effect of long-range dispersive interactions such as π-π stacking that are needed to accurately describe interactions in MOFs. This limitation can be circumvented by employing a periodic model of the framework during the fitting procedure as in the method of Fang et al.[26,61] This method has been shown to accurately describe the adsorption properties of CO_2 in zeolites. To the best of our knowledge, there has been no attempt to develop first-principles-based force fields for aromatic hydrocarbons in MOFs.

The aim of this chapter is to derive force fields to describe the adsorption of C_8 aromatics in MOFs using the method of Fang et al.[23,24] In Section 2.2, we describe our procedure for extending their method to aromatic-containing frameworks and adsorbates

that contain many more degrees of freedom than the original CO_2-zeolite systems. We then use classical Grand Canonical Monte Carlo (GCMC) simulations to predict adsorption properties of C_8 aromatics in several MOFs in Section 2.3. Finally, we assess the accuracy and transferability of our force field by comparing our simulated adsorption data to experimental data from the literature.

2.2 DFT-Derived Force Fields for Cyclic Hydrocarbons in MOFs

In this section we describe our method for developing a transferable force field to describe the adsorption of cyclic hydrocarbons in MOFs based on DFT calculations. We chose to develop our force field for xylene isomers due to their industrial relevance; however the overall method is general to any adsorbed molecule. We began our procedure by generating hundreds of adsorbate configurations in the pores of several periodic MOF structures using a classical force field. The MOFs MIL-47, DMOF-1, UiO-66 and IRMOF-1 were chosen for this test set because they contain the BDC (BDC = 1,4-benzenedicarboxylic acid) linker common to many MOF materials yet contain different framework topologies as shown in Figure 2.1. We simultaneously fit our force field for all four materials to ensure its transferability to other BDC-containing MOFs. We chose toluene as a model adsorbate for the xylene isomers because this molecule was found to accurately represent the interactions of these molecules (see below). The use of toluene greatly reduced the computational expense compared to using all three of the xylene isomers in these calculations. We used an energy biasing procedure[62] for the insertion moves at T = 300 K to ensure that our procedure samples configurations relevant to classical simulations at ambient conditions.

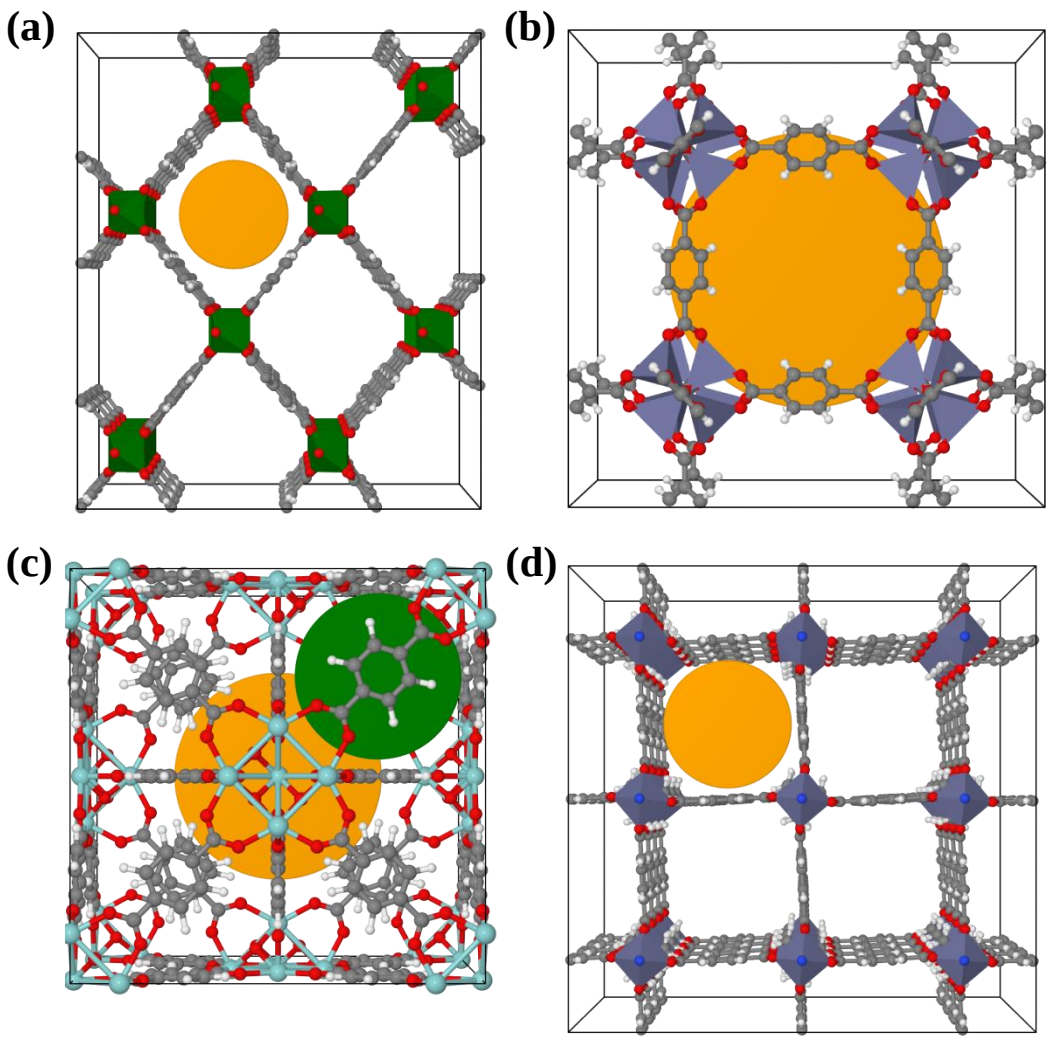

Figure 2.1 Schematics of the MOFs used in in our test set: (a) MIL-47, (b) IRMOF-1, (c) UiO-66, and (d) DMOF-1. The orange spheres are approximately the size of the largest cages in the MOF. The green sphere represents the size of the smaller cages in UiO-66.

The adsorption energy for each configuration was calculated using:

$$E_{ads} = E_{ads/MOF} - (E_{ads} + E_{MOF}) \qquad (2.1)$$

where $E_{ads/MOF}$, E_{ads}, and E_{MOF} are the total energies of the adsorption complex, an isolated adsorbate molecule, and an isolated MOF framework, respectively.

In our initial classical calculations, the interactions between the C_8 aromatics and the framework were modeled using conventional Lennard-Jones (L-J) and Coulomb potentials. The OPLS force field was used to describe non-bonded interactions because this force field accurately describes the bulk phase behavior of aromatic molecules.[63] In this model, the carbon and hydrogen atoms of benzene rings are modeled explicitly and methyl groups ($-CH_3$) are represented by a single pseudo-atom. The Universal Force Field (UFF)[64] was used to describe the framework atoms and the conventional Lorenz-Berthelot mixing rules were used to specify the adsorbate-MOF interactions. L-J interactions were truncated at a spherical cutoff distance of 25 Å for the fitting procedure. The point charges of the framework atoms were calculated for each MOF using the density-derived electrostatic and chemical (DDEC) charge method.[65-67] This method accurately reproduces the electrostatic potential energy surface (EPES) of the periodic MOF framework. Coulombic interactions were calculated using the Ewald summation method with a relative precision of 10^{-6}. The conventional rigid framework approximation was used for the framework atoms in all adsorption calculations. The empty frameworks were energy-minimized prior to these calculations using the methodology described below. The small cages in UiO-66 were assumed to be experimentally accessible to the C_8 aromatics. Previous simulations using similar assumptions have given good agreement with experiments for the adsorption of xylene isomers in MIL-47[15] and UiO-66[53].

To parameterize our force field, we calculated the adsorption energy of the previous configurations using Density Functional Theory (DFT). Prior to all adsorption calculations, the geometry of each framework was energy-minimized using plane wave

DFT calculations as implemented in the Vienna ab initio Simulation Package (VASP).[68,69] The unit cell and atomic positions were allowed to fully relax at an energy cutoff of 520 eV and were considered to be converged if the forces on each atom were <0.03 eV/Å. The geometry optimizations and adsorption energy calculations were performed on conventional (primitive) unit cells for MIL-47 and DMOF-1 (UiO-66 and IRMOF-1). Calculations were performed at the Γ-point for DMOF-1, UiO-66, and IRMOF-1 and using a Monkhorst-Pack grid of 2×1×1 for MIL-47. The experimental and DFT energy-minimized framework lattice constants were found to be in good agreement (see Table A.1). The adsorption energy calculations used the DFT-D3 functional of Grimme et al. to describe dispersion with Becke-Johnson (BJ) damping.[70,71] The DFT-D method was chosen for these calculations because it can capture long-range dispersion interactions such as π-π stacking in aromatic-containing systems.[72] This method was previously used to assess the stacking energy of xylenes in MIL-47.[73].

A force field fitting procedure was performed to determine parameters for the cross-interactions between the toluene molecules and the atoms in the BDC linker of the framework. The metal atoms of all MOFs and the DABCO linker in DMOF-1 (DABCO = 1,4-diazabicyclo[2.2.2]octane) were described using UFF. We assume that using UFF to describe these interactions is reasonable because this force field gives reasonable agreement with DFT-D3 adsorption energies as shown in Figure 2.2 below. We used least-squares fitting to determine the L-J A and B terms to minimize the deviation between the classical and DFT-D3 adsorption energies using:

$$E_{FF}(R_{ij}) = E_{vdW} + E_{Coul} = \frac{A_{ij}}{r_{ij}^{12}} - \frac{B_{ij}}{r_{ij}^{6}} + \frac{q_i q_j}{r_{ij}} \qquad (2.2)$$

where r_{ij} is the distance between atoms i and j, A_{ij} and B_{ij} are the repulsive and attractive L-J coefficients, and q_i and q_j represent the partial atomic charges for atoms i and j, respectively. We found that using unconstrained least-squares fitting produced L-J parameters with purely repulsive ($B_{ij} = 0$) or attractive terms ($A_{ij} = 0$). As an alternative, we found that allowing the L-J parameters to vary within a factor of 4 of their UFF values gave a similar fit to the DFT adsorption energies compared to unconstrained fitting. We used the constrained fitting procedure in our work because it produces L-J parameters that are physically meaningful. We will refer to the force field developed in this way as "D3FF" for the remainder of this work.

The adsorption energies for toluene in four MOFs calculated using UFF and D3FF and compared to DFT-D3 are shown in Figure 2.2. We used 300 configurations of toluene for this analysis because this value was found to give converged results for the isosteric heats of adsorption at infinite dilution in each material (see Figure A.1). The 1,200 adsorption energies span a broad range of energies, from ca. -70 to +20 kJ/mol. The adsorption energies calculated using UFF and DFT-D3 are in good agreement in the low energy region but systematic deviations occur as repulsive interactions become more significant. Although this region does not contribute substantially to low coverage adsorption properties it becomes more significant at higher loadings relevant to practical separation applications. The mean absolute deviation (MAD) between the force field and DFT-D3 adsorption energies are substantially reduced using D3FF compared to UFF (MAD_{D3FF} = 2.98 kJ/mol vs. MAD_{UFF} = 5.82 kJ/mol). We also performed an analysis to ensure that D3FF is transferable to the interactions of the xylene isomers. For this test, we calculated the adsorption energies for *o*-xylene in all four MOFs using D3FF and

compared our results to DFT-D3 adsorption energies. We found that D3FF more accurately represents the interactions of the xylene isomers compared to UFF (MAD_{D3FF} = 3.27 kJ/mol vs. MAD_{UFF} = 5.36 kJ/mol for *o*-xylene). We demonstrate that D3FF is transferable to other BDC-containing MOFs in Section A.2.

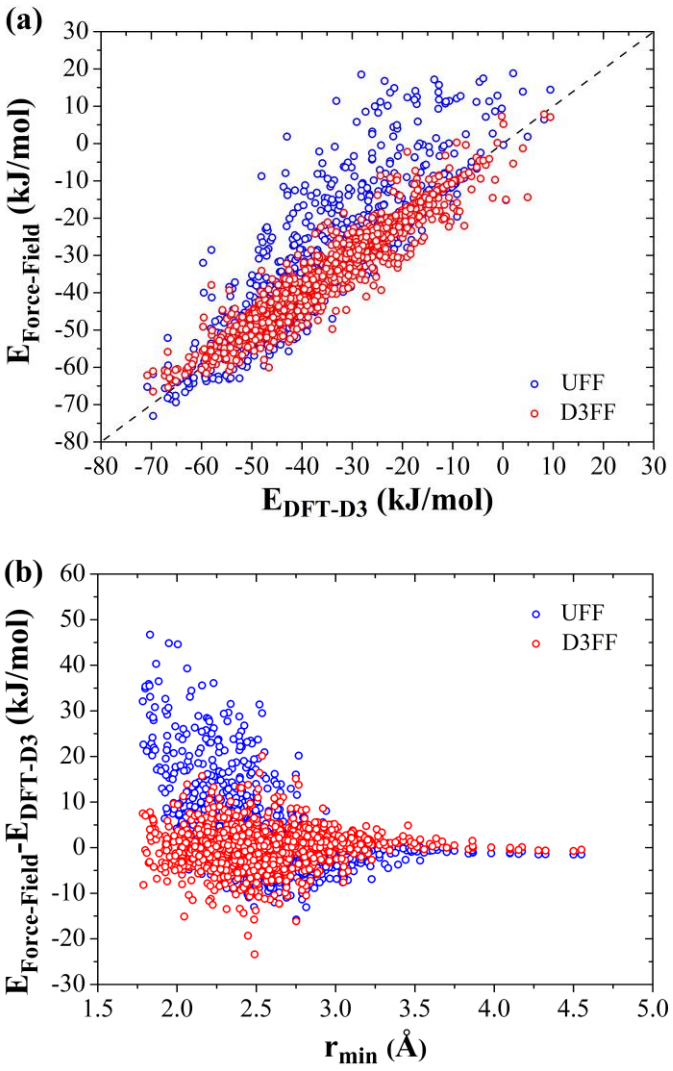

Figure 2.2 (a) Adsorption energies of toluene in MIL-47, DMOF-1, UiO-66 and IRMOF-1 MOFs calculated using D3FF and UFF compared to DFT-D3, (b) difference in adsorption energies ($E_{Force-Field}$-E_{DFT-D3}) as a function of nearest atomic distance between toluene and the MOF.

2.3 Classical Simulations Using DFT-Derived Force Fields

To examine the validity of D3FF, we first compared simulated adsorption properties of the xylene isomers and ethylbenzene in MOFs with experimental values reported in the literature. The first quantity we compared was the heat of adsorption at infinite dilution, Q_{st}^0. Q_{st}^0 is an important adsorption property because it represents interactions of the adsorbate over the entire pore space of the MOF. Fang et al. have discussed why Q_{st}^0 is not identical to the adsorption energy for the lowest energy state of an adsorbed molecule and why averaging a large number of states is necessary to accurately determine Q_{st}^0.[26] The simulated Q_{st}^0 for all systems was computed using the Widom insertion technique.[18,74] The experimental Q_{st}^0 values for MIL-47, UiO-66, and IRMOF-1 were measured using pulse gas chromatography.[45,47,50] The experimental Q_{st}^0 for DMOF-1 were extrapolated by Nicolau et al. to infinite dilution based on adsorption isotherm data measured at high loadings.[49] We found that the presence of strong adsorbate-adsorbate interactions in this system greatly complicates the extrapolation to infinite dilution for this system. Therefore, the effective Q_{st}^0 for this system is represented using the isosteric heat of adsorption (Q_{st}) at the guest loading corresponding to the lowest pressure measured in the adsorption data of Nicolau et al. rather than the extrapolated value**.**

As shown in Figure 2.3, the experimental and simulated (D3FF) Q_{st}^0 are in good agreement, except in the case of IRMOF-1 and DMOF-1. The deviation in IRMOF-1 is likely due to poor sample quality as discussed later. Our simulations predict MADs of 9.7 kJ/mol, 8.1 kJ/mol and 6.9 kJ/mol (excluding IRMOF-1) for UFF, DREIDING, and D3FF, respectively, compared to experiments. These results indicate that the D3FF more

accurately predicts the Q_{st}^0 in these systems. The possible sources for the deviations between simulations and experiments are discussed in detail below.

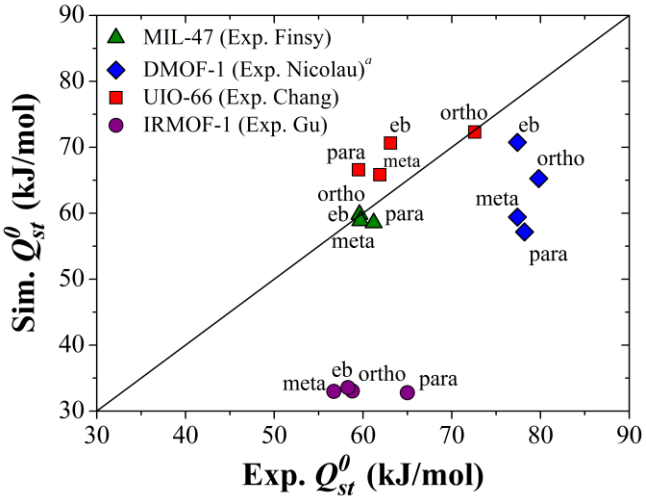

Figure 2.3 Comparison of exp. and sim. (D3FF) heats of adsorption for xylene isomers and ethylbenzene at infinite dilution for different MOF materials. The experimental data are from chromatography experiments of Finsy et al. (T = 543 K) in MIL-47,[45] Chang et al. (T = 423 K) in UiO-66,[47] and Gu et al. (T = 573 K)[50] in IRMOF-1 and adsorption data of Nicolau et al. (T = 423 K)[49] in DMOF-1. Simulations were performed at the same temperatures as the corresponding experiments. [a]The simulated and experimental Q_{st} for DMOF-1 are measured at finite loading.

To elucidate the effect of adsorbate loading on the heat of adsorption, we calculated Q_{st} of *o*-xylene as a function of loading. Q_{st} at finite loading is also an important adsorption property because industrial xylene separations are typically performed under near saturation conditions. The loading-dependent Q_{st} values were calculated using GCMC simulations using the energy/particle fluctuation formula.[75] As shown in Figure 2.4, the *o*-xylene shows a strong loading dependence in all materials, varying by ~35 kJ/mol between infinite dilution and saturation conditions for DMOF-1, IRMOF-1, and MIL-47. This value is similar to the heat of vaporization of *o*-xylene at ambient conditions (ΔH_{vap} = 43.4 kJ/mol)[76]. All of the materials we examined exhibit an increasing heat of adsorption with respect to loading, except for UiO-66. The trend

observed in this system can be explained by strong adsorption sites in the small cages of UiO-66 (see Section 7.2.3A.3). Overall, these results demonstrate that adsorption properties of xylenes change significantly as a function of loading. This effect is important to consider for practical applications due to the high energy requirement to desorb the xylenes at high loadings in some materials.

Figure 2.4 also shows that the simulated Q_{st} at higher loadings are in better agreement with experimental Q_{st}^{0} values for DMOF-1 and IRMOF-1. As mentioned previously, for DMOF-1 this deviation is caused by strong adsorbate-adsorbate interactions at higher loadings that make it invalid to extrapolate these measurements to infinite dilution. The discrepancy in the Q_{st} for IRMOF-1 could be due to incomplete activation or partial degradation of the MOF structure. This observation is supported by the low experimental BET surface area observed for IRMOF-1 in the report of Gu et al. (225 m^2/g)[50] compared to the previous work of Wong-Foy et al. (3534 m^2/g)[77]. It is reasonable to expect that these effects probably account for much of the deviation between simulations and experiments observed in our work.

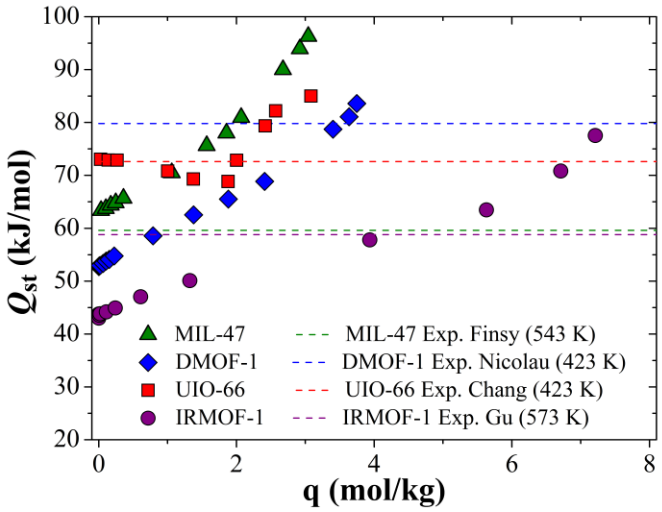

Figure 2.4 Isosteric heat of adsorption (Q_{st}) versus loading for *o*-xylene in several MOFs calculated using D3FF. The experimental heats of adsorption at infinite dilution are shown in dashed lines for comparison.

The adsorption isotherms for the xylene isomers in MIL-47 and DMOF-1 were simulated using D3FF and compared to experimental data from the literature. It is difficult to ascertain the quality of the MOF samples used in these studies as the experimental surface areas were not always reported. In Figure 2.5, we scaled the simulated isotherms for MIL-47 and DMOF-1 to match the experimental saturation loadings for ease of comparison. We compared our results to the highest temperature isotherm data available because most of the literature data do not contain low pressure adsorption uptake due to experimental limitations. As shown in Figure 2.5, the D3FF-simulated isotherms match experiments well, although there is a significant deviation at low loadings for the xylene isomers and ethylbenzene in both MOFs. The causes for these deviations are probably similar to those mentioned previously, but could also be influenced by the experiments not having fully reached equilibrium. The simulated

results at various temperatures and using DREIDING are also found be in reasonable agreement with experiments (see Figure A.3).

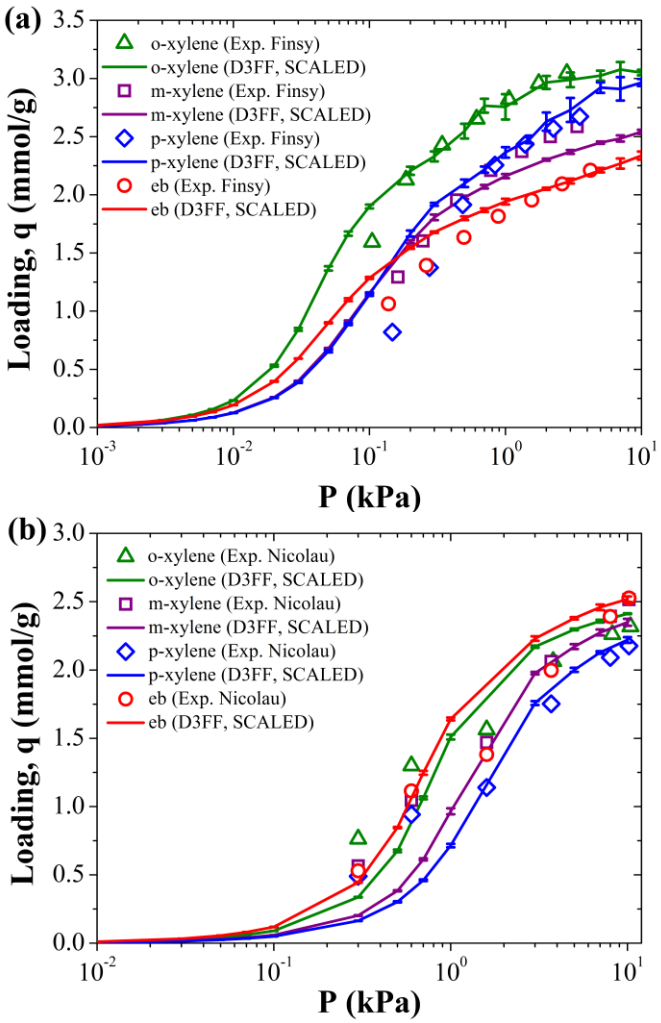

Figure 2.5 Comparison of simulated (D3FF) and experimental adsorption isotherms for xylene isomers in (a) MIL-47 at T = 423 K and (b) DMOF-1 at T = 448 K. The simulated isotherms are scaled to match the saturation loading of the experimental isotherms for comparison.

The binary selectivities for different mixtures of C_8 aromatics were calculated using classical simulations and compared to experimental binary breakthrough data as shown in Figure 2.6. We chose to use binary selectivity data for this comparison because this was the only data available for multiple materials. The selectivities computed with DREIDING give poor quantitative agreement compared to experiments. We found that

generic force fields give better performance than DFT-based force fields in this case, with MADs of 1.9, 1.7, and 2.9 for UFF, DREIDING, and D3FF, respectively. Although both types of force fields only give a qualitative assessment of xylene selectivity in these systems, we envisage that generic force fields can be used as a tool to screen a large number of MOFs and guide experimental efforts. The adsorption properties of the top-performing materials from the screening can then be validated using D3FF prior to experimental evaluation. This level of the screening will also require modeling framework flexibility, as we show below that this effect can cause large differences in xylene selectivities at high loadings in these systems.

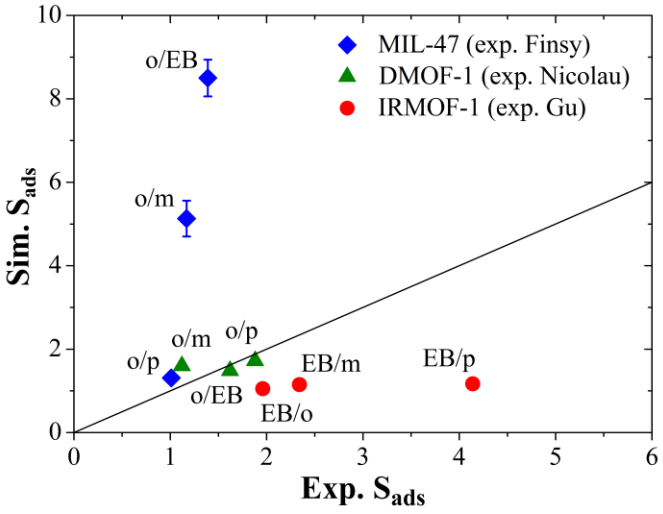

Figure 2.6 Binary selectivities for equimolar mixtures of xylene isomers and ethylbenzene calculated using GCMC simulations with DREIDING and measured using breakthrough experiments. Simulations were performed under the same conditions as the corresponding experiments.

The effect of framework flexibility on calculated xylene selectivities in MOFs has not yet been examined computationally, despite the fact that MIL-47 has been shown to exhibit significant deformation due to the adsorption of some organic molecules.[78,79] An experimental study by Alaerts et al.[14] found that adsorption of the xylene isomers does

not significantly affect the lattice constants of MIL-47. However, it is possible that subtle structural changes to MIL-47 due to xylene adsorption are difficult to resolve in these measurements. Wang et al.[80] found that the adsorption of some six member ring organic molecules cause deformations of the MIL-47 structure. These authors did not examine structural changes due to adsorption of C_8 molecules in their study. However, they found that several structures had similar energies to the parent MIL-47 structure based on single point DFT energy calculations. This result indicates that these structures might be accessible due to the adsorption of similar molecules such as C_8 hydrocarbons.

To elucidate the sensitivity of our selectivity calculations to framework flexibility, we calculated xylene selectivities in one of the crystal structures determined from X-ray diffraction (XRD) in the study of Wang et al.[80] We used the MIL-47(cyclohexane) structure reported in their study because it has a similar cell volume to the empty MIL-47 structure but exhibits a significant twisting of the octahedral chains in the structure. In our work, we found an energy difference of only +2.5 kJ/mol/V atom between the energy-minimized MIL-47 and MIL-47(cyclohexane) structures using DFT-D3. Our results in Figure 2.7 show that the binary selectivities calculated in MIL-47(cyclohexane) are significantly altered compared to the empty MIL-47 structure. Surprisingly, our results show that the simulated selectivities give better agreement with experiments for this system. These results show that small changes in the framework structure at high loadings have a significant impact on C_8 selectivities, and imply that efforts to quantitatively predict high loading selectivities in materials of this kind should consider framework relaxation due to adsorption.

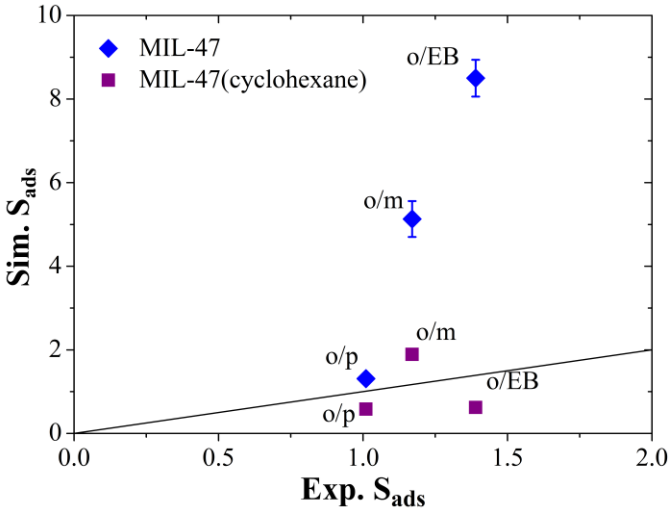

Figure 2.7 Binary selectivities for equimolar mixtures of xylene isomers and ethylbenzene calculated using GCMC simulations with DREIDING in the empty MIL-47 framework and MIL-47(cyclohexene) structures.

2.4 Conclusion

In this chapter, we developed a DFT-based force field to describe the adsorption of C_8 cyclic hydrocarbons in MOFs. We then used this force field to predict several key adsorption properties in these systems using GCMC simulations. We find that the DFT-based force field outperforms generic force fields for predictions for heats of adsorption and single component isotherms compared to experiments. We also observed that generic force fields can provide qualitatively accurate predictions for binary adsorption selectivities compared to breakthrough experiments. This result could be useful for future materials screening of these materials with generic force fields to identify *p*-xylene-selective adsorbents that can outperform the existing zeolite material. We envisage that DFT-based force fields could be used to validate predictions from generic force fields in these systems. Our results also show that several factors can lead to large deviations between experiments and simulations. In particular, we find that modeling framework flexibility must be considered to accurately calculate xylene selectivities at high loadings

in these systems. Our methodology is an important step in obtaining better predictions of the adsorption of C_8 hydrocarbons in MOFs and shed light on unique adsorption behavior observed for these systems.

CHAPTER 3

COMPUTATIONAL IDENTIFICATION AND EXPERIMENTAL EVALUATION OF METAL-ORGANIC FRAMEWORKS FOR XYLENE ENRICHMENT

3.1 Introduction

The separation of xylene isomers is important since *para*-xylene (*p*X), *ortho*-xylene (*o*X), *meta*-xylene (*m*X) and ethylbenzene (EB) have a number of uses as chemical feedstocks/intermediates or as industrial solvents. Particularly, the recovery of pure *p*X is desirable because it is used in the synthesis of terephthalic acid which is the key of precursor for large-scale synthesis of polyesters. However, this separation is difficult because of the close boiling points of the isomers, and is currently either carried out by crystallization or by the PAREX adsorption process.[81] New adsorption-based or membrane-based processes have considerable potential to provide a less complex and more energy-efficient separation. In the case of adsorption, a key issue is to identify an adsorbent that can thermodynamically or kinetically discriminate the C_8 aromatic isomers with selectivity and/or volumetric capacity better than the zeolite BaX used in the PAREX process. In principle, *p*X can be separated from the C8 aromatics mixture by either preferential adsorption or preferential exclusion. However, since *p*X is the minority component (20-25 mol%) in the feed, it is economically more desirable to find adsorbents that can selectively adsorb *p*X.[82]

Metal-organic frameworks (MOFs) are a class of nanoporous materials with crystalline framework structures, and are constructed by coordination bonding between

organic linker molecules and metal nodes.[83-85] There is a rapidly growing interest to explore the unique separation characteristics of MOFs as adsorbents or membranes, due to the large diversity of MOF materials in comparison to other existing nanoporous materials such as zeolites.[86-89] In general, three strategies can be summarized for the identification of MOF adsorbents that may lead to *p*X-selective materials rather than those with the more conventional *o*X-selective characteristics. The first possible method is by molecular sieving separation driven by the difference in molecular sizes of the xylene isomers. If the MOF pores provide a distinct molecular sieving effect, the smaller *p*X molecules (kinetic diameter 0.58 nm) would have faster access into the pores while the intracrystalline diffusion of the larger *o*X and *m*X molecules (kinetic diameter 0.68 nm) is hindered. The second possible method is to identify adsorbents with strongly nonpolar structures wherein the adsorption of *p*X (which has a very small dipole moment) is favored and the effects of electrostatic interaction with the more strongly dipolar *o*X and *m*X are minimized. The third potential method is to exploit entropic effects leading to the preferential packing of the more symmetric *p*X molecules within the confined porous structure at high loadings. The latter strategy may be the most practical of the three, since it is likely to best exploit the differences between *p*X and the other isomers. The industrially applied *p*X-selective FAU-type zeolite adsorbents (BaX and KBaY) operate *via* entropic effects.

In this chapter we focus upon the identification of MOFs with higher selectivity (and ideally also higher volumetric capacity) than FAU zeolites. Molecular simulations have been shown by a number of authors to be a valuable tool for calculating adsorption and diffusion properties of a large database (typically $>10^3$ MOF structures) and thereby

guiding experimental efforts towards the most promising materials. For example, Haldoupis et al.[9] computationally screened hundreds of MOFs and zeolites for kinetic separation of light gases (*e.g.*, CH_4, H_2), and identified many materials with exceptional separation properties. Wilmer et al.[11] constructed and screened a database of approximately 138,000 hypothetical MOFs for methane storage applications, discovered several hundred MOFs with predicted CH_4 storage capacities greater than any known material, and experimentally confirmed their simulated predictions for one top-performing MOF. Dubbeldam et al.[38] screened databases of MOFs and zeolites and identified a MOF that is predicted to out-perform the existing zeolite for separating linear and branched alkanes by nearly two orders of magnitude. Torres-Knoop et al.[17] used screening to identify a MOF with a predicted xylene capacity several times higher than zeolite BaX. Although simulations have identified potential MOFs of interest that are predicted to have enhanced performance, studies in which the candidate materials have been evaluated using experiments are still very few. Here, we first describe the computational screening of a large database of MOFs to identify materials with desirable characteristics for the separation of *p*X from a stream of mixed xylene isomers. We then experimentally evaluate predicted top-performing materials and characterize their desirable properties for this separation through experimental breakthrough measurements and modeling. Besides demonstrating the utility of computationally guided materials synthesis and evaluation, we discuss how our simulations also give useful insight into the mechanisms leading to high *p*-xylene selectivity.

3.2 Methods

3.2.1 Molecular Simulations

Our simulation methodology uses multicomponent Grand Canonical Monte Carlo (GCMC) simulations to calculate the adsorption selectivities of C_8 aromatics in MOFs. The crystal structures of the MOFs used in these calculations are taken from the Computation-Ready, Experimental (CoRE) MOF database[90] which contains ~4,700 MOF structures. We also included a set of commonly known MOFs which are primarly contained in the RASPA simulation package[91] that are not part of the CoRE database. Since we are purely interested in thermodynamically-controlled adsorptive separations in this work, we remove from further consideration any MOFs with pore limiting diameters (PLDs) < 0.4 nm to avoid kinetic (diffusion) limitations. Our simulations are performed with a industrially representative bulk liquid feed mixture[92] at 9 bar pressure and molar composition of 0.33:1:2:1 ethylbenzene/*o*X/*m*X/*p*X. The fugacity of each component is determined from the Peng-Robinson equation of state. Although the industrial feed is typically at a temperature of about 180°C, we performed our calculations at 50°C. These conditions are used because most of the MOF structures in the database are crystallographically determined at ambient or lower temperatures. Our GCMC simulations are performed with RASPA.[91] We use equilibration and production periods of 10^3 Monte Carlo (MC) cycles each. Each cycle consists of attempted adsorbate insertion/deletion, rotation, translation, and identity change moves. Although some error is introduced into our calculations due to the use of a relatively small number of cycles, we show in a following section that the above convergence is sufficient for the high-throughput component of our screening procedure. Then, the predicted top-performing

MOFs are subjected to long-cycle (>10^5 MC cycles) GCMC calculations to ensure highly converged final results. The overall *p*X selectivity (over all the other three components) is calculated from our GCMC simulation data according to the conventional definition:

$$S_{ads} = \left(\frac{q_{px}}{q_{ox} + q_{mx} + q_{eb}}\right)\left(\frac{f_{ox} + f_{mx} + f_{eb}}{f_{px}}\right) \qquad (3.1)$$

where q_i is the amount of component i adsorbed in the framework and f_i is its partial fugacity. The total adsorption capacity for each material is obtained as the sum of the adsorbed amounts of all C_8 components per unit volume and also per unit mass of the bare adsorbent material.

The non-bonded interactions between the C_8 aromatics and the framework are computed using the standard Lennard-Jones potential (L-J). The cross-terms are specified using the Lorenz-Berthelot mixing rules. The L-J potential is truncated at a spherical cutoff distance of 1.2 nm for all calculations. The L-J parameters are taken from the Universal Force Field (UFF)[64] for the framework atoms, and from the TraPPE force field[93] for the adsorbate atoms. The TraPPE force field is selected for the adsorbate atoms because it accurately describes the bulk phase behavior of C_8 aromatics. We note that the TraPPE force field does not explicitly include point charges for these molecules. This significantly reduces the computational time required to predict xylene adsorption properties since it does not require the time-consuming task of determining point charges on framework atoms. Furthermore, Granato et al.[53] have shown that this force field produces good agreement with experiments for C_8 aromatics adsorption in the MOF UiO-66.

3.2.2 MOF Synthesis and Activation[1]

Four predicted top-performing MOF materials (MIL-47, MIL-125-NH_2, MIL-140B, and MOF-48) are synthesized by either solvothermal or hydrothermal methods at temperatures up to 220°C. In a solvothermal synthesis, dimethylformamide (DMF) is usually applied as the solvent. The duration of the synthesis can vary from several hours to several days.[94-97] The as-synthesized MOFs are activated by a combination of solvent exchanges (including a fresh DMF treatment for the removal of excessive ligands) and subsequent methanol exchanges for removal of DMF. In MIL-47, the activation process can be achieved by calcination in air at higher temperatures such as 300°C. It should be noted that an appropriate activation is crucial to open up the microporous spaces that are necessary for the adsorption process. In MIL-47, the activation is highly sensitive to the calcination time, and the appropriate procedure must be accurately carried out.[98] A summary of the MOF synthesis and activation conditions is as follows. **MIL-47**: 1.22 g VCl_3 + 0.32 g terephthalic acid (BDC) + 14 ml H_2O at 200°C for 96 h, molar ratio of V/linker/H_2O = 1/0.25/100. Activation: 300^{o}C calcination in air for 30h. **MIL-125-NH_2**: 60 ml $Ti[OCH(CH_3)_2]_4$ + 55 g 2-amino-BDC + 800 ml DMF + 200 ml methanol at 100°C for 72 h at atmospheric pressures, molar ratio of Ti/linker/DMF/MeOH = 1/15/500/250. Activation: triple "first DMF and then MeOH" exchange at room temperature. **MIL-140B**: 0.70 g $ZrCl_4$ + 1.30 g naphthalene-2,6-dicarboxylic acid + 15 ml DMF + 0.34 ml acetic acid at 220^{o}C for 6 h, molar ratio of Zr/linker/DMF/acetic acid = 1/2/195/2. Activation: one-time "first DMF and then acetone" exchange at room temperature. **MOF-**

[1] All experimental work reported in this chapter was performed by Dr. Ke Zhang in Dr. Sankar Nair's laboratory at Georgia Tech.

48: 0.52 g VO + 1.51 g 2,5-dimethyl terephthalic acid + 14 ml H_2O at 200^oC for 96 h, molar ratio of V/linker/H_2O = 1/1/100. Activation: 300^oC calcination in air for 15h.

3.2.3 Breakthrough Adsorption Experiments and Modeling[2]

Xylene separation experiments are carried out using liquid-phase breakthrough apparatus (schematic shown in Figure S1). The apparatus uses two liquid sources, one filled with the desorbent and the other with the feed mixture, and these sources are connected to computer-controlled syringe pumps A and B respectively. The typical superficial xylene liquid feed velocity is 0.1 ml/min for breakthrough experiments. Desorbent and feed lines are mixed together to obtain the liquid input line which is connected to the adsorbent column inlet. The packed bed column is housed in a well-insulated and ventilated oven which can be heated to up to 400°C. The outlet from the packed bed stream is connected to a back-pressure regulator, which maintains the total pressure in the liquid line at a fixed value (500 psi in this study). The outlet liquid may be sent to the fraction collector directly or to the waste container using a digitally-controlled switch. The fraction collector is programmed to inject small liquid samples from the outlet of the packed bed into 1.5 ml vials. A robotic injector delivers a precise amount of liquid to each vial in a given order. At the end of a breakthrough run, the vials are manually removed from the fraction collector and taken to an autosampling GC for composition analysis. The packed bed is also connected to an inert gas purge line for *in situ* thermal activation and removal of guest molecules from the adsorbent in the packed

[2] All breakthrough modeling reported in this chapter was performed by Souryadeep Bhattacharyya in Dr. Sankar Nair's laboratory at Georgia Tech.

bed. Breakthrough experiments are carried out with four MOF materials selected for experimental investigation based upon the computational screening procedure. For purposes of comparison, a sample of zeolite BaX was also measured. This sample was made at ExxonMobil Chemical Company by exchanging approximately 50% of the Na^+ cations in a zeolite 13X sample (purchased from BASF) with Ba^{2+} cations. The selectivity (as defined by Equation 1) and the capacities are estimated directly from the raw experimental breakthrough curves, as illustrated in previous works.[99]

For a thorough understanding of the breakthrough curves and for more quantitative verification of the separation characteristics estimated from the raw experimental data, we have also carried out a more detailed model-based fitting of the breakthrough curves [100-102]. The model is implemented using gPROMS® Model Builder [42]. Typically, 200 discretization points for the column in the axial domain were found to be sufficient for convergence using a second-order central finite difference method. Two types of parameters, namely the intrinsic adsorption equilibrium coefficients ($K_i = \partial q_i/\partial c_i$) for each component i and a combined dispersion-diffusion parameter, were fitted from the experimental breakthrough data. All the xylenes were assumed to have essentially the same dispersion-diffusion parameter in a particular packed bed. This is because liquid-phase dispersion of each component is expected to be practically identical, and intracrystalline diffusion is not believed to play a significant role considering the PLDs of the MOFs studied, the crystal sizes, and the liquid superficial velocity. The fitted model breakthrough curves are used to obtain the selectivity and capacity in the same manner as obtained from the raw experimental breakthrough curves. The adsorbed

amounts of the xylenes in each adsorbent, as obtained from the fitted breakthrough curves, were corrected for the non-selective volume in the column.

3.3 Results and Discussion

We applied our screening procedure to determine the *p*X selectivity and total xylene capacity for ~2,500 MOFs. Our results in Figure 3.1 show that these MOFs exhibit a wide range of selectivities from almost zero to >100. Indeed, in our entire data set we find that several MOFs are predicted to have nearly perfect *p*X selectivities, although these materials also have vanishingly small capacities. We also find that large pore MOFs exhibit *p*X selectivities close to unity. A notable example is IRMOF-1, which has a total xylene capacity of about 5 mmol/cm^3 and a *p*X selectivity of 0.7. Overall, the screening results demonstrate conclusively that MOFs can exhibit a large range of *p*X selectivities and capacities. This is a promising result in the pursuit of identifying materials that can outperform FAU zeolites for this separation. In particular, the most useful materials would be those with improved selectivities and/or capacities compared to the existing zeolite. Figure 3.1 shows that a number of MOFs are predicted to have desirable characteristics for this separation. We select candidate materials from our data set based on the following criteria: 1) high *p*X selectivity and capacity under the industrial feed conditions, 2) good chemical and thermal stability, and 3) synthesis procedure based on commercially available linkers and metals. The second criterion is included to ensure that the materials could withstand repeated experimental adsorption/desorption cycles, and the last criterion is in view of the desire for straightforward synthesis and reduction of raw material costs. Based upon these criteria, the best-performing *p*X-selective materials are MIL-140B, MOF-48, and MIL-125-NH_2.

Interestingly, MOF-48 is the dimethyl-functionalized version of MIL-47, which is known to possess *o*X-selectivity in a quaternary xylene mixture.[103] The structural differences between the two materials that lead to large differences in their selectivities are discussed in detail later.

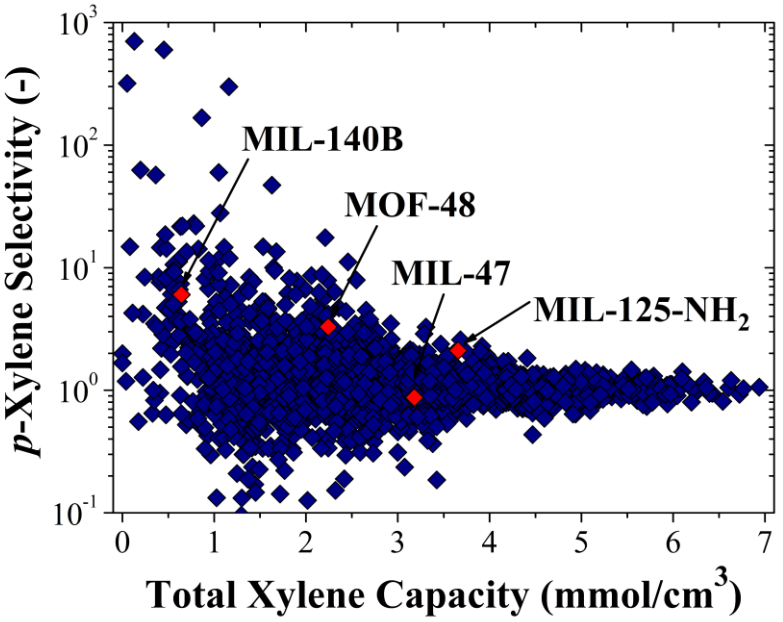

Figure 3.1 *p*-xylene adsorption selectivity versus total xylene capacity for approximately 2,500 MOFs calculated using short 'screening-quality' GCMC simulations for a feed mixture of 0.33:1:2:1 ethylbenzene/*o*-xylene/*m*-xylene/*p*-xylene at 50°C and 9 bar.

As mentioned earlier, we use short Monte Carlo (MC) simulations in our screening procedure to evaluate a large number of materials at reasonable computational expense. To evaluate the convergence of these calculations, we calculate the adsorption selectivity (S_{ads}) as a function of number of MC cycles for a few of these materials. These simulations are performed under the same conditions used for our screening procedure described previously. The S_{ads} was computed using 5 separate simulations for each set number of MC cycles (N_{Cycles} = 1×10^3 - 3×10^5). We selected MIL-125-NH_2, MIL-140B, and MOF-48 for this test because these materials exhibit *p*X selectivity, and also MIL-47

as a material that shows *o*-xylene selectivity. Figure B.2 shows that our screening calculations are well-converged after 10^3 MC cycles for all materials except MIL-140B. We discovered that MIL-140B requires a large number of MC cycles ($>3\times10^5$) to accurately determine its *p*X selectivity due to its low capacity. However, it is also clear that that the *p*X selectivity of MIL-140B is qualitatively captured using the short cycle approach. Our results show that short-cycle simulations can be used to evaluate a large number of materials. They also underscore the importance of verifying the selectivity of top-performing materials with longer GCMC simulations prior to recommending these materials for synthesis.

Figure 3.2 and Table 3.1 summarize the characterization of the synthesized materials MIL-125-NH_2, MIL-140B, and MOF-48, and MIL-47. In Figure 3.2, the XRD patterns of all four materials reveal high crystallinity in the as-made form, as well as maintenance of the crystal structure after the activation processes. In Table 3.1, we show a comparison of experimental and theoretical (geometric) surface areas. In this work, the experimental surface areas are determined by the BET method from the activated materials *via* N_2 physisorption at 77 K. They are also compared with the range of values reported in the previous literature for these MOFs. The theoretical (geometric) surface areas were determined using a N_2 probe radius corresponding to the distance at which the interatomic potential is zero.[104] The simulated pore volumes were calculated using a helium atom probe.[105,106] Our experimental results are in good agreement with the values reported in the previous literature in all cases. Overall, these results show that the synthesized materials exhibit the typical experimental surface areas and pore volumes

reported in the literature and have good sample crystallinity for breakthrough experiments. However, the theoretical values are in good agreement with experiments for MIL-140B and MIL-125-NH_2, but are considerably larger than the experimental values for MIL-47 and MOF-48. Due to the good crystallinity of all our MOF samples, we suspect that this effect in MIL-47 and MOF-48 is more likely due to residual solvent or linkers left over from the synthesis and activation procedures. In these two MOFs with 1-D channels, considerable pore volume blockages could thus occur.

Table 3.1 Comparison of experimental and simulated (geometric) surface areas of the four MOFs selected for synthesis.

MOF	Expt. BET SA (m^2/g) (this work)	Expt. BET SA (m^2/g) (literature)	Sim. SA[104] (m^2/g)	Expt. Pore Volume (cm^3/g)	Sim. Pore Volume (cm^3/g)
MIL-47	755	750[107]-930[78]	1650	0.28	0.61
MIL-125-NH_2	1450	1469[108]	1990	0.61	0.68
MIL-140B	420	460[109]	360	0.17	0.21
MOF-48	195	180[110]	1000	0.08	0.38

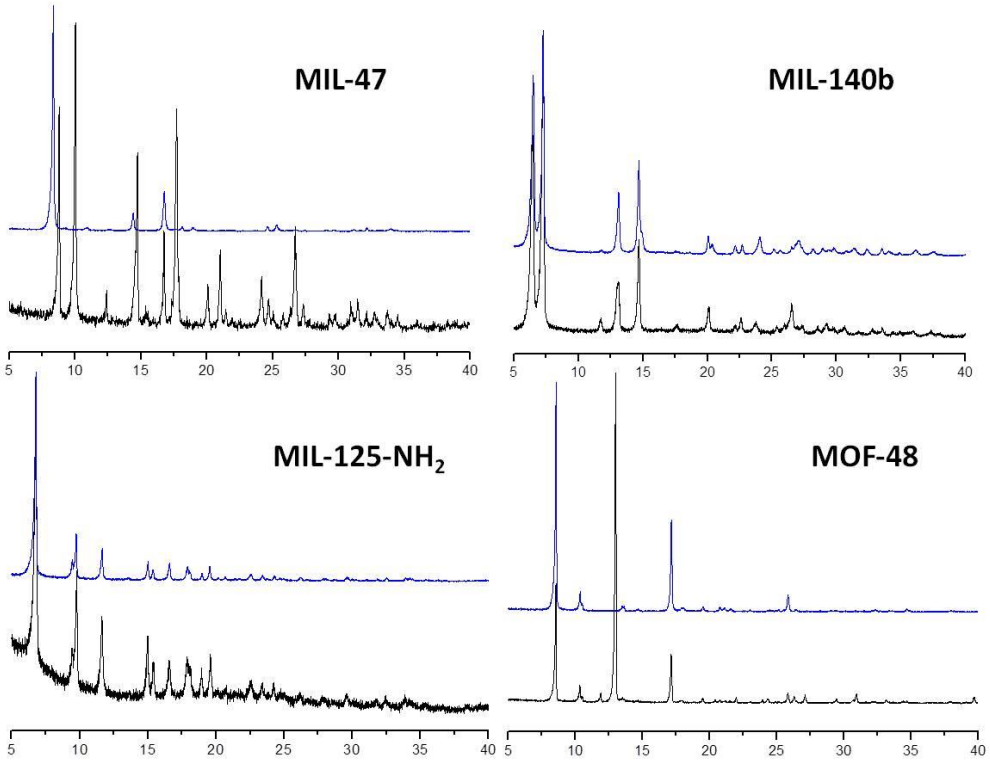

Figure 3.2 X-ray diffraction patterns of the four synthesized materials MIL-47, MIL-125-NH_2, MIL-140B, and MOF-48 before and after activation procedures (Black: as-synthesized; Blue: activated), over a 2Q range of 5-40° and a Cu*K*α x-ray source.

Figure 3.3 shows the experimental breakthrough data and the model-fitted breakthrough curves for the four MOF materials. The corresponding data and model fit for BaX zeolite is shown in Figure B.3. The model was able to accurately fit the breakthrough experimental curves for all the five adsorbents, with the fitted parameters shown in Table B.1. All the breakthrough experiments display comparable values of the dispersion-diffusion parameter *D*, which is in the range of 10^{-7} m^2s^{-1}. All the MOF adsorbents show adsorption coefficient values that are favorable for *p*X selectivity, with the exception of MIL-47 which is *o*X-selective. In the following discussion, we will

compare in detail the separation characteristics obtained from GCMC simulations, raw experimental breakthrough data, and model-fitted breakthrough curves.

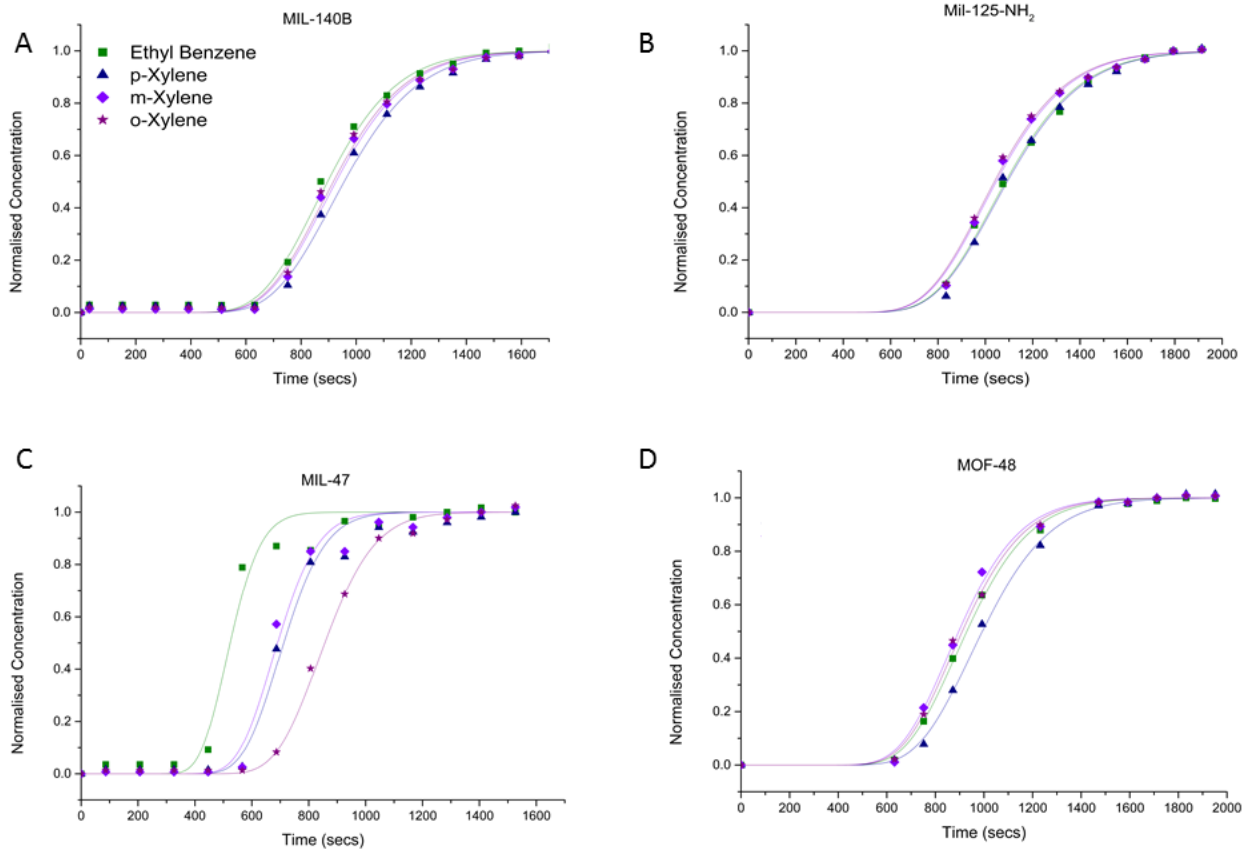

Figure 3.3 Experimental (symbols) and model-fitted (solid lines) breakthrough curves for C_8 isomers in (A) MIL-140B, (B) MIL-125-NH_2 , (C) MIL-47 and (D) MOF-48 at 50ºC and 9 bar at a bulk liquid composition of 0.33:1:2:1 ethylbenzene/*o*-xylene/*m*-xylene/*p*-xylene for MIL-47 and 0.5:1:2:1 ethylbenzene/*o*-xylene/*m*-xylene/*p*-xylene for the other MOFs with a volume flowrate of 0.1 ml/min.

In Table 3.2, we show a detailed comparison of experimental and simulated *p*X selectivities over the other individual components, as well as the total C_8 capacities. The experimental results obtained both from the raw breakthrough data as well as from the model-fitted breakthrough curves are shown. Our simulation and experimental results are in qualitative agreement for *p*X/*m*X and *p*X/*o*X selectivities. The simulated *p*X/EB

selectivities show large deviations from experiment, which is due in part to the low EB loadings in the MOFs. Our simulations also predict capacities for MIL-140B and MIL-47 that are in reasonable agreement with experiments. The GCMC over-prediction of the experimental capacities in MIL-125-NH_2 and MOF-48 is quite likely due to the present difficulty in completely activating these materials, a conclusion that is also supported by the earlier discussion on the crystallinity of the activated MOFs and the comparison of experimental and theoretical surface areas. This observation can be considered as promising, because it suggests that the performance of these computationally selected 'best-performing' materials can be further improved, although in the present study we have not attempted to optimize the synthesis and activation procedures for MIL-125-NH_2 and MOF-48. Figure 3.4 shows a comparison of the overall *p*X selectivities (defined by Equation 3.1) as obtained by GCMC simulations versus those obtained from the raw experimental breakthrough data. Our simulations and experiments were performed at the same bulk fluid temperature; however the bulk pressure was 35 bar in experiments and 9 bar in simulations. In Figure S4 we show that these bulk pressures correspond to approximately the same bulk fugacity, and so the simulation and experimental results are directly comparable. It is clear that the breakthrough experiments are in qualitative agreement with simulations for all the MOFs. The simulations correctly predict the experimentally observed *p*X selectivity in the top-performing MOFs. The deviations found between simulated and experimental selectivities could be due to several reasons, most notably the flexibility of the MOF structures. Although a detailed demonstration of this effect will be forthcoming in a later work, we suggest here that structural flexibility can cause large differences in selectivities especially near saturation loading conditions.

Table 3.2 *p*-xylene adsorption selectivities and total C_8 capacities for selected MOFs and zeolite BaX. The data values are shown in the format A/B (C), where A = value obtained from raw experimental breakthrough data, B = value obtained from model-fitted breakthrough curves, and C = value obtained from GCMC simulations. No simulation data is available for zeolite BaX.

Adsorbent	T (°C)	$S_{pX/EB}$	$S_{pX/mX}$	$S_{pX/oX}$	q_{max} (mmol/cm^3)
MIL-47	50	1.7/2.3 (17.2)	1.1/1.0 (2.3)	0.6/0.7 (0.5)	5.7/10.0 (4.3)
MIL-125-NH_2	50	1.3/1 (1.3)	1.5/1.2 (3.2)	1.6/1.2 (3.5)	1.9/3.1 (4.2)
MIL-140B	50	2.1/1.7 (0.8)	1.6/1.2 (5.0)	1.8/1.4 (175)	1.7/2.0 (1.6)
MOF-48	50	1.5/1.3 (0.7)	1.7/1.6 (9.8)	1.7/1.4 (6.9)	2.6/2.9 (2.2)
BaX	180	1.9/1.8	1.6/1.6	1.4/1.4	3.0/3.4

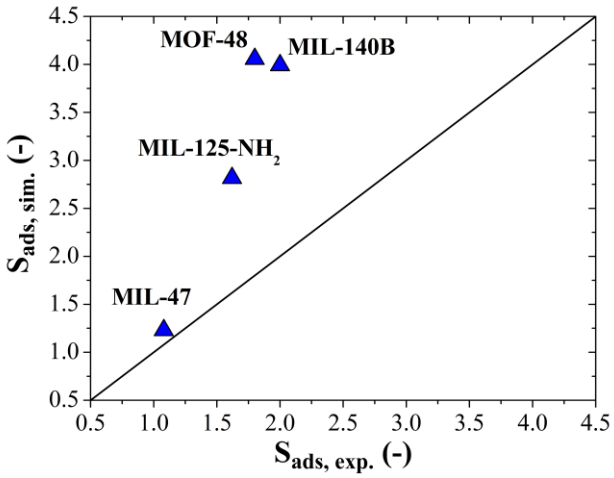

Figure 3.4 Comparison of simulated and experimental selectivities in selected MOFs for a bulk liquid composition of 0.33:1:2:1 ethylbenzene/*o*-xylene/*m*-xylene/*p*-xylene at 50°C and 9 bar in simulations and 35 bar in experiments.

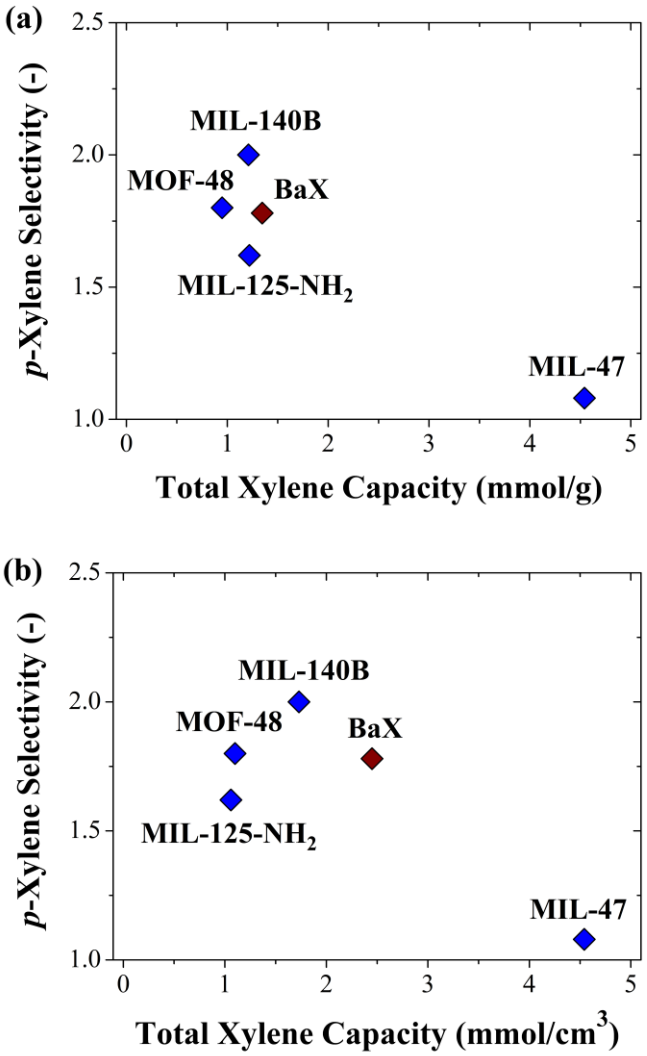

Figure 3.5 Graphical comparison of experimental selectivities versus (a) gravimetric or (b) volumetric capacities in selected MOFs and laboratory-exchanged zeolite BaX for a bulk liquid feed composition of 0.33:1:2:1 F. The pressure is 35 bar in experiments and 9 bar in simulations and the temperature is 50°C for the MOFs and 180°C for BaX. Experimental results from both the raw breakthrough data as well as the model-fitted breakthrough curves are shown.

Figure 3.5 shows the experimental results for overall *p*X selectivity (Equation 3.1) and total C_8 gravimetric and volumetric capacity for the selected MOFs compared to the laboratory-exchanged zeolite BaX. We observe that the top-performing *p*X-selective MOFs exhibit moderately higher selectivities and similar gravimetric capacities in comparison to the zeolite. However, the performance of these MOFs is somewhat

reduced in terms of volumetric capacity due to their lower densities (0.9-1.4 g/cm^3) than that of the zeolite (~1.8 g/cm^3). Although MIL-47 does not possess *p*X selectivity, it is clear that this material has an enormous capacity for adsorption of xylenes. This led us to synthesize a functionalized version of this material seeking improvements in the *p*X-selectivity, as in the case of MOF-48. Both the GCMC simulations (Figure 3.4) and experimental results (Figure 3.5) show the dramatic increase in *p*X selectivity in MOF-48 over that of MIL-47. Although simulations predict that the xylene capacity of MOF-48 should be only slightly reduced from that of MIL-47, the experiments show a drastically reduced capacity in MOF-48. As mentioned earlier, this is most likely related to the low surface area of the present (and previously reported) MOF-48 materials, and indicates the desirability of optimizing its synthesis and activation conditions.

To better understand the mechanism of the *p*X-selectivity, we calculated adsorbate free energy profiles in the MOFs using a liquid feed of 0.33:1:2:1 eb/*o*-xylene/*m*-xylene/*p*-xylene at 9 bar and 50°C. Figure 3.6 shows the free energy profiles of the xylene isomers and ethylbenzene along the 1-D channels of MIL-47 and MOF-48. These profiles were determined by collecting histograms of the center of mass of each molecule at each point along the channel axis during the simulation.[111] The molecule with the lowest free energy along the entire channel length is preferentially adsorbed in the MOF. From the figure, it is clear that *o*-xylene is more strongly adsorbed along the channel in MIL-47 whereas *p*-xylene is favored in MOF-48. We find that the addition of methyl functional groups to the BDC linkers of MIL-47 causes a change from *o*X- to *p*X-selectivity in this material. This effect is due to corrugation in the channel topology of MOF-48 compared to MIL-47 as shown in Figure 3.6. This effect leads to enhanced *p*-

xylene selectivity in MOF-48 and separation properties that are comparable to the zeolite adsorbent.

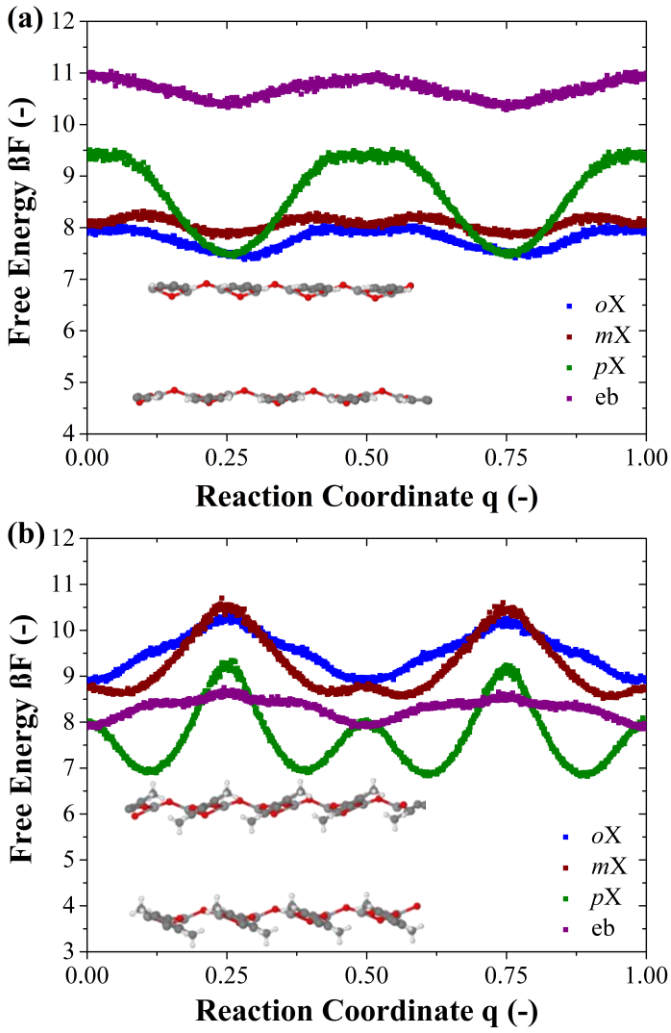

Figure 3.6 Free energy profiles of the xylene isomers and ethylbenzene in the 1-D channels of (a) MIL-47 and (b) MOF-48 constructed using histograms from simulations under feed conditions of 0.33:1:2:1 ethylbenzene/o-xylene/m-xylene/p-xylene at P = 9 bar and T = 50°C. The inset figure shows the channel topology of each of the MOFs.

3.4 Conclusion

We have demonstrated a computational method that can identify *p*-xylene-selective materials from a large database of MOF materials. We have then synthesized several of the predicted best-performing materials and evaluated their xylene separation properties using breakthrough adsorption measurements and model-based fitting of the breakthrough data. The experiments confirm the *p*-xylene selectivities of the selected MOF materials. The top-performing materials, MIL-140B and MOF-48, are found to have *p*-xylene selectivities that exceeded that of the laboratory-exchanged zeolite BaX. Our simulations demonstrate that functionalization of the BDC linkers in MIL-47 with dimethyl groups causes corrugation in the channel topology that favors the adsorption of *p*-xylene in MOF-48 compared to *o*-xylene MIL-47. Further optimization of the MOF-48 synthesis and activation processes can allow access to a much larger fraction of its pore volume, and has the potential to yield a *p*X-selective as well as high-capacity material. The present work is an example of the utility of our methodology combining molecular simulation and targeted experiments to enable accelerated discovery and development of promising materials for a given separation.

CHAPTER 4

ADSORPTION AND DIFFUSION OF SMALL ALCOHOLS IN ZEOLITIC IMIDAZOLATE FRAMEWORKS ZIF-8 AND ZIF-90[3]

4.1 Introduction

Metal-organic frameworks (MOFs) are crystalline nanoporous materials composed of metal centers and organic linkers.[7,112-114] They have a number of potential applications in gas storage,[1,2] chemical separations,[3,4,115] catalysis,[6,116-118] drug delivery,[5] and molecular sensing.[8] Zeolitic imidazolate frameworks (ZIFs) are a class of MOFs that share similar pore topologies with zeolites and have been shown to exhibit good chemical and thermal stability.[119] ZIF-8 and ZIF-90 possess large cavities and small windows that enable the separation of small molecules by molecular sieving.[120-124] ZIF-8 (ZIF-90) consists of Zn^{2+} tetrahedrally coordinated to 2-methylimidazolate (imidazole-2-carboxaldehyde) linkers that crystallize into the sodalite zeolite topology after hydro- or solvo-thermal synthesis.[119,125,126] The pores of ZIF-8 have been determined to be hydrophobic in computational[127] and experimental[128] studies based on the heat of adsorption of water.

An emerging area of interest is the consideration of ZIF materials in liquid-phase separations[129,130] and catalysis involving organic molecules.[131,132] Recent experimental studies have found that hydrophobic MOFs, including ZIF-8,[130] exhibit substantial

[3] Material in this chapter has been previously published as Gee, J. A.; Chung, J.; Nair, S.; Sholl, D. S. Adsorption and Diffusion of Small Alcohols in Zeolitic Imidazolate Frameworks ZIF-8 and ZIF-90. *The Journal of Physical Chemistry C* **2013**, *117*, 3169-3176.

adsorption selectivity for small alcohols over water.[133,134] While Grand Canonical Monte Carlo (GCMC) simulations have been used extensively to study the adsorption of small nonpolar molecules in MOFs,[19,135] less has been done to characterize the adsorption of alcohols, which are both good models for polar molecules in MOFs as well as technologically interesting in their own right. Nalaparaju et al. studied the adsorption of water and small alcohols in hydrophobic and hydrophilic ZIFs using GCMC simulations.[136] They used their simulations to identify useful materials and operating conditions for the separation of alcohols and water. To date, however, there has not been an assessment of the reliability of molecular simulations in predicting adsorption isotherms for alcohols in MOFs. A detailed understanding of the equilibrium and transport properties of alcohols in these materials would aid in their consideration for applications such as biofuel purification processes.

For separations in nanoporous materials involving molecules of dissimilar sizes, it is often necessary to characterize the effect of mass transport limitations in the material. A useful metric for characterizing this effect is the minimum pore dimension along a path passing through the entire material, or pore limiting diameter (PLD). The PLD characterizes the pore size relevant to diffusion for molecules whose motion is sterically limited.[9] The pore limiting diameter (PLD) of the rigid ZIF-8 and ZIF-90 structures used in this chapter are approximately 3.4 Å,[137] while the kinetic diameters of methanol and ethanol are 3.6 Å and 4.5 Å,[138] indicating that transport limitations may be significant for these adsorbates. Computational studies of diffusion in MOFs often use molecular dynamics (MD) simulations with generic force fields to simulate the motion of the adsorbate through the pores of the MOF.[28-30] Self-diffusion coefficients obtained from

MD simulations can be compared to corresponding experimental measurements using pulsed field gradient NMR (PFG-NMR).[139,140] Recent studies have found good agreement between simulated and experimental diffusivities for small hydrocarbons in MOF-5[31] and CuBTC,[32] two MOFs in which the pore sizes that control diffusion are large relative to the kinetic diameter of the diffusing species. We are not aware, however, of direct comparisons of this type in examples where the MOF pore size is similar to the size of the diffusing molecules.

Framework flexibility is a notable feature of MOFs and zeolites that can allow observable diffusivities for molecules with kinetic diameters greater than the pore size of the rigid framework.[9,141-147] Bux et al. observed considerable permeability of methane in ZIF-8 using IR microscopy despite methane possessing a larger kinetic diameter (3.8 Å) than the PLD of the rigid framework.[120] Zhang et al. recently estimated an effective aperture size for ZIF-8 between 4.0-4.2 Å based on kinetic uptake measurements of short alkanes.[148] Several studies have computed the diffusivity of methane in ZIF-8 using MD simulations with both rigid and flexible MOF frameworks.[33-35] These studies predicted methane diffusivities $< 10^{-13}$ m^2/s in rigid frameworks, but found diffusivities nearly two orders of magnitude higher when allowing for framework flexibility. An exception to this trend was observed in the study of Hertäg et al.,[34] where they used their MD simulations with the DREIDING force field to predict the effect of framework flexibility in ZIF-8 and found the diffusivity of CH_4 was a factor of ~4 slower than in the rigid case. For smaller molecules such as CO_2, modeling studies comparing the effect of framework flexibility in ZIF-8 have also shown conflicting trends. Haldoupis et al. observed a factor of ~9 increase in CO_2 diffusivity when allowing for framework flexibility in ZIF-8 using

structural information from *ab initio* molecular dynamics (AIMD) simulations,[149] while classical MD simulations[36] predicted a decrease by a factor of ~2. Based on these results, it is unclear what role framework flexibility plays in the diffusion of small alcohols in ZIFs.

The choice of force field used in MD simulations can also have a significant effect on the accuracy of the predicted diffusivities. Discrepancies as large as two orders of magnitude have been observed for the diffusivities of methane in ZIF-8 computed using different generic force fields.[34] Recent studies have developed fully flexible force fields to accurately reproduce the experimental lattice constants in ZIF-8. The use of these force fields in MD simulations has resulted in predicted diffusivities for methane and CO_2 that are in better agreement with experiment data.[35-37] Although their application has been successful in studies of the diffusion of simple adsorbates, the extension of these force fields to more complex species has not been investigated.

In this chapter, we report adsorption isotherms, self-diffusion coefficients, and Arrhenius parameters for methanol and ethanol in ZIF-8 and ZIF-90 using molecular simulations and experiments. We also investigate the accuracy and transferability of generic and experimentally fitted force fields in describing adsorption and diffusion in these materials.

4.2 Simulation Details

The experimentally determined crystal structures for ZIF-8 and ZIF-90 were taken from the Cambridge Structural Database (CSD).[150] Each structure was then optimized using plane wave density functional theory (DFT) calculations as implemented in the Vienna *ab initio* simulation package (VASP).[151] The Perdew-Burke-Ernzerhof (PBE) functional was used for electron exchange and correlation.[152] Unit cell optimizations were performed at the Γ-point and used the conjugate gradient algorithm until the forces on each atom were < 0.02 eV/Å. The optimization method for each structure followed a similar procedure. Atomic positions were first optimized using an energy cutoff of 400 eV, followed by a relaxation of both atomic positions and unit cell parameters at a cutoff of 700 eV. A final optimization of atomic positions was performed at a cutoff of 400 eV to ensure the atoms were at their true energetic minima. Point charges were assigned to the framework atoms using these optimized structures with the DDEC method of Manz et al.[65,67]

Two separate force fields were used for each of the ZIFs in GCMC and MD simulations: a modified GAFF force field[27,153] and the generic DREIDING force field of Mayo et al.[52] The equilibrium distances used in the GAFF force field were based on experimental bond lengths and angles of the ZIF-8 structure. The lattice constants of the ZIF-8 and ZIF-90 framework were found to be in better agreement with experiments using GAFF compared to DREIDING (see Table C.1). The TraPPE united atom force field was used to model the alcohols.[154] This force field accurately represents the bulk phase behavior of these molecules. Adsorbate-adsorbent interaction terms were defined

using a Lennard-Jones potential with a cutoff of 13 Å and parameters given by the Lorenz-Berthelot combining rules.

GCMC and hybrid GCMC (HGCMC) simulations were performed using the Multipurpose Simulation Code (MUSIC).[155] DFT-optimized ZIF geometries were used in all of the GCMC simulations with the framework and adsorbate molecules kept rigid throughout the simulations. The bulk fluid phase fugacity was assumed to be equal to the pressure due to the low pressure ranges used in our simulations. The Wolf method was used to compute electrostatic interactions using a damping parameter, α, equal to 0.1 and a spherical cutoff distance of 13 Å.[156] Preliminary adsorption simulations for methanol in ZIF-90 using a rigid framework were used to verify that the Wolf method provided approximately equivalent results compared to the more computationally intensive Ewald summation technique. GCMC simulations consisted of an equilibration and production period of 2×10^7 moves using energy-biased adsorbate insertions/deletions, translations, and rotations with fractional weights of 0.75, 0.2, and 0.05 respectively. To simulate adsorption in ZIF-90, HGCMC simulations were used to account for flexibility of the aldehyde group in each linker. The HGCMC simulations allowed insertion and deletion moves for adsorbates as in standard GCMC and also a global update of the position of the atoms of the aldehyde group in ZIF-90 using a short MD step. Bonded potentials for the aldehyde group were taken from the GAFF force field and consisted of stretching, bending, and improper torsion terms. The aldehyde group was tethered to the remaining atoms in the rigid framework using a flexible C-C bond. The remaining atoms in the ZIF-90 framework were fixed at their DFT-optimized geometries throughout the HGCMC simulations. The length and number of MD steps was selected to ensure a 50%

acceptance ratio of displacements in the atomic positions of the aldehyde group.[157] On average, the number of successful MD steps (timestep) in the HGCMC simulations was ~4×10^4 (~1 fs).

All NVT MD simulations were performed using the LAMMPS simulation code.[158] Lattice constants and atomic positions were optimized prior to each simulation using the appropriate force field and a conjugate gradient algorithm until the forces on each atom were < 0.01 eV/Å. Temperature control was achieved using a Nosé-Hoover thermostat with a decay period of 0.1 ps. Electrostatic interactions were computed using the conventional Ewald summation technique with a relative accuracy of 10^{-6}. Before each MD run, adsorbate molecules were randomly inserted into each ZIF structure with the restriction that insertion moves were only accepted if they lowered the total energy of the adsorbate-adsorbent system. The loadings used in the diffusivity calculations were the same as those used in the PFG-NMR diffusivity measurements. All MD simulations used a time step equal to 1 fs. Before each production run, the system was equilibrated with a 1 ns NVT MD simulation. The average mean squared displacement was computed for many adsorbate molecules over a 10 ns NVT MD production period and used to compute the self-diffusivity using the Einstein relation.[159] An example of a plot of the MSD versus time used to compute the diffusivity is shown in Figure C.1.

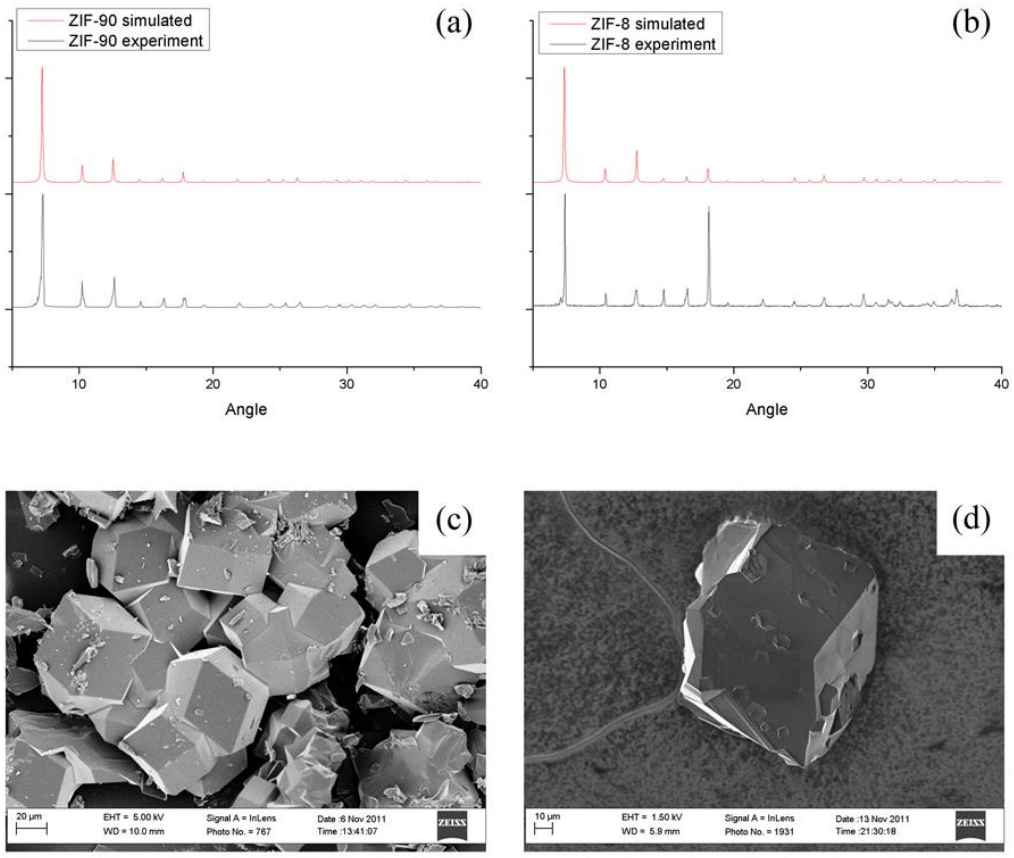

Figure 4.1 Measured and simulated X-ray diffraction (XRD) patterns, and SEM images, of ZIF-90 (a,c) and ZIF-8 (b,d) crystals.

4.3 Experimental Methods[4]

Zinc(ll) nitrate hexahydrate (Sigma-Aldrich), imidazole-2-carboxaldehyde (Alfa Aesar), 2-methyl-imidazole (99%, Sigma-Aldrich), and sodium formate (Sigma-Aldrich) were used as received without further purification. To synthesize ZIF-90, 1.488 g of zinc(ll) nitrate hexahydrate and 1.921 g of imidazole-2-carboxaldehyde were dissolved in 100 ml of dimethylformamide (DMF). The solution was heated to 393 K for 10 min and then cooled to ambient temperature at a rate of 5 K/min. A light-orange crystalline

[4] All experimental work reported in this chapter was performed by Jaeyub Chung in Dr. Sankar Nair's laboratory at Georgia Tech.

material was separated from the solution by decantation. The crystals were washed with methanol and then dried at 333 K for 12 h. To synthesize ZIF-8, 3.528 g of zinc(ll) nitrate hexahydrate, 1.944 g of 2-methyl-imidazole, and 0.807 g of sodium formate were mixed in 80 ml of methanol and ultrasonicated in a bath for 1 min. The solution was then heated at 363 K in a Teflon-lined stainless steel autoclave for 24 h. After cooling, a crystalline material was collected from the bottom and sides of the Teflon liner. The crystals were washed with methanol and dried at 333 K for 12 h. X-ray diffraction (XRD) patterns and SEM images of the two materials are shown in Figure 4.1, verifying the ZIF-8 and ZIF-90 structures and the large crystal sizes (about 50 μm for ZIF-90 and 100 μm for ZIF-8).

Approximately 200 mg of sample was introduced into a 10 mm OD glass nuclear magnetic resonance (NMR) sample tube and degassed under vacuum at 393 K (ZIF-90) or 453 K (ZIF-8) for 24 h. The samples were cooled to ambient temperature in an ultra-high purity nitrogen purge stream. Calculated amounts of alcohol adsorbates (4.5 mmol methanol/g-ZIF, 2.25 mmol ethanol/g-ZIF) were introduced into the sample tube, which was then sealed and allowed to equilibrate for 48 h before conducting the NMR measurements. The experimental diffusion measurements were performed by the PFG NMR technique at 400 MHz ^{1}H resonance frequency using stimulated spin-echo[160] sequences. The NMR spin-echo intensity is sensitive to the mean-square displacement during the diffusion time interval (Δ) between a pair of pulsed field gradients. The spin echo intensity $M(b)$ is measured as a function of the variable b, which depends on the PFG-NMR parameters of the selected pulse sequence. Since the intercrystalline concentration of the alcohols was expected to be very low, a single-exponential model[161]

was able to fit the spin-echo attenuation and determine the self-diffusivity of alcohol molecules in the ZIF:

$$\frac{M(b)}{M_0} = \exp\left(-bD_{self}\right) \quad \text{with} \quad b = (\gamma G\delta)^2(\Delta - \frac{1}{3}\delta) \qquad (4.1)$$

where D_{self}, G, δ, and Δ represent the self-diffusivity, intensity of the gradient pulse, duration of the gradient pulse, and the time interval between the pair of gradient pulses, respectively. Our technique used a diffusion time Δ = 500 ms, gradient pulse length δ = 1.01 ms and maximum gradient G = 5.01×10^{-2} T/m. The bulk self-diffusion coefficient of anhydrous methanol measured using our PFG-NMR method was 2.47×10^{-9} m^2/s at T = 30°C, in good agreement with the value of 2.41×10^{-9} m^2/s at T = 25°C reported by Hurle et al.[162] using a similar technique.

4.4 Adsorption Results and Discussion

Adsorption isotherms for methanol and ethanol on ZIF-8 from GCMC simulations are presented in Figure 4.2. To facilitate comparison with adsorption measurements reported by Chmelik et al.[163] using infrared microscopy (IRM) in terms of fractional loading, we converted their data to absolute loadings using the saturation loadings measured by Cousin Saint Remi et al.[130] The GCMC simulated isotherms using both the GAFF and DREIDING force fields are in good agreement with the IRM measurements. Slight adsorption selectivity for ethanol over methanol is observed for ZIF-8 in both experiments and simulations. These results agree qualitatively with measurements[130] at T = 50°C using a gravimetric adsorption apparatus.

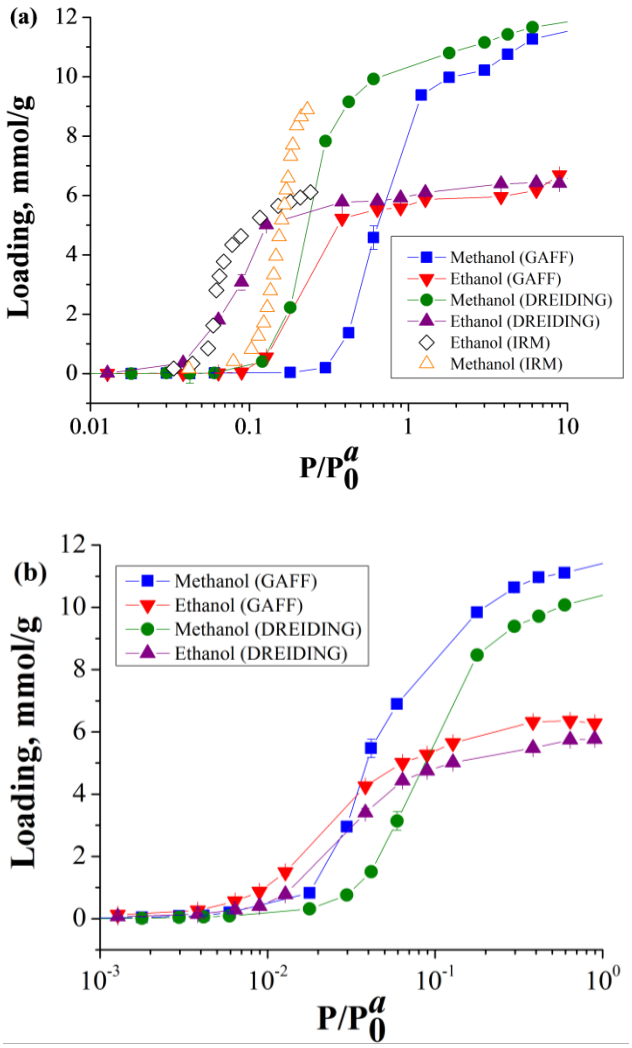

Figure 4.2 GCMC-simulated adsorption isotherms for methanol and ethanol in (a) ZIF-8 and (b) ZIF-90 using the GAFF and DREIDING force fields. The simulation results for ZIF-8 are compared to the experimental adsorption measurements made by Chmelik et al.[163] using infrared microscopy (IRM).

[a]Pressures were normalized by the saturated vapor pressure of each alcohol ($P_{0,CH3OH}$ (25°C) = 16.9 kPa, $P_{0,CH3CH2OH}$ (25°C) = 7.8 kPa).[164]

The simulated adsorption isotherms shown in Figure 2 indicate that the adsorption of alcohols at low pressures is significantly higher in ZIF-90 compared to ZIF-8. To understand this effect in greater detail, we studied the hydrogen bonding between the hydroxyl group of the methanol molecules and the carbonyl oxygen of ZIF-90 during the

GCMC production period. Methanol was selected as a model adsorbate for larger polar organic molecules in these simulations due to its large dipole moment. Hydrogen bonding was considered if the O···O distance was less than 3.5 Å and the O-H···O angle was less than 30°.[165] A similar procedure was used by Zang et al. to study hydrogen bonding between physisorbed water molecules and the surface hydroxyl groups of aluminosilicate nanotubes.[166]

Using the criteria defined above, we calculated the number of hydrogen bonds formed between methanol and the MOF framework as a function of pressure. The results, shown in Figure 4.3, show that interactions between methanol and the framework are dominated by hydrogen bonding between methanol and the carbonyl oxygen of ZIF-90 at low loadings. This interaction is responsible for the enhanced uptake of alcohols on ZIF-90 compared to ZIF-8, which is not capable of hydrogen bonding. Methanol-methanol hydrogen bonding reaches a maximum at high pressures where the methanol molecules form a dense phase within the pores.

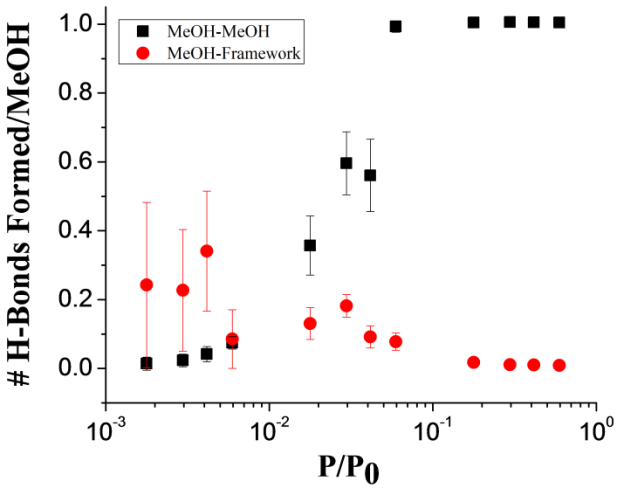

Figure 4.3 Number of hydrogen bonds formed between methanol molecules and the carbonyl group of ZIF-90 calculated using the criterion defined in the text.

We also performed simulations to examine whether framework flexibility is crucial to correctly describing adsorption of hydrogen bonding species in ZIF-90. The calculations shown above used HGCMC to allow the aldehyde groups in ZIF-90 to be flexible during adsorption simulations. Figure 4.4 compares the adsorption isotherm obtained with this approach with the isotherm computed holding the entire ZIF-90 framework rigid. The results indicate that including framework flexibility only increases the adsorbed amounts slightly at low and moderate pressures. This is quite different from the situation in aluminosilicate nanotubes, where reorientation of hydrogen bonding groups during adsorption can have a large impact on the overall adsorption isotherm.[166] The relatively weak impact of aldehyde flexibility can be understood in terms of Figure 4.3, which shows there are a relatively low number of hydrogen bonds formed between methanol and the framework over the entire range of pressures. This result is in qualitative agreement with the results of Amrouche et al., who determined that the pores of ZIF-90 are hydrophobic based on the isosteric heat of adsorption of water at infinite dilution.[127] It is reasonable to expect, however, that the effect of framework flexibility may be significant for ZIFs with more strongly hydrophilic functional groups.

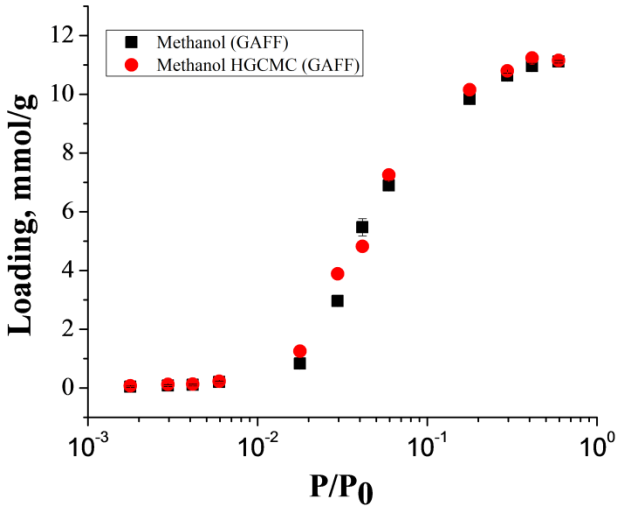

Figure 4.4 Adsorption isotherms for methanol in ZIF-90 computed using GCMC with a rigid framework (black symbols) and using HGCMC including aldehyde flexibility (red symbols).

4.5 Diffusion Results and Discussion

The self-diffusion coefficients of methanol and ethanol in ZIF-8 and ZIF-90 were predicted using NVT MD simulations and compared with PFG-NMR measurements using the methods described earlier. The alcohol loadings used in the simulations were the same as those used in the PFG-NMR measurements. Preliminary calculations indicated that the self-diffusion coefficient of methanol was insensitive to variations in loading of up to 10% around the loading used in our experiments in ZIF-8. Due to the slow diffusion predicted by our MD simulations, additional runs were performed to ensure that a substantial number of adsorbate molecules passed through multiple unit cells during the simulations (see Table C.2). Time scale limitations dictated that our MD method was not able to give reliable results for diffusivities $< 10^{-12}$ m^2/s, as the calculations would be prohibitively time consuming.

Table 4.1 gives the self-diffusion coefficients for methanol and ethanol in ZIF-8 and ZIF-90 using two different force fields, GAFF and DREIDING. For each case, separate calculations were performed with a rigid ZIF structure and allowing all degrees of freedom in the structure to be flexible. One interesting outcome is that the inclusion of framework flexibility makes only a small difference in the computed self-diffusivities of the alcohols. This can most clearly be seen in the case of ZIF-90, where the methanol diffusivity is fast enough to be reliably computed using MD for all four calculations. The GAFF force field predicts that including framework flexibility increases the diffusivity of methanol by a factor of ~2, while DREIDING predicts a decrease in diffusivity by a factor of ~3. A qualitatively similar effect for these two force fields was seen in the study of Hertäg et al.,[34] where their MD simulations predicted that the self-diffusion coefficient of CH_4 increased by greater than two orders of magnitude when modeling framework flexibility in ZIF-8 using GAFF, but decreased by a factor of ~4 using DREIDING. Haldoupis et al.[149] also determined that the diffusivity of CH_4 could vary by a factor of ~50 using different rigid approximations to the ZIF-8 structure with nearly identical pore sizes using AIMD. Overall, these results show that the effect of framework flexibility is a complicated function of the adsorbate potential energy surface and cannot be simply described as always increasing or always decreasing diffusivity relative to the rigid pore structure.

Table 4.1 Computed self-diffusion coefficients of methanol in ZIF-8 and ZIF-90 at 25°C using the GAFF and DREIDING force fields with flexible and rigid frameworks compared with PFG-NMR and IRM measurements.

ZIF	Force Field	$D_{s,MeOH}$ (× 10^{-12} m^2/s)		
		Rigid	Flexible	PFG-NMR
ZIF-8	GAFF	< 1	~1	38.94
	DREIDING	< 0.1	< 0.1	
ZIF-90	GAFF	~2	6.3 ± 2.4	109.5
	DREIDING	7.2 ± 0.7	~3	

[b]The experimental and simulated alcohol loadings were 4.5 mmol methanol/g-ZIF ($\theta \approx 0.5$) and 2.25 mmol ethanol/g-ZIF ($\theta \approx 0.35$). Note: $\theta = n_{ads}/n_{sat}$.

Table 4.1 also compares our MD results for the self-diffusion coefficients of methanol measured using our PFG-NMR method and the measurements of Chmelik et al.[163] using infrared microscopy (IRM). The IRM technique uses transient intracrystalline concentration profiles to measure transport diffusivities, which are converted to self-diffusivities using a thermodynamic correction factor determined from experimental adsorption isotherms. PFG-NMR and IRM techniques both probe diffusion on length scales much shorter than a typical separation distance between intracrystalline defects in MOFs[167,168] and therefore their measurements can be compared directly. The self-diffusion coefficients reported using IRM were measured at similar alcohol loadings as those used in this chapter. As shown in Table 4.1, the self-diffusion coefficients for methanol in ZIF-8 measured using PFG-NMR and IRM are in reasonable agreement. In all cases, the observed self-diffusion coefficients are considerably lower than the diffusivities of the alcohols in their bulk liquid phase, measured, as described above to be 2.5×10^{-9} m^2/s for methanol at 25°C.

The self-diffusivities measured by PFG-NMR and IRM are substantially larger than our MD results. The most meaningful comparison can be made with the MD results using the GAFF force field including the effect of framework flexibility. In this case, the PFG-NMR results for ZIF-8 (ZIF-90) are 37 (17) times larger than the MD result. The accuracy of these results can be compared to the MD diffusion study of Zheng et al.,[36] where the self-diffusion coefficient of CO_2 was found to be within 20% of the experimental value when including the effect of framework flexibility in ZIF-8 using the GAFF force field. Our MD results are in better agreement with the IRM measurements, underpredicting the experimentally observed diffusivity by a factor of 6. Qualitatively, however, the PFG-NMR and MD results agree that diffusion of both alcohols is more rapid in ZIF-90 than in ZIF-8.

The self-diffusion coefficients for methanol and ethanol in each MOF computed using MD simulations with the GAFF force field are compared with experiments in Table 4.2. While our MD simulations are unable to provide exact estimates of the diffusivities of ethanol, they are able to qualitatively capture the high diffusion selectivity for methanol over ethanol observed in ZIF-8 and ZIF-90. Our PFG-NMR measurements show that ZIF-8 (ZIF-90) exhibits a diffusion selectivity, $S = D_{methanol}/D_{ethanol}$, of $S = 229$ ($S = 6$) for methanol over ethanol at T = 25°C. The IRM value of S ~ 30 for ZIF-8 at T = 25°C was lower than our PFG-NMR measurements but still showed significant diffusion selectivity for methanol. Overall, our results show that both ZIFs exhibit high diffusion selectivity for methanol over ethanol.

Table 4.2 Computed self-diffusion coefficients of methanol and ethanol in ZIF-8 and ZIF-90 at 25°C using the GAFF force field including framework flexibility compared with corresponding PFG-NMR and IRM measurements.

		D_s ($\times 10^{-12}$ m^2/s)		
ZIF	**Adsorbate**	GAFF (Flexible)	PFG-NMR (this work)	IRM (Chmelik et al.)
ZIF-8	CH_3OH	~1	38.94	~6.3
	CH_3CH_2OH	< 0.1	0.17	~0.14
ZIF-90	CH_3OH	6.3 ± 2.4	109.50	-
	CH_3CH_2OH	< 1	19.03	

The Arrhenius parameters for the diffusion of the alcohols in both ZIFs measured using PFG-NMR and MD are shown in Table 4.3. The self-diffusion coefficients were measured over the temperature range 30-100°C using the same alcohol loadings as before. The experimental measurements were compared to MD-simulated diffusivities calculated using the GAFF force field including framework flexibility. The MD-simulated values could only be determined for the diffusion of methanol in ZIF-90 due to time scale limitations. As shown in Table 4.3, the simulated activation energy for the diffusion of methanol in ZIF-90 using MD is in good agreement with the experimental value measured using PFG-NMR. The simulated and experimental activation energies for the alcohols are slightly higher in ZIF-90 compared to ZIF-8 and much greater than kT at 25°C (~2.5 kJ/mol). All of our results are of the same order of magnitude as the activation energies previously reported for the diffusion of small alkanes in ZIF-8.[169,170]

Table 4.3 also shows that the activation energies for the diffusion of methanol and ethanol are approximately the same, despite methanol diffusing more rapidly than ethanol in both ZIFs. As a result, the pre-exponential factors are significantly larger for methanol compared to ethanol in each material. A similar trend was observed in the study of Wehring et al.,[32] where their MD simulations of the diffusion of short chain alkanes in the large-pore MOF CuBTC predicted that the pre-exponential factor decreased by a factor of ~2 with increasing chain length while the activation energies were approximately independent of chain length. This effect is more dramatic in this chapter, where we observe a three-orders-of-magnitude difference in the pre-exponential factors between the diffusion of methanol and ethanol in ZIF-8. This observation points to the importance of entropic factors in determining the overall hopping rate of alcohols among cages in these materials. Our results also highlight the challenge in using simple applications of transition state theory (TST) to calculate the diffusivities in these systems. Many applications of TST in MOFs and zeolites assume that the pre-exponential factor is a constant for different diffusing species.[171] This approach would not capture the significant diffusion selectivity that is observed experimentally for both ZIFs.

Table 4.3 Arrhenius parameters for diffusion of methanol and ethanol in ZIF-8 and ZIF-90 measured over the temperature range 30-100°C using PFG-NMR and MD.

ZIF	Adsorbate	PFG-NMR		GAFF (Flexible)	
		D_0 (m^2/s)	E_A (kJ/mol)	D_0 (m^2/s)	E_A (kJ/mol)
ZIF-8	CH_3OH	1.10×10^{-8}	14.2	-	
	CH_3CH_2OH	4.57×10^{-11}	14.0		
ZIF-90	CH_3OH	1.01×10^{-7}	17.2	9.73×10^{-9}	19.4
	CH_3CH_2OH	1.63×10^{-8}	17.5	-	

4.6 Conclusion

In this chapter, the adsorption and diffusion of small alcohols in ZIF-8 and ZIF-90 were studied using molecular simulations and experiments. Our GCMC simulated adsorption isotherms for the adsorption of small alcohols in ZIF-8 were in good agreement with previous experimental data and indicated a slight adsorption selectivity for ethanol over methanol. A similar trend was observed in the simulation results for adsorption of the alcohols in ZIF-90. Hydrogen bonding was found to increase the adsorption uptake of alcohols at low pressures in ZIF-90 compared to ZIF-8 due hydrogen bonding with the carbonyl group of ZIF-90. We found that hydrogen bonding in the case of ZIF-90 was not strong enough to cause significant distortion of the framework during adsorption using HGCMC simulations. Although this effect was small for the hydrophobic ZIF-90 framework, it may be significant in the case of hydrophilic ZIFs.

We also measured self-diffusivities and Arrhenius parameters for the alcohols in both ZIFs using PFG-NMR and MD. It was found that ZIF-8 exhibits significant

diffusion selectivity for methanol over ethanol. This result underscores the potential for using this material for the kinetic separation of the alcohols in biofuel purification processes. Overall, reasonable agreement was obtained between PFG-NMR measurements and MD simulations using the GAFF force field including framework flexibility. Our findings support the idea that simulations using readily available force fields can be used to reliably predict adsorption and diffusion of small alcohols in these materials.

CHAPTER 5

CHARACTERIZATION OF THE THERMODYNAMIC STABILITY OF SOLVATED METAL-ORGANIC FRAMEWORK POLYMORPHS USING MOLECULAR SIMULATIONS[5]

5.1 Introduction

Zeolitic imidazolate frameworks (ZIFs) are a class of metal-organic frameworks (MOFs) composed of inorganic metal centers and imidazole-type organic linkers.[119] ZIFs are known to exhibit polymorphism and have been experimentally synthesized in a variety of zeolite-like topologies by varying the metal center, organic linker, and solvothermal conditions used during synthesis.[119,137,172-174] The ability to experimentally target a particular topology could give rise to materials with enhanced properties for a number of applications in gas storage[175-177] and chemical separations[4,49,178]. Although the ZIF synthesis process may be under kinetic control, thermodynamic control, or a combination of both, it is expected that the solvent can play a role in accessing synthetic pathways to different polymorphs by stabilizing intermediate framework structures[179,180] as in the case of zeolites[181,182]. An understanding of the relative thermodynamic stabilities of polymorphs under different solvothermal conditions could be used to aid in experimental design for synthesis of these materials.

[5] Material in this chapter has been previously published as Gee, J. A.; Sholl, D. S. Characterization of the Thermodynamic Stability of Solvated Metal–Organic Framework Polymorphs Using Molecular Simulations. *The Journal of Physical Chemistry C* **2013**, *117*, 20636-20642.

The stability of zeolite polymorphs has primarily been examined theoretically using *ab initio* single point energy calculations based on the empty frameworks.[179,183-188] While these methods are able to accurately quantify the total energy of each structure, they are unable to account for the effect of guest molecules and temperature on the stability of the framework. The entropic component of the stability of several SiO_2 polymorphs has been investigated analytically using free energy minimization[189] and numerically using a coarse-grained representation of the zeolite framework and the method of Frenkel and Ladd.[190,191] Although this contribution may have an effect on the framework stability at high temperatures, calorimetric measurements have shown the difference in entropy between SiO_2 polymorphs to be negligible under most conditions[182].

The stability of multiple MOF and covalent organic framework (COF) polymorphs have been investigated using density functional theory (DFT) calculations[179,183,187,192] and calorimetric experiments[180,193]. Many theoretical studies on this subject[179,183,187] have focused on the prediction of polymorph structures and accurate quantification of framework energetics. The work of Amirjalayer et al.[194] extended this methodology to parameterize a DFT-based force field that was then used to accurately predict the structural and energetic properties of the framework for a set of copper paddle wheel MOFs. The same authors applied a similar methodology to covalent organic frameworks (COFs)[192] and demonstrated that their DFT-derived force field could be used to search for structure-property relationships among a series of real and hypothetical COF structures. The energetics of multiple ZIF polymorphs have recently been investigated using experimental[180] and theoretical[179,183,187] measurements of the energies of the empty frameworks. Both DFT simulations and experiments are in agreement that the stability of

the ZIF polymorphs increases with increasing framework density. Similar to observations in zeolites,[181] these studies predicted that small energetic differences separate different metastable polymorph structures.

Compared to the structural energetics of MOF and zeolite polymorphs, the effect of solvent on the stability of the framework has garnered less attention. In zeolites, the effect of structure-directing agents (SDAs) has been shown to have a small influence on the stability of SiO_2 polymorphs.[182] In the case of MOFs, Hughes et al.[180] measured an enthalpy of solvation of only -3 kJ per mole of Zn in ZIF-4 using dimethylformamide (DMF) as solvent. In a similar study, a solvation enthalpy of N,N-diethylformamide (DEF) of -4.8 kJ per mole of Zn was measured in the large-pore MOF-5.[193] These measurements suggest that, as in the case of SDAs in zeolites, the solvent has a minor effect on the stability of the MOF.

In this chapter, we develop a computational method to determine the most thermodynamically stable polymorph of a nanoporous material among a collection of candidate structures using a combination of well-established free energy simulation methods. We demonstrate the application of our method using the MOF ZIF-8, whose structure consists of Zn^{2+} atoms tetrahedrally coordinated to 2-methylimidazole (mIm) linkers. ZIF-8 crystallizes in the sodalite (SOD) topology after hydro- or solvo-thermal synthesis. Recent studies have reported short synthesis times for ZIF-8 at ambient conditions using small molecules such as methanol[126,195] and water[196] as solvents compared to the bulkier dimethylformamide (DMF) solvent and high temperatures used in the original synthesis. In this chapter we consider the relative thermodynamic stability of the hypothetical Zn $(mIm)_2$ polymorphs predicted by Baburin et al.[183] in the presence

of methanol as a prototypical solvent. We also present similar results for solvation by butanol. Although the solvothermal conditions chosen for this study are relatively mild, this methodology can be extended to other solvothermal conditions.

5.2 Theory

To study the relative free energy differences of MOFs under solvothermal conditions, a computational method is needed that can accurately describe the free energy of immersion and the configurational free energy of the framework. Our method uses thermodynamic integration (TI)[174,175] or osmotic framework adsorbed solution theory (OFAST)[197-203] to calculate the free energy of immersion, ΔG_{imm}, of the framework. ΔG_{imm} is the energy associated with immersing the empty framework into a bulk fluid phase under isothermal conditions.[105] The configurational free energy, G_{conf}, is calculated in the harmonic approximation based on the minimum potential energy and vibrational density of states (VDOS) of the framework. By invoking this approximation, it is assumed that all flexible degrees of freedom of the empty and solvated framework can be represented as harmonic oscillators. Once these free energies have been tabulated for multiple structures, the thermodynamic cycle below is used to extract the free energy difference between polymorphs in the presence of solvent, ΔG_{tot}:

$$\Delta G_{tot,1-2} = \Delta\Delta G_{imm,1-2} + \Delta G_{conf,1-2}$$

$$\Delta G_{tot,1-2}(Z_1, Z_2) = \frac{\Delta G_{imm,2}(Z_2)}{Z_2} - \frac{\Delta G_{imm,1}(Z_1)}{Z_1} + \frac{G_{conf,2}(Z_2)}{Z_2} - \frac{G_{conf,1}(Z_1)}{Z_1} \quad (5.1)$$

where ΔG_{imm} (G_{conf}) is the free energy of immersion (configurational free energy) of the MOF and Z_i is the number of formula units in structure *i*. The free energies must be normalized by the number of formula units (1 formula unit (Z) = $Zn(mIm)_2$) present in each structure to create a suitable basis for comparison. The thermodynamic cycle used in our study is shown in Figure 5.1.

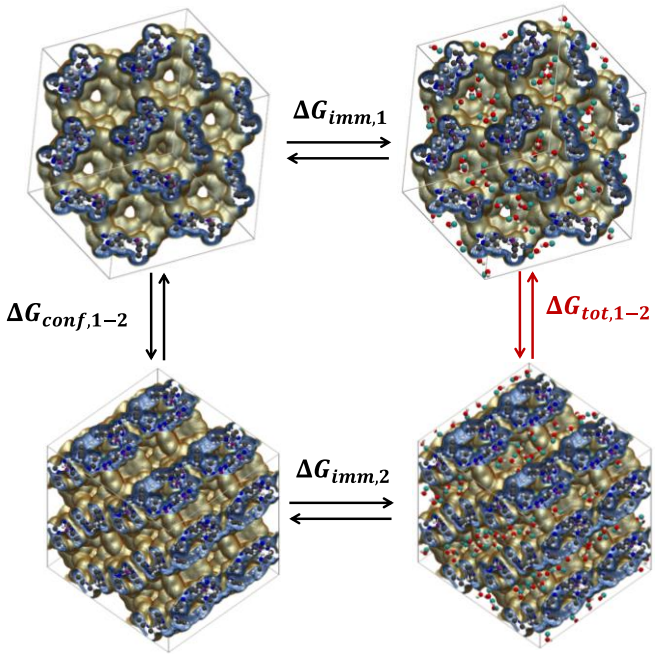

Figure 5.1 Schematic of the thermodynamic cycle used to determine the free energy difference between solvated polymorphs at ambient conditions, ΔG_{tot}. The top (bottom) framework is the primitive simulation cell of $Zn(mIm)_2$ in the SOD (DFT) topology. The images on the left (right) show the empty (solvated) frameworks. The C (CH_3) atoms of the framework (methanol) are shown in grey (cyan), N in blue, O in red, Zn in purple, and H in white.

5.3 Computational Methods

This section describes the various computational methods used to compute the free energies involved in the thermodynamic cycle described in the previous section. Interaction parameters and point charges were assigned to the framework atoms based on our previous calculations for ZIF-8.[204] An analysis by Watanabe et al.[67] has shown that

using fixed point charges in describing framework flexibility in ZIF-8 is a good approximation.

Thermodynamic integration (TI) is a simulation technique that uses MD simulations to compute ΔG_{imm}.[205,206] TI has been used, for example, to study the solvation of biomolecules[207] and carbon nanotubes[208,209] under various solvothermal conditions. Our calculations, however, are the first to extend the TI method to examine the solvation of a porous material of infinite extent. In our application of TI, the integration path is formed by annihilating the pairwise interactions between the solvent and framework atoms. This is achieved using Kirkwood's coupling parameter method:[210]

$$U(\lambda) = (1-\lambda)U_I + \lambda U_{II} \tag{5.2}$$

where λ is the coupling parameter that relates the two reference states. In our calculations, these states are represented by the empty (λ=0, U = U_I) and solvated (λ=1, U = U_{II}) frameworks. Using this methodology, ΔG_{imm} can be obtained by integrating over the path connecting these two states:[208]

$$\Delta G_{imm} = \int_{\lambda=0}^{\lambda=1} \left\langle \frac{\partial U(\lambda)}{\partial \lambda} \right\rangle_{\lambda} \partial\lambda \tag{5.3}$$

where U is the potential between the guest molecules and the framework and <⋯> denotes an ensemble average computed over the course of an NPT MD simulation for a fixed value of λ. The number of guest molecules present in the solvated framework is determined using GCMC calculations under equivalent thermodynamic conditions (T, P) as those specified in the NPT MD simulations for the TI method. Because the TI method includes the effect of framework flexibility, these GCMC simulations must also include this effect to give valid results for the guest molecule loadings. In Chapter 4 we showed that framework flexibility has a negligible effect on the adsorption uptake of alcohols at

high pressures in hydrophobic ZIFs using the hybrid GCMC/MD technique[211]. As a result, we assumed that the framework atoms were held rigid during these GCMC simulations performed in this chapter.

The application of the TI method to our system requires annihilating the electrostatic and Lennard-Jones (LJ) interactions between the solvent and MOF. The simultaneous annihilation of these potentials ($\lambda \rightarrow 0$) can result in cases where the electrostatics overwhelm the LJ interactions and allow the overlapping of atoms before the repulsive contribution of the LJ potential can take effect.[212] This effect can produce singularities during the integration of the equations of motion and calculation of the ensemble average in Equation 5.3. These issues were avoided in our calculations by decoupling the electrostatic and LJ interactions.[207,212] A similar effect is also observed when annihilating the LJ interactions, as the typical interatomic spacing decreases while the forces on the atoms rapidly increase as λ approaches zero.[212] An efficient approach to annihilating the LJ interactions is to employ a "soft-core" LJ potential that increases the curvature of the repulsive part of the conventional LJ potential and reaches a finite value at $\lambda = 0$.[213,214] The soft-core model used in our study has the same form as implemented in the GROMACS[215] simulation software:

$$U_{sc}(\lambda, \mathrm{r}) = (1-\lambda)U_I(r_A) + \lambda U_{II}(r_B) \tag{5.4}$$

with r_A and r_B given by:

$$r_A = (\alpha\sigma^6\lambda^p + r^6)^{1/6} \tag{5.5}$$

$$r_B = (\alpha\sigma^6(1-\lambda)^p + r^6)^{1/6} \tag{5.6}$$

where U_{sc} is the scaled potential, U is the conventional LJ potential, and σ is the LJ collision diameter. The maxima in the $\langle dU_{sc}/d\lambda \rangle$ curve corresponds to the point in configuration space where the solvent and framework atoms begin to overlap. The

adjustable parameters p and α control the shape of this curve and were set to p = 1 and α = 0.85 in our simulations to ensure sufficient sampling of phase space between the empty and solvated framework states. A preliminary investigation showed that an even λ spacing of 0.05 (0.1) proved to give accurate results for annihilating the LJ (electrostatic) interactions compared to clustering λ values near the maxima of the $<dU_{sc}/d\lambda>$ curve. An example of the results used to determine free energy differences for the LJ and electrostatic transformations using TI is shown in Figure 5.2.

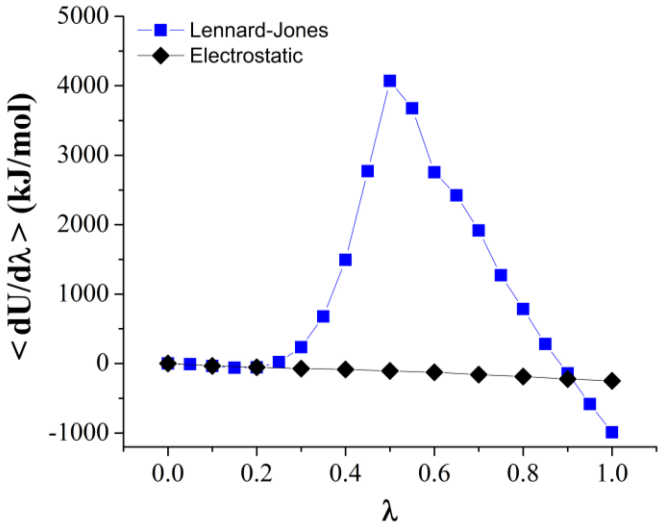

Figure 5.2 Thermodynamic integration (TI) curves used in our study to compute ΔG_{imm} by separately annihilating the Lennard-Jones and electrostatic interactions between methanol and the $Zn(mIm)_2$ (SOD) framework using NPT MD simulations at T = 25°C and P = 101.3 kPa. The solid lines are drawn to guide the eye.

The OFAST method is an alternative to TI that has been used to study structural changes due to adsorption of guest molecules in flexible nanoporous solids.[197-203] In OFAST, the free energy of immersion of the framework is calculated using:[216]

$$\Delta G_{imm} = -RT \int_0^f \frac{n^e(f)}{f} df \qquad (5.7)$$

where n^e is the excess amount of guest molecules adsorbed in the framework and f is the fugacity of the bulk fluid phase. At low fugacities, the excess amount adsorbed is equal to

the absolute amount adsorbed. As in earlier applications of OFAST,[197,201-203] the absolute guest molecule loadings were calculated using conventional GCMC simulations assuming a rigid MOF framework. Employing the rigid framework approximation in these simulations neglects the contribution of framework flexibility to the stability of the solvated framework. This effect is explicitly included in our ΔG_{imm} calculations using the TI method. We discuss the strength of this effect in Section 5.4 below.

The free energy of the empty framework, G_{conf}, was calculated using the VDOS method. This method has been applied to study the swelling behavior of aluminosilicate nanotubes upon water adsorption[217] and in the computation of free energies of several phases of elemental sulfur.[218] In the VDOS method, G_{conf} is calculated in the harmonic approximation using:[219]

$$G_{conf}(T,P) = U_{conf} + \frac{1}{2}\int_{\nu=0}^{\nu_{max}} h\nu D(\nu)\,d\nu + k_B T \int_{\nu=0}^{\nu_{max}} D(\nu)\ln(1 - e^{-\frac{h\nu}{k_B T}})\,d\nu + PV \quad (5.8)$$

where U_{conf} is the minimum potential energy, ν is a vibrational frequency, and $D(\nu)$ is the VDOS of the framework. The VDOS of the framework was calculated from a short NVT MD trajectory of the empty framework using the specden plug-in package in the VMD software[220]. The VDOS plots for five $Zn(mIm)_2$ polymorphs are shown in Figure D.1. Additional corrections to the free energy of the empty framework may be needed if anharmonic modes are important, but we have not attempted to include these effects in this chapter.

5.4 Results and Discussion

In this section, we demonstrate the application of the TI, OFAST and VDOS methods to study the relative free energies of a set of hypothetical $Zn(mIm)_2$ polymorphs under solvothermal conditions. These simulations were performed under ambient conditions (P = 101.3 kPa, T = 25°C) to simulate the actual solvothermal synthesis conditions for ZIF-8[25,26]. We selected four structures from the 24 hypothetical $Zn(mIm)_2$ polymorphs generated by Baburin et al.[183] for this analysis due to the high computational cost associated with the TI calculations. From these structures, the CAG and DFT topologies have been observed experimentally by Park et al.[119] in $Zn(Im)_2$ structures and the UNH and PCL are purely hypothetical topologies. Below, we examine the relative stability of these polymorphs compared to the experimentally observed $Zn(mIm)_2$ (SOD) structure using the GAFF force field[36,153,204] to describe the bonded and non-bonded interactions of the framework atoms. This force field was found to give excellent agreement compared to the energy-minimized lattice constants predicted by the DFT calculations of Baburin et al.[183] (see Table D.1).

We begin our analysis by comparing our predictions for the different contributions to the relative configurational energies of each polymorph, as shown in Table 5.1. Our results predicted that the contributions of the VDOS and pressure-volume terms to ΔG_{conf} were small in each case. As a result, ΔU_{conf} and ΔG_{conf} were approximately equivalent for all polymorphs. This observation suggests (although it does not prove) that anharmonic corrections to ΔG_{conf} are likely to be unimportant in this analysis. The results in Table 5.1 also show that ΔU_{conf} for each of the empty frameworks is unfavorable by at least ~19 kJ/mol per formula unit (f.u.) relative to the $Zn(mIm)_2$

(SOD) structure. These results are in conflict with the configurational potential energies predicted by Baburin et al.[183] using density functional theory (DFT) calculations. A comparison of the relative configurational energies predicted using these two methods for the entire set of hypothetical polymorphs is shown in Figure D.2.

The disagreement between DFT and classical simulations for the prediction of ΔU_{conf} may be strongly influenced by the GAFF force field used in our calculations, which was parameterized to favor a tetrahedral geometry for each ZnN_4 cluster.[36] While the experimentally observed $Zn(mIm)_2$ (SOD) structure exhibits this tetrahedral configuration, the hypothetical polymorphs involve a significant energy penalty within the GAFF force field for adopting a different geometry. Although the GAFF force field can accurately describe the lattice constants of the polymorphs, it gives poor agreement for the distribution of bond lengths and angles for the ZnN_4 cluster (see Table D.1) compared to the DFT energy-minimized structures. It is worth noting that the widely used DREIDING[221] force field was also parameterized to favor this geometry and gave similar ΔU_{conf} values compared to the GAFF force field in our preliminary calculations.

Table 5.1 Comparison of the configurational potential and free energy differences (P = 101.3 kPa, T = 25°C) for four $Zn(mIm)_2$ polymorphs relative to the $Zn(mIm)_2$ (SOD) structure using the GAFF force field.

Polymorph	ΔU_{conf} **(kJ/mol/f.u.)**	ΔG_{conf} **(kJ/mol/f.u.)**	ΔG_{tot} **(kJ/mol/f.u.)**	
			OFAST	**TI**
SOD	0.0	0.0	0.0	0.0
DFT	19.5	19.9	21.4	24.6
CAG	27.6	27.9	31.0	30.1
PCL	36.7	36.8	37.2	38.1
UNH	65.4	66.0	69.6	71.1

Table 5.1 also compares the predictions of the ΔG_{tot} relative to the $Zn(mIm)_2$ (SOD) structure using OFAST and TI. The predictions using each method are in good agreement, with a maximum deviation of ~3 kJ/mol/f.u. If TI and OFAST calculations were performed with the same degrees of freedom, they should give identical results. Our TI calculations included relaxation of the ZIF frameworks due to the presence of solvent molecules. As in previous applications of OFAST, [18,22-24] however, our results were based on holding each framework rigid. Additional TI simulations using rigid frameworks produced results for ΔG_{imm} that were in close agreement with OFAST. It is clearly more physically correct, however, to include the framework degrees of freedom in these calculations. The OFAST results in Table 5.1, therefore, should be viewed as an approximation to the more physically accurate TI results.

Although the VDOS/TI calculations are more rigorous than our OFAST calculations for the prediction ΔG_{imm}, we estimate that the VDOS/TI method requires an

order of magnitude more CPU time compared to OFAST. In addition, the TI method can only be used to compute ΔG_{imm} at a molecule loading corresponding to a single bulk phase condition. In contrast, an OFAST calculation involves calculating a full adsorption isotherm. This implies that the relative stability of polymorphs can be approximated using OFAST at a range of solvent fugacities with no additional computational effort. Figure 5.3 shows ΔG_{tot} calculated in this way for four $Zn(mIm)_2$ polymorphs relative to the experimentally observed $Zn(mIm)_2$ (SOD) structure using OFAST. In this figure, the bulk fluid pressures were normalized by the saturated vapor pressure of methanol. As a result, a relative pressure of unity in this figure corresponds to a reservoir of pure methanol in a bulk liquid phase. These results indicate that the SOD topology is the most stable structure (for the GAFF force field) over the entire pressure range investigated in our study.

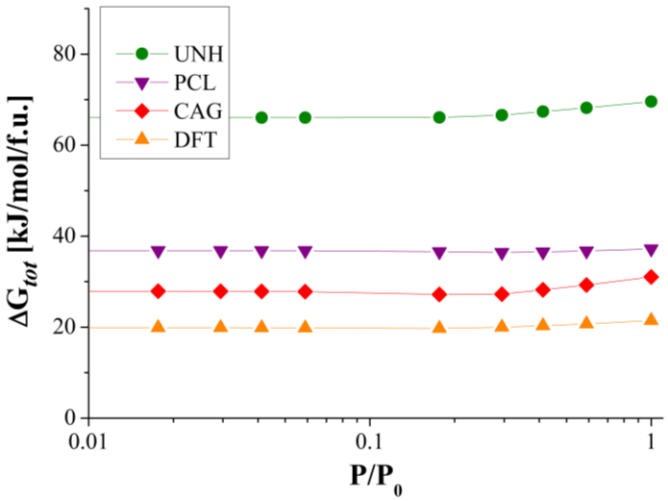

Figure 5.3 Comparison of the total free energy difference (ΔG_{tot}) for four $Zn(mIm)_2$ polymorphs relative to the $Zn(mIm)_2$ (SOD) structure in the presence of methanol at T = 25°C using OFAST.

Having established that the computationally efficient OFAST approach gives results in close agreement with the more accurate TI method for the solvated $Zn(mIm)_2$ polymorphs, we used OFAST to examine a larger set of polymorphs than the 4 examined above. Figure 5.4 shows ΔG_{imm} as a function of accessible pore volume for a set of 24 hypothetical polymorphs compared to the $Zn(mIm)_2$ (SOD) structure using the OFAST method. The pore volumes of the polymorphs were calculated based on the DFT energy-minimized structures of Baburin et al.[183] using the helium probe insertion technique[105,106]. As opposed to the enthalpy of solvation, which is a function of guest molecule loading, the ΔG_{imm} reported here represents an integrated effect of solvation and is a function of only the bulk fluid phase fugacity and composition (at constant T). This formalism allows us to directly compare the effect of solvation in different polymorph systems directly. The data in Figure 5.4 shows that ΔG_{imm} increases in magnitude with the pore volume of the framework for each polymorph to a maximum of ~12 kJ/mol. Similar calculations using butanol as solvent (Figure D.3) indicated that the ΔG_{imm} of butanol in the polymorphs was similar to methanol, which is due to a competition between enthalpic and entropic contributions to the free energy. These results shown here indicate that the effect of solvation varies significantly for frameworks with different structural topologies.

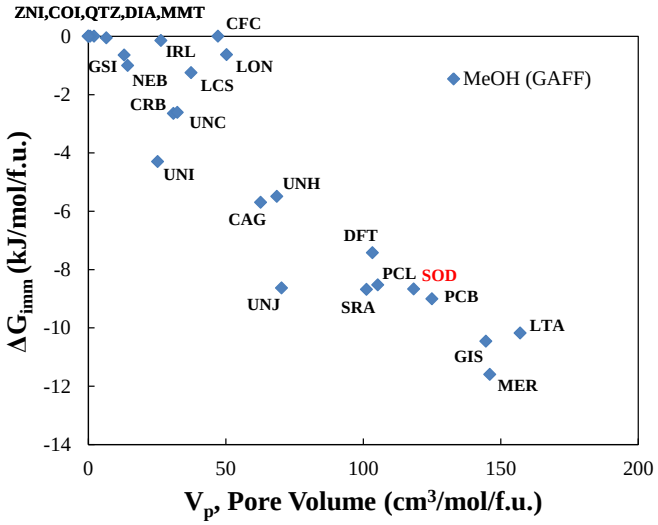

Figure 5.4 Free energy of immersion (ΔG_{imm}) of methanol versus accessible pore volume for 25 $Zn(mIm)_2$ polymorphs at T = 25°C.

To test whether the ΔG_{imm} could have an effect on the ordering of metastable polymorphs, we compared the relative difference of the configurational, immersion, and total free energies of all of the polymorphs, as shown in Figure 5.5. For this analysis we used the configurational energies predicted using DFT in the study of Baburin et al.[183] rather than the GAFF force field due to its ability to accurately describe the full range of geometries that exist for the $Zn(mIm)_2$ polymorphs. The development of a force field that can describe the framework energetics of the polymorphs is beyond the scope of this study but may be addressed in future work. As shown in Figure 5.5, the DFT calculations of Baburin et al.[183] predicted that the ZNI topology is the most stable topology by >15 kJ/mol compared to most other polymorphs. Our simulations predict that solvation by methanol stabilizes many of the non-ZNI topologies by ~5-10 kJ/mol/f.u. This result is reasonable due to the relatively weak interaction of methanol with the hydrophobic $Zn(mIm)_2$ framework. It has been shown that ΔG_{imm} makes a larger contribution to

framework stability in systems with coordinatively unsaturated metal sites[222]. Although solvation by methanol does not change which polymorph is the most stable, the energetic ordering of metastable polymorphs is altered when solvation effects are included. If only G_{conf} of the empty frameworks was considered, the 5 polymorphs with the lowest energy polymorphs would be ranked (based on DFT-calculated energies[183]) as ZNI < CRB < COI < DIA < UNI. Once solvation is included, this ordering changes to ZNI < CRB < SOD < COI < UNI. These results support the notion that solvation can play a role in determining the thermodynamic stability of different framework topologies.

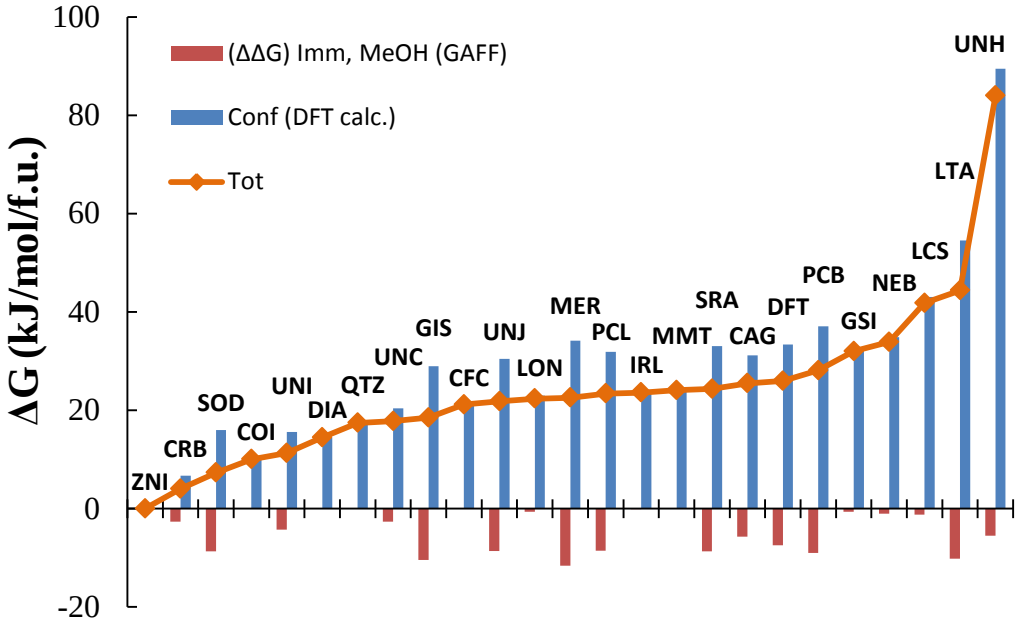

Figure 5.5 Comparison of the relative difference of the configurational (ΔG_{conf}), immersion ($\Delta\Delta G_{imm}$), and total (ΔG_{tot}) free energies for 24 hypothetical $Zn(mIm)_2$ polymorphs compared to the $Zn(mIm)_2$ (SOD) structure using OFAST.

5.5 Conclusion

The relative free energy difference of a set of hypothetical $Zn(mIm)_2$ polymorphs was investigated with free energy calculations using the OFAST, TI, and VDOS methods. This chapter describes the first theoretical investigation of the stability of MOF materials under solvothermal conditions. Our simulations predict that the difference in ΔG_{imm} is small compared to ΔG_{conf} for all polymorphs relative to the most stable structure. However, we also find that solvation affects the energetic ordering of metastable polymorphs. Our calculations indicate that the OFAST and TI methods are in good agreement in the prediction of ΔG_{imm} of the framework for these materials. Due to its computational efficiency and accuracy, the OFAST method is therefore a useful tool for preliminary calculations of ΔG_{imm} in situations where contributions from framework flexibility are expected to be small.

Although this chapter focused on the stability of the framework in the presence of pure methanol or butanol, these free energy simulation methods can be extended to examine the multicomponent mixtures of polar solvents typical employed in MOF synthesis procedures. The OFAST method can efficiently calculate ΔG_{imm} for pure adsorbing species, however this method requires the computation of multicomponent isotherms to study mixture adsorption which increases its computational cost. The TI method, however, can be directly extended to mixture adsorption and explicitly incorporates the effect of framework flexibility on ΔG_{imm}. Therefore, this method may provide a better alternative for calculating ΔG_{imm} under realistic synthesis conditions involving solvent mixtures. Overall, these methods will be useful for studying the

stability of a wide range of nanoporous materials with different structural topologies under various solvothermal conditions.

CHAPTER 6

CRYSTAL-SIZE-DEPENDENT STRUCTURAL TRANSITIONS IN NANOPOROUS CRYSTALS: ADSORPTION-INDUCED TRANSITIONS IN ZIF-8[6]

6.1 Introduction

Nanomaterials can have desirable properties that are not possible with bulk materials such as enhanced optical and dielectric properties,[223,224] and higher stiffness and strength.[225] For example, nano-sized catalyst particles offer higher external surface area and therefore increased catalytic activity.[226] Nano-sized molecular sieve particles are often preferred over micron-sized particles to fabricate advanced separation devices (e.g. nanocomposite hybrid membranes), as thinner membranes and more attractive membrane productivity are achievable with smaller-sized particles.[227] Accordingly, understanding the differences between nanomaterials and bulk phases and how to take advantage of these differences for practical applications are of great importance.

Zeolitic imidazolate frameworks (ZIFs) are a recently developed class of porous crystalline solids formed by tetrahedrally coordinated transition metal ions (usually zinc and cobalt) bridged by imidazolate linkers.[228,229] Compared with zeolites that exhibit relatively rigid frameworks, rotation of imidazolate linkers makes ZIF's framework more flexible and more susceptible to structural transitions induced by uptake of guest

[6] Material in this chapter has been previously published as Gee, J. A.; Zhang, C.; Sholl, D. S.; Lively, R. P. Crystal-Size-Dependent Structural Transitions in Nanoporous Crystals: Adsorption-Induced Transitions in ZIF-8. *The Journal of Physical Chemistry C* **2014**, *118*, 20727-20733.

molecules.[230] Recent experimental studies[148,231-235] suggest that ZIFs may have advantages relative to conventional zeolites as adsorbents and membrane materials for advanced separations.

ZIFs' bulk-phase properties are usually measured on micron-sized particles each comprising at least thousands of unit cells.[228] However, nano-sized ZIF particles comprised of as few as several unit cells may be preferred over micron-sized ZIF particles in applications where rapid mass transfer is needed. Currently, limited knowledge is available on the effects of crystal size on framework flexibility and structural transition for ZIFs/MOFs and other porous solids. Sakata and co-workers[236] studied a shape memory effect of flexible crystalline porous coordination polymers (PCPs) as a result of crystal downsizing. Kumari and co-workers[237] observed substantial differences on sorption capacity within micron- and nano-sized ZIF-8 crystals. A fundamental understanding of such effects may be critical to the design of nano-sized nanoporous materials with desirable properties. One useful example of a structural transition in a ZIF is the change of crystal structure of ZIF-8 induced by adsorption of N_2.[230] This transition causes an appreciable "step" in the N_2 adsorption isotherm of ZIF-8. Similar transitions in other ZIFs can be induced by adsorption or other factors such as external pressure,[238] although it is important to note that the presence of a step in the isotherm is not necessarily evidence of a structural transition and vice versa.

In addition to experimental studies, several groups have used molecular simulations to examine framework flexibility and structural transitions in the bulk ZIF-8 framework. Haldoupis et al. combined *ab initio* Molecular Dynamics (AIMD) and classical simulations to predict the effect of framework flexibility on the diffusion of CH_4

and CO_2 in ZIF-8.[239] Several groups have developed classical force fields to describe the static and dynamic properties of ZIF-8 based on the AMBER and DREIDING force fields.[34,35,240,241] Zhang et al. recently developed a classical force field to describe the N_2-induced structural transition of ZIF-8.[242] These authors demonstrated that this force field was able to accurately reproduce the structural transition first observed experimentally by Fairen-Jimenez et al.[230] using hybrid Grand Canonical Monte Carlo (GCMC) simulations.

The osmotic framework adsorbed solution theory (OFAST) is a useful simulation method that has been used to study structural deformations in flexible nanoporous solids.[243,244] OFAST predicts the equilibrium-favored system based on adsorption simulations in a series of metastable frameworks. This technique has been a critical tool for understanding and predicting adsorption-induced structural transitions of flexible MOFs. All previous applications of OFAST have been to bulk materials. Some recent work examining the spatial extent of adsorption stresses in nanoporous crystals has focused on introducing coarse-grained simulation techniques.[245] Although this work has been successful in describing transitions in bulk materials, it is unclear how these techniques could be extended to include surface effects in nanoparticles.

In this chapter, we investigated the effect of crystal size on the structural transitions of ZIF-8 by applying OFAST to simulate an entire ZIF-8 nanoparticle. To test the validity of this approach experimentally, ten ZIF-8 samples with distinct crystal diameter (10 nm-324 μm) were synthesized. The samples were characterized with N_2 physisorption and experimental isotherms were compared with OFAST-simulated N_2 physisorption isotherms of ZIF-8 nano-particles and the ZIF-8 bulk phase.

6.2 Simulation Details

The ZIF-8 nanoparticle used in our simulations was constructed by clipping a sphere from the center of a large simulation cell of the bulk structure, as shown in Figure 6.1. This procedure was motivated by the roughly spherical shape of the smallest nanoparticles observed using electron microscopy (Figure 6.2) and qualitatively similar XRD pattern of these particles and the bulk material (Figure E.1). We should note that our model can handle other crystal shapes and orientations as long as the crystal structure is known. Our simulated nanoparticle has half the diameter of the smallest experimental crystal; this was the largest size that was readily feasible. We will show below that this model is able to effectively reproduce trends in the adsorption isotherm observed for varying particle sizes. Any under-coordinated imidazole groups (metal atoms) at the surface of the nanoparticle were terminated with "capping" hydrogen atoms (imidazole groups). Recent studies have found evidence for NH-terminated imidazole groups at the surface of $Zn(Im)_2$-containing systems as well as a combination of N- groups, OH groups, and under-coordinated Zn atoms.[246,247] We assume that any unstable ions at the surface will quickly terminate with hydroxyl or imidazole ions present in the aqueous synthesis conditions. The effect of different nanoparticle surface terminations on adsorption uptake is discussed in more detail later in this chapter.

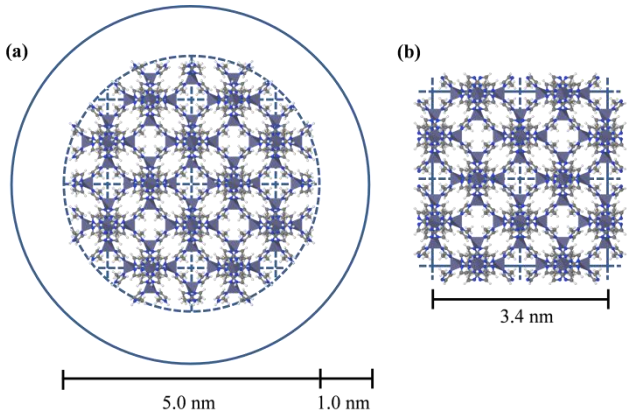

Figure 6.1 Schematic comparison of the (a) non-periodic nanoparticle and (b) periodic bulk ZIF-8 systems prior to force field energy minimization, shown to scale. The unit cells comprising the simulation cell of the bulk structure are bounded by dotted blue lines and are superimposed in the nanoparticle to guide the eye. The domain over which GCMC moves were performed for both structures is indicated by a solid line. The C atoms of the framework are shown in gray, N in blue, H in white, and Zn as purple tetrahedra.

Adsorption isotherms for the nanoparticle and bulk systems were simulated using grand canonical Monte Carlo (GCMC) simulations as implemented in RASPA.[248] All structures were force field energy-minimized prior to these simulations. The GCMC simulations used an equilibration (production) period of 1×10^4 (2.5×10^4) cycles. The GCMC moves were restricted to a spherical shell encompassing the entire nanoparticle and included an additional 1.0 nm shell to capture adsorption in extracrystalline space. Any GCMC move that allowed an adsorbate to leave the system was rejected. The amount of adsorbed molecules was calculated using a fixed cut-off that was approximately equal to the radius of the particle.

The bonded and non-bonded force field parameters used to describe the bulk structure were the same as those used in the study of Zhang et al.[242] We assumed that these parameters are able to describe the interactions in the nanoparticle with only minor

modifications to include the "capping" hydrogen atoms. The van der Waals interactions were modeled using a 12-6 Lennard-Jones (LJ) potential for both systems. The spherical cutoff radius for the LJ interactions was 16.5 Å (20 Å) for the bulk (nanoparticle). Analytical tail corrections were applied for the bulk system and the potential was truncated at the cutoff radius for the nanoparticle. The electrostatic interactions were calculated using Ewald summation for the bulk system and a Coulombic pairwise potential with a cutoff radius spanning the entire system for the nanoparticle. Periodic boundary conditions (PBCs) were applied for the bulk structure whereas finite boundaries were used for the nanoparticle. We used finite boundary conditions with a Coulombic potential for the nanoparticle because these conditions were found to give equivalent results to using PBCs and Ewald summation at reduced computational expense.

6.3 Experimental Methods[7]

Scanning electron microscopy (SEM) and transmission electron microscopy (TEM) were used to estimate crystal size of synthesized ZIF-8 samples. SEM images were obtained on a LEO 1530 field emission scanning electron microscope (LEO Electron Microscopy, Cambridge, UK). TEM images were obtained on a FEI Tecnai F30 high resolution TEM at 300 kV. Electron microscope images are shown in Figure 6.2, which reveal (truncated) rhombic dodecahedron shaped micro-crystals and spherical nano-crystals. Powder X-ray diffraction (PXRD) was used to confirm the crystal structure of synthesized ZIF-8 samples. XRD data were collected on a Phillips X'Pert X-Ray

[7] All experimental work reported in this chapter was performed by Dr. Chen Zhang in Dr. Ryan Lively's laboratory at Georgia Tech.

Diffractometer (using Cu Kα radiation, λ=0.154 nm at 45 kV and 40 mA). Experiments were carried out scanning from 2θ =5-40°. PXRD patterns of the synthesized ZIF-8 samples are shown in Figure E.1, which are in good consistency with the simulated pattern.

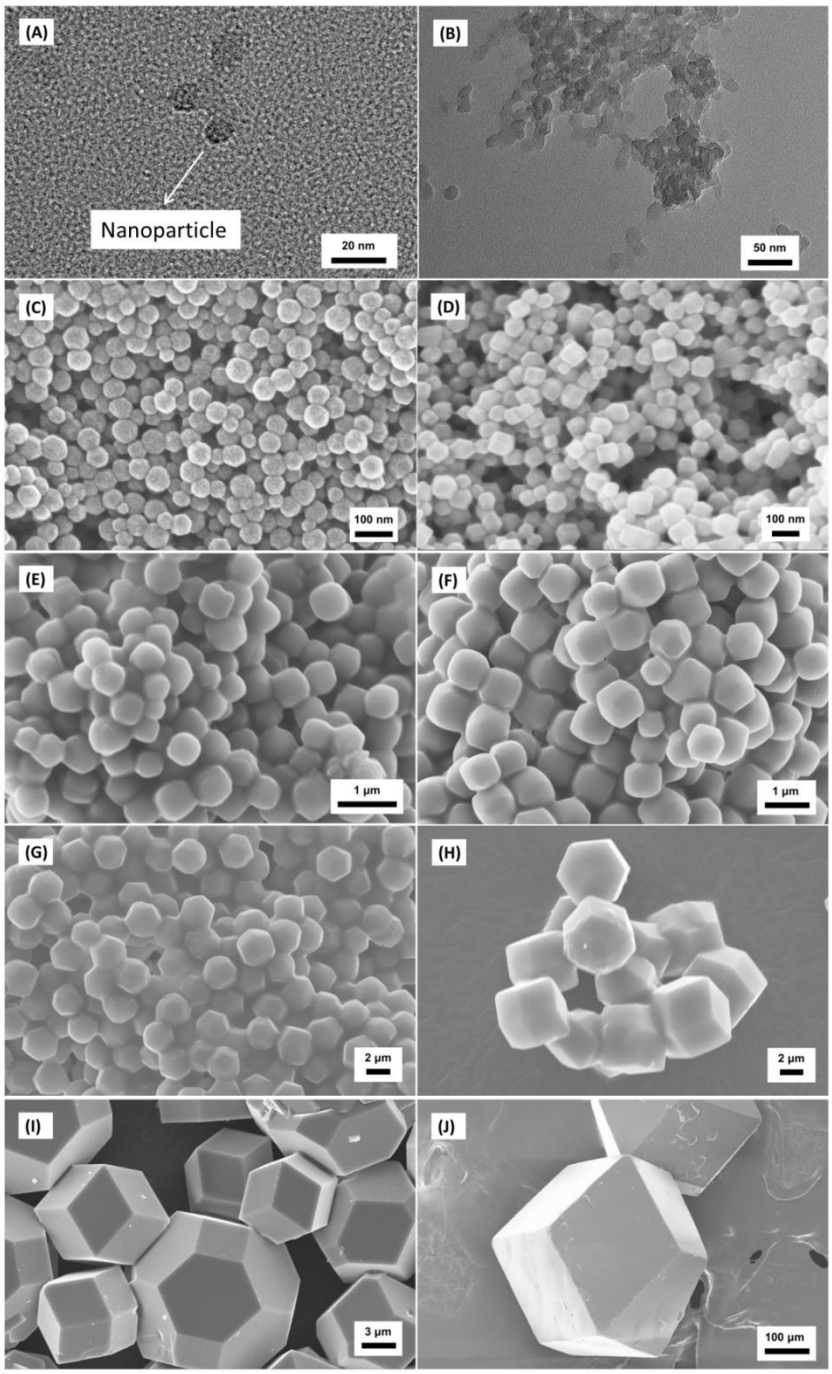

Figure 6.2 Electron microscope images of synthesized ZIF-8 samples (A) 10 nm (B) 18 nm (C) 52 nm (D) 92 nm (E) 540 nm (F) 1 micron (G) 3.4 micron (H) 7.6 micron (I) 15.8 micron (J) 324 micron. Figure 2 (C), (I), and (J) are reproduced from Zhang et al[148].

N_2 physisorption isotherms (77K) were measured with an ASAP 2020 physisorption analyzer (Micromeritics, Norcross, GA). Samples were degassed at 120-150°C for 12-16 hours prior to measurements. Figure E.2 shows N_2 physisorption isotherms of the ZIF-8 samples. N_2 molecules first adsorb in the pores through a multilayer formation and micropore filling mechanism at low relative pressure ($P/P_0<0.01$), as shown by the dramatic increase in sorption capacity. As the relative pressure is increased, adsorption continues on the crystal external surfaces until a "plateau" is reached for micron-sized crystals[249]. A further increase in sorption capacity takes place for nano-sized crystals close to the saturation pressure ($P/P_0=1$), which is believed to be condensation in the mesopores and macropores formed by agglomeration of nano-sized crystals. Brunauer-Emmett-Teller (BET) surface areas and micropore volumes were obtained from the N_2 physisorption isotherms and listed in Table E.1. The BET surface area was analyzed based on the consistency criteria[250], which was comparable (with the exception of 10 nm, 18 nm, and 52 nm sample) with the value of the commercial sample by BASF.

6.4 Results and Discussion

We applied the OFAST method to study the structural transition induced by N_2 adsorption in the bulk and nanoparticle structures by comparing results in the ZIF-8 low loading (LL) and high loading (HL) structures defined in the earlier work of Fairen-Jimenez et al.[230] Our model does not account for kinetic barriers or inhomogeneity between the LL and HL phases, although these effects might be captured using a mesoscopic model similar to the one proposed by Triguero et al.[245] As shown in Figure 6.3, our OFAST calculations predict that N_2 adsorption induces a structural transition in

bulk ZIF-8 at a relative pressure (P/P_0) of ~5×10^{-3}. This value is in good agreement with the hybrid GCMC results of Zhang et al.,[242] which predicted that the transition occurs over a P/P_0 range of 5×10^{-3}-1×10^{-2}. It is important to note that the agreement between the simulated and experimental bulk material (Figure 6.3) is not unexpected; this transition pressure was used to parameterize the Zhang et al. force field.[242] It should be noted that we observed another minor step in the experimental isotherm of the bulk materials at P/P_0~5×10^{-3}, which was consistent with the results of a previous study[251]. However, we were not able to simulate this effect using the Zhang et al. force field.

Our results in Figure E.4 show the grand potential Ω of the bulk ZIF-8 framework as a function of P/P_0. These calculations predict that the LL form of ZIF-8 is the equilibrium-favored structure at zero loading, in agreement with experimental observations. The calculated difference in free energy per formula unit between the empty LL and HL structures of ZIF-8 with the Zhang et al. force field[242] is ~1.8 kJ mol^{-1} Zn^{-1}, which is ~3 kT at T = 77 K. At high N_2 pressures the HL system becomes lower in free energy relative to the LL system due to the increased guest molecule loading in this system. This effect provides the thermodynamic driving force for the system to undergo the transition from the LL to HL structures.

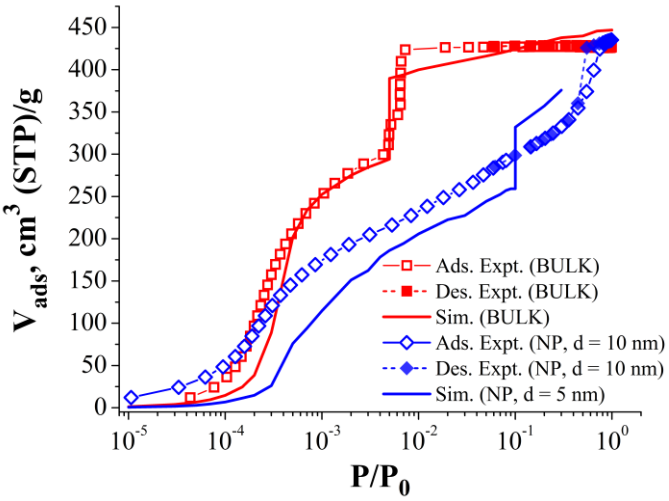

Figure 6.3 OFAST-simulated and experimental adsorption isotherms for N_2 in the ZIF-8 bulk and nanoparticle (NP) frameworks at T = 77 K.

Our simulated and experimental N_2 adsorption isotherms show that the adsorption uptake in the nanoparticle follows a substantially different trend than the bulk, as shown in Figure 6.3. The isotherm for the nanoparticle follows a Type II-like isotherm. The experimental isotherm also shows that capillary condensation occurs in the mesopores between the nanoparticles near P/P_0 = 1, although this effect is neglected in our simulations. The N_2 adsorption uptake in the nanoparticle is lower than in the bulk on a framework mass basis. It should be noted that this was contradictory with the results reported by Kumari et al.,[237] who observed much lower sorption capacity in micron-sized ZIF-8 crystals than nano-sized ZIF-8 crystals. It is speculated that such contradiction was due to the use of DMF for synthesis and washing the micron-sized ZIF-8 sample in the work of Kumari et al.,[237] which possibly led to partial activation[228]. Figure 6.3 shows that our simulated isotherms are in reasonable agreement with experiments until P/P_0 approaches ~1×10^{-1}. It is unclear why the adsorption uptake in the Henry's region is higher in the experimental d = 10 nm nanoparticle compared to the bulk material,

although this effect was also observed in the study of Sataka et al.[236] It is clear that the simulation data shows a step in adsorption isotherm at a P/P_0 of $\sim 1\times10^{-1}$, while the experimental data shows no evidence of such a transition. It was possible that the structural transition on the 10 nm sample was too subtle to be experimentally observed due to limited device sensitivity. Regardless of this disagreement, we still find that this method is able to describe the experimentally-observed trend of transition pressure versus particle size.

As mentioned previously, we were not able to simulate particle sizes larger than d = 5 nm due to computational limitations. However, we were able to evaluate the effect of decreasing particle sizes on the simulated transition behavior. Figure 6.4 shows the OFAST-simulated N_2 adsorption isotherms at T = 77 K for the bulk material, d = 5 nm and d = 2.5 nm nanoparticles. We observe that the smallest simulated nanoparticle (d = 2.5 nm) does not exhibit a step in the isotherm over the entire range of P/P_0. This result is similar to our experimental observation that a step is observed for the d = 20 nm particle but absent for the d = 10 nm particle and demonstrates that the transition pressure is very sensitive to particle size for smaller nanoparticles.

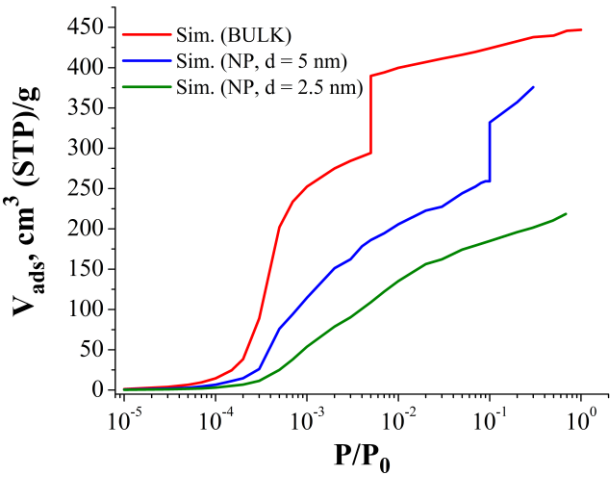

Figure 6.4 OFAST-simulated adsorption isotherms for N_2 in ZIF-8 bulk, d = 5.0 nm, and d = 2.5 nm particles at T = 77 K.

Although we assumed that the bulk material and nanoparticle have similar compositions, we also tested the sensitivity of our simulation results to alternate nanoparticle surface terminations. To examine this effect, we replaced the imidazole groups on the surface of the d = 5.0 nm nanoparticle with less bulky hydroxyl groups. As shown in Figure 6.5, the hydroxyl-terminated surface exhibits a similar transition pressure compared to the imidazole-terminated surface. This result is reasonable because the surface functional groups are far from the center of the nanoparticle where the adsorption uptake is maximal. Therefore, we expect that the effect of surface termination has a minor impact on the trends observed in our simulation analysis.

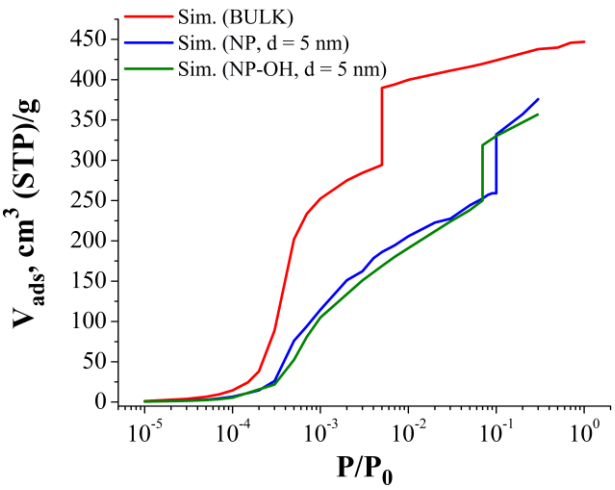

Figure 6.5 OFAST-simulated adsorption isotherms for N_2 in ZIF-8 bulk, d = 5.0 nm imidazole- and d = 5.0 nm hydroxyl-terminated (NP-OH) particles at T = 77 K.

To better understand the differences in adsorption uptake in the nanoparticle and the bulk materials we partitioned the adsorption uptake in the nanoparticle into "bulk-like" and surface regions. The bulk-like region was defined as any N_2 molecule lying within a radial distance of approximately one bulk ZIF-8 unit cell from the center of the nanoparticle. We observed that the adsorption uptake in the surface region is negligible compared to the interior at $P/P_0 < 10^{-3}$ (Figure E.5). The preferential adsorption in the bulk-like region at low pressures is due to the increased number of neighboring framework atoms compared to the surface. This effect leads to a decrease in nitrogen heat of adsorption at infinite dilution of ~1.5 kT at the surface relative to the interior. The suppressed adsorption uptake at the surface results in a lower transition pressure compared to the bulk-like region (Table E.2). This effect results in a reduced thermodynamic driving force for the transition in the nanoparticle over the entire range of bulk fluid pressures compared to the bulk.

Our calculations confirm that the different transition behavior was due to adsorption effects rather than structural properties of the nanoparticle compared to the bulk. Although the nanoparticle does not have a precisely defined formula unit as in the bulk structure, we can estimate the free energy difference between the LL and HL structures as ~1.9 kJ mol^{-1} Zn^{-1} in the nanoparticle. This value is similar to that observed for the bulk, indicating that this energy is not the primary driving force behind the difference in transition behavior. Moreover, an experimental Williamson-Hall analysis (Figure E.6) confirmed that the experimental nano-crystals did not exhibit differences in crystal strain from the bulk.

To further understand the effects of crystal size on structural transition of the material, an additional eight ZIF-8 samples were synthesized (Figure 6.2). Experimental N_2 adsorption and desorption isotherms of all ten ZIF-8 samples are plotted individually in Figure E.2. Adsorption isotherms are also shown in Figure 6.6 (A) with the relative pressure range 10^{-3}-10^{-1} shown in more detail in Figure 6.6 (B). A closer examination of isotherms in this range revealed very differently-shaped isotherms. For the 324 micron and 15.8 micron ZIF-8 sample, the structural transition featured a sharp step in the isotherm. As particle size decreased, this step became less defined and the structural transition gradually shifted to higher relative pressures. As the particle size started to fall into the nano regime (i.e. d<100 nm), the structure transition became much less obvious. A similar effect was observed by Sakata et al.,[236] although it was unclear whether their transition was suppressed by kinetic or thermodynamic limitations. For the smallest sample with d=10 nm, the isotherm was completely devoid of an observable step.

Additionally, magnification at the Henry's region is shown in Figure E.3; however, no size dependent features were observed at this region.

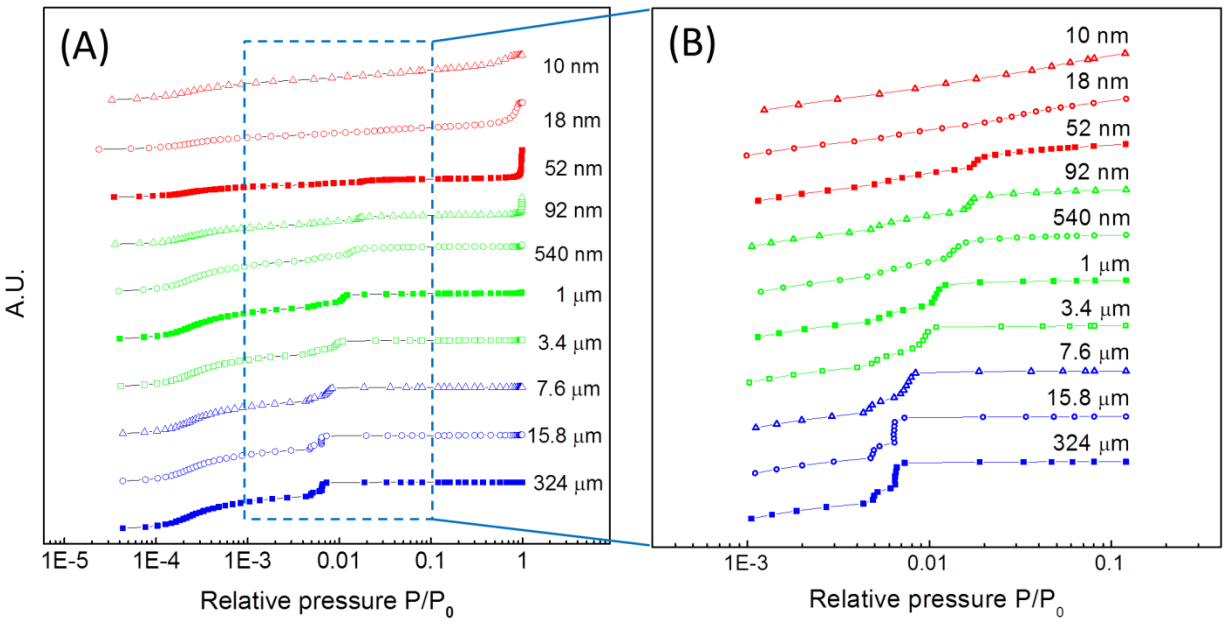

Figure 6.6 (A) Experimental N_2 adsorption isotherms (B) Experimentally observed crystal-size-dependent structural transitions. Isotherms are artificially offset for clarity.

Unfortunately, simulating N_2 physisorption isotherms of intermediate crystal sizes (18 nm, 52 nm, 92 nm, 540 nm, 1 μm, 3.4 μm, 7.6 μm, and 15.8 μm) would be overly computationally expensive. As a result, we were not able to directly compare OFAST-simulated isotherms with experimental data. Based on our findings for the 5 nm nanoparticle, we applied a simple core-shell model to examine the trend in transition pressure versus particle size. We assumed that the surface for each structure consisted of a shell the size of the smallest particle for which a transition was observed surrounding the interior of the particle. The transition pressure for each crystal size was a volume-weighted value between the transition pressures for the largest and smallest crystal size for which a transition was observed in experiments and simulations. As shown in Figure

6.7, this model gives reasonable agreement with the trends observed experimentally. We also observe that the difference in transition behavior compared to the bulk becomes more pronounced with smaller particle sizes, which was also shown in Figure 6.4. The discrepancies between the model and experiments may be due to differences in particle shape versus crystal size which are not included in the model. The disagreement between simulated and experimental transition behavior is likely due to a combination of experimental error and inaccuracy of the force field, which was parameterized based on adsorption uptake in the bulk material. Overall, these results give further indication that the effect of crystal size on transition pressure is due to the influence of the surface on the adsorption uptake in each crystal.

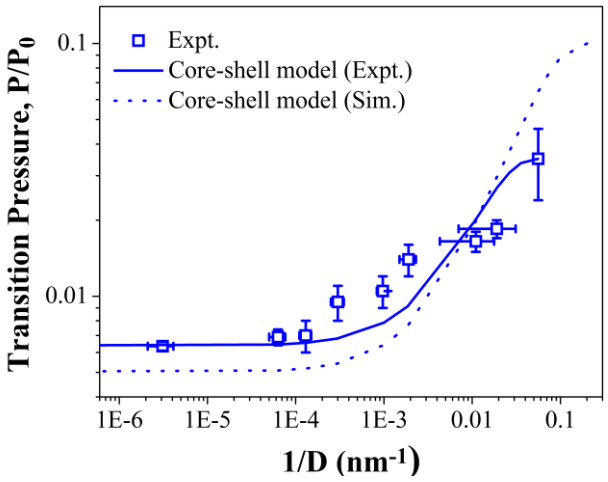

Figure 6.7 Transition pressure versus inverse crystal size from experiments and using a simple core-shell model with experimental and simulated transition pressures.

6.5 Conclusion

In this chapter, we investigated the crystal-size-dependent structural transition of ZIF-8 induced by N_2 adsorption using simulations and experiments. We developed a new methodology to simulate the adsorption and transition behavior of entire ZIF-8 particles at nanometer length scales. Our simulations predict that the structural transition occurs at a significantly higher pressure in the nanoparticle compared to the bulk. Our models show that this is caused by a destabilizing effect of the nanoparticle surface which results in reduced guest molecule loadings in this region. Our sensitivity analysis demonstrates that our models do not depend on surface termination but are strongly dependent on particle size for the smallest particles. We also developed a simple core-shell model to explain the trend in transition pressure versus particle size on length scales inaccessible to simulations. These models successfully predicted the trends in transition behavior observed using crystal-size dependent experimental measurements for this system. The methods developed in our study should be useful for understanding thermodynamically-controlled crystal-size dependent structural transitions in porous materials in general.

CHAPTER 7

CONCLUSION

7.1 Outlook

In this thesis, we demonstrated that molecular simulations can be used to guide experimental efforts towards promising materials for adsorption-based industrial separations. We also showed that simulations are a convenient tool for interpreting and validating experimental observations. Prior to this work, most simulation studies of MOFs in the literature focused on modeling separations of simple molecules such as H_2, CH_4, and N_2.[9,11] This thesis is among recent work that has extended previous methods to examine the separation of more complex molecules relevant to industrial separations.[17,38] We expect that simulations will continue to be useful in this area due to the large diversity of MOFs and the time-consuming nature of experiments.

A major challenge in accurately screening porous materials for separations is in reducing the computational expense of GCMC simulations. In Chapter 3, we showed that short GCMC simulations can be used to gain a qualitative prediction of the *p*-xylene selectivity of a given MOF. However, novel methods are currently being developed to improve the efficiency of GCMC simulations for dense systems. One example is the Configurational Bias/Continuous Fractal Component (CB/CFCMC) method of Dubbeldam et al.[252] We believe that further improvements in computational efficiency of these algorithms will result in higher accuracy predictions for computational materials screening efforts.

Another topic that deserves further attention is the development of improved force fields for describing complex adsorbate-MOF interactions. In Chapter 2, we showed that both generic and DFT-based force field can give qualitatively accurate results for the adsorption of C_8 aromatics in MOFs. The inclusion of dispersion corrections significantly improves the accuracy of DFT for systems with weakly adsorbing species. However, improved methods are currently being developed to include higher-level quantum mechanics corrections to these calculations. One such example is the DFT/CC method, which adds a correction to energies calculated using periodic DFT based on CCSD(T) calculations on small clusters of atoms.[253] This method has been shown to give good agreement with experiments for CO_2 adsorption in cation-exchanged zeolites.[61] The next generation of force fields for describing the adsorption of C_8 aromatics in MOFs will likely be based on high level quantum mechanics calculations and provide a better method of validating predictions from generic force fields.

We have shown in Chapter 2 that it is necessary to account for the effect of framework flexibility to accurately model industrial separations performed under high pressure or in the liquid phase. This effect can be included in our calculations by performing hybrid GCMC. A potential limitation of this approach is that generic force fields may not accurately describe the dynamics of the framework of interest. We described several methods for improving the accuracy of intramolecular force fields for MOFs based on experimental or *ab initio* methods in Chapter 2. The use of intramolecular force fields will continue to be useful for studying diffusion in MOFs and will eventually be used to model flexibility in adsorption simulations under industrial conditions.

7.2 Suggestions for Future Work

7.2.1 Extension of Screening Methodology to Other Systems

We chose to focus the efforts of our screening procedure in Chapter 3 on identifying MOFs for the industrial separation of *p*-xylene due to the enormous structural diversity available with MOFs. However, our methodology can in principle be generalized to identify promising materials in other porous materials such as zeolites or molecular crystals for this and similar separations. One challenge in modeling the separation of aromatic hydrocarbons in zeolites in particular will be in describing the interaction of the aromatic rings with cations in the structure. It is unlikely that generic force fields will be able to accurately describe these interactions because they were not included in their parameterization. Therefore, it may be necessary to develop a force field to describe these interactions using the DFT-based method developed in Chapter 2. These force fields should be validated based on a reliable set of experimental data prior to their use in any screening procedure. Once validated, these models can be implemented directly into our screening code and used to identify other porous materials for different separations.

7.2.2 Prediction of Adsorption Properties of Cyclic Hydrocarbons Using DFT/CC

As mentioned in Section 7.1, higher-level quantum chemistry methods such as DFT/CC are necessary to accurately describe dispersive interactions for weakly adsorbed molecules. The DFT/CC method could be implemented for these systems by developing correction curves for the CH_3 group of the C_8 aromatic molecules using the interaction of ethane dimers. These curves could then be combined with parameters for aromatic rings

developed by Bludský et al.[253] The physical accuracy of the predictions using this force field should be validated by comparing predicted and experimental properties similar to the methodology described in Chapter 2. The DFT/CC force field will provide a useful validation for systems in which generic force fields are not able to accurately describe experimental data.

7.2.3 Effect of Framework Flexibility on Adsorption in MOFs

In Chapter 2, we discovered that framework flexibility can significantly influence adsorption predictions in MOFs under industrially-relevant conditions. Although we only examined this effect in BDC-type MOFs, it is likely to be present in other types of MOFs due to the inherent flexibility of these materials. An interesting area of future work would be to develop a list of general guidelines for determining whether this effect will have a significant impact on adsorption in a given system. To achieve this goal, one could use simulations to probe a flexible degree of freedom of the framework and determine its effect on adsorption properties for several systems. Ultimately, this type of analysis could help to improve the efficiency of screening calculations by indicating systems which require additional modeling of framework flexibility to obtain accurate results.

We also suggest developing a methodology for accurately and efficiently simulating the effect of framework flexibility on MOFs. This effect can be included in our adsorption simulations by performing hybrid GCMC as described in Chapter 4. Unfortunately, it is not currently feasible to perform hybrid GCMC for complex adsorbates in industrial conditions due to the high computational cost of simulating adsorption in these systems. Therefore, it may be necessary to decouple the dynamics of

the framework and adsorption to increase computational efficiency. Due to the lack of available force fields for many MOF systems, it may be most convenient to use *ab initio* Molecular Dynamics (AIMD) to account for the framework dynamics in these systems. This method should provide more physically accurate predictions of adsorption in these systems at high loadings compared to simulations in the rigid MOF structure.

Appendix A

A.1 Comparison of Sim. and Exp. Lattice Constants

Table A.1 Comparison of the structural parameters for MIL-47, DMOF-1, UiO-66, and IRMOF-1 from DFT calculations and experiments.

Polymorph	Lattice parameter (Å)		
	a	b	c
MIL-47 (DFT)	6.79	16.64	13.37
MIL-47 (exp.)[14]	6.81	16.41	13.57
DMOF-1 (DFT)	11.05	11.05	9.58
DMOF-1 (exp.)[254]	10.93	10.93	9.61
UiO-66 (prim., DFT)	14.79	14.79	14.79
UiO-66 (prim., exp.)[255]	14.80	14.80	14.80
IRMOF-1 (prim., DFT)	18.45	18.45	18.45
IRMOF-1 (prim., exp.)[256]	18.27	18.27	18.27

Note: DFT energy-minimizations of the framework atoms were performed with the DFT-D2 method because structural optimization with DFT-D3 was not implemented in the version of VASP used in our study.

A.2 Assessment of D3FF Transferability and Convergence

A critical test of the performance of D3FF is its transferability to other MOFs. To test this aspect of our fitting procedure, we performed an analysis of the number of materials in the test set required to accurately describe adsorption data in 1,200 configurations in all four materials we considered (MIL-47, DMOF-1, UiO-66, IRMOF-1). The force field developed using adsorption data in MIL-47 alone as the test set gave a mean absolute deviation (MAD) of 3.59 kJ/mol compared to DFT-D3. This value is within ~0.5 kJ/mol of the MAD obtained using D3FF, which was developed using 1,200 configurations in all four materials in its test set. A similar result was found using the adsorption data in other MOFs as the test set (data not shown). Based on this analysis, we conclude that our method is transferable to other MOF materials despite the small number of MOFs used in our test set.

In our fitting procedure described in the main text, we were only able to probe a limited number of configurations of the xylene isomers due to the computational cost of the single point DFT energy calculations. Therefore, it was necessary to determine the required number of configurations required to obtain a force field that is converged relative to the DFT data. To test the convergence of D3FF, we calculated the isosteric heat of adsorption of *o*-xylene (Q_{st}^{0}) versus the number of configurations used in the parameterization for all four materials in our test set. Our results in Figure S3 indicate that the Q_{st}^{0} are converged for these materials after ~300 configurations. As a result, we used this number of configurations in our final parameterization procedure to ensure that the D3FF is consistent with the DFT data.

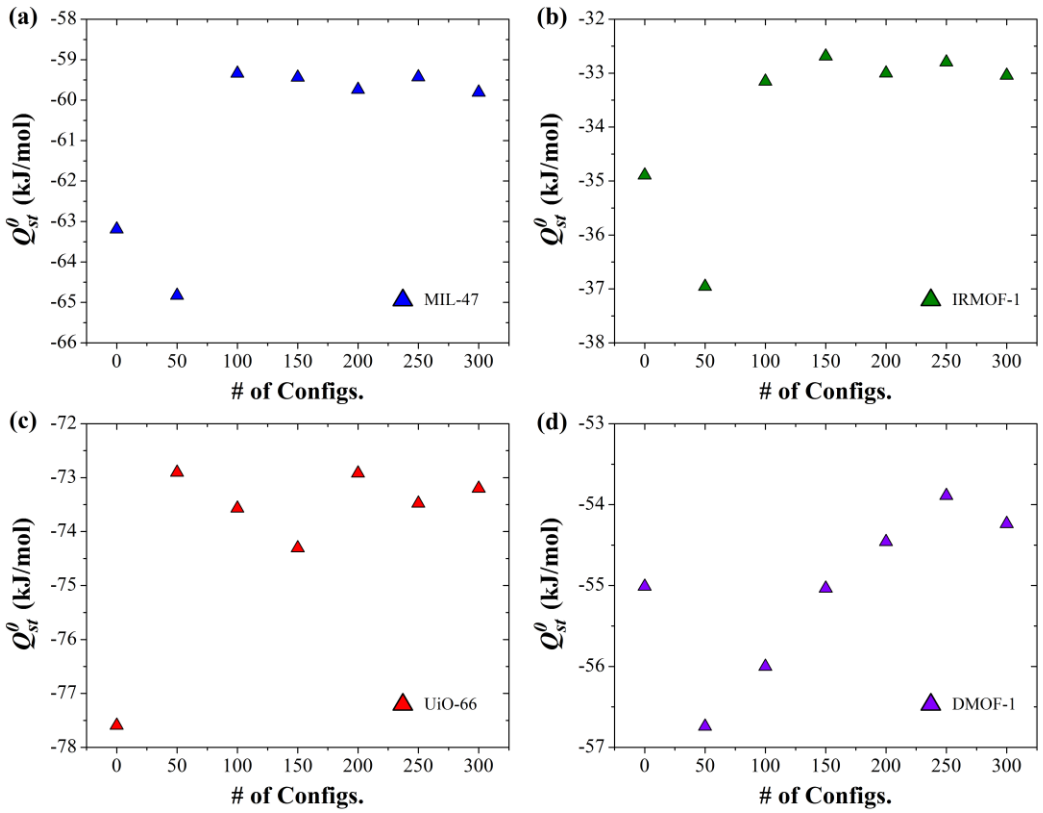

Figure A.1 Simulated heat of adsorption of *o*-xylene at infinite dilution (Q_{st}^{0}) versus number of configurations used in our force field parameterization.

A.3 Comparison of Contributions to Sim. Heats of Adsorption

In Figure 2.4 of the main text, we showed that the heat of adsorption versus loading for *ortho*-xylene showed different trends depending on the MOF under study. In Figure A.2, we provide a breakdown of the contributions to the total heat of adsorption from host-guest and guest-guest interactions. The trend we observe in this figure is that the heat of adsorption versus loading is dominated by guest-guest interactions in the case of MIL-47 and host-guest interactions in UiO-66. This difference can be explained by a confining effect of the smaller cages in UiO-66. These cages have a large heat of adsorption at infinite dilution (Q_{st}^{0}) of ~75 kJ/mol and can only accommodate a single adsorbed xylene molecule. The xylenes adsorbed in these cages are unable to interact with other adsorbates due to the large separation between adjacent cages. Therefore, at low loadings the xylenes exhibit a small guest-guest contribution to the isosteric heat of adsorption (Q_{st}). At higher loadings, the total Q_{st} is reduced by adsorption in the larger cages and the guest-guest contribution becomes more significant, similar to MIL-47 and the other large-pore MOFs examined in our study.

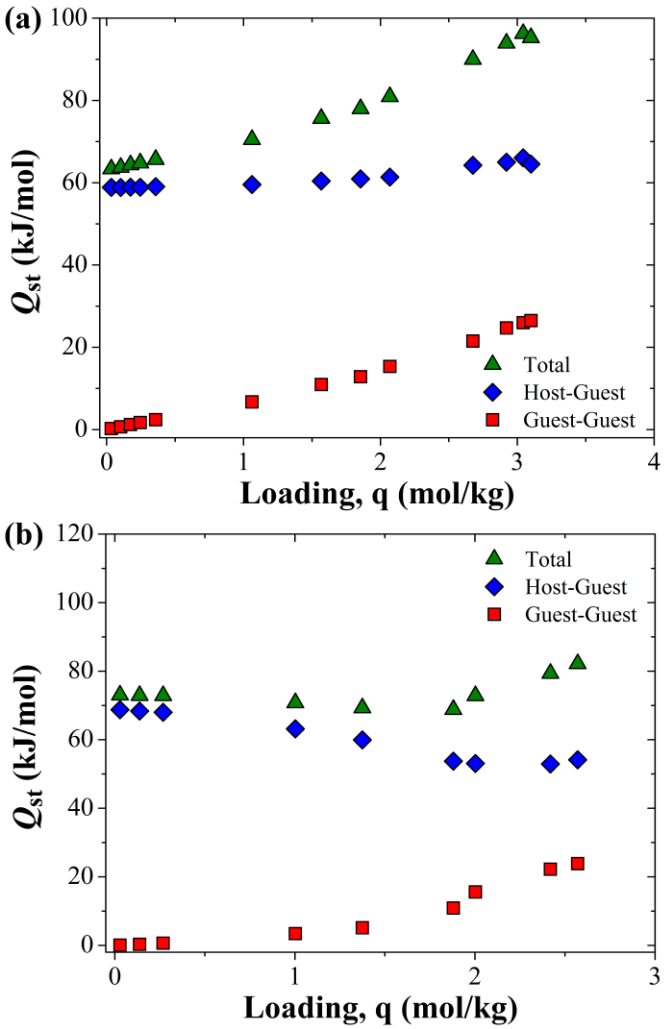

Figure A.2 Comparison of the different contributions to the total heat of adsorption of *o*-xylene calculated using GCMC (D3FF) in (a) MIL-47 at T = 543 K and (b) UiO-66 at T = 423 K.

Note: Q_{st} is defined as:[75]

$$Q_{st} = \mathrm{RT} - \frac{\langle NU \rangle - \langle N \rangle \langle U \rangle}{\langle N^2 \rangle - \langle N \rangle^2} \qquad \text{(A.1)}$$

where N is the number of adsorbates, U is the potential energy, and "<…>" denotes an ensemble average. U can be partitioned into framework-adsorbate and adsorbate-adsorbate contributions. We did not include the "RT" term in the framework-adsorbate and adsorbate-adsorbate contributions to Q_{st} to avoid double-counting this contribution to the total Q_{st}. Therefore, the sum of these two contributions does not equal the total Q_{st} in these plots.

A.4 Additional Comparison of Sim. and Exp. Isotherms

In Chapter 2, we demonstrated that both generic and DFT-based force fields are able to capture the trends in adsorption uptake at a single temperature. It is also important to compare the adsorption uptake as a function of temperature to assess the transferability of the force fields to different operating conditions. In Figure A.3, we demonstrate that both the generic and D3FF are able to accurately capture the experimental data at various temperatures for MIL-47 and DMOF-1.

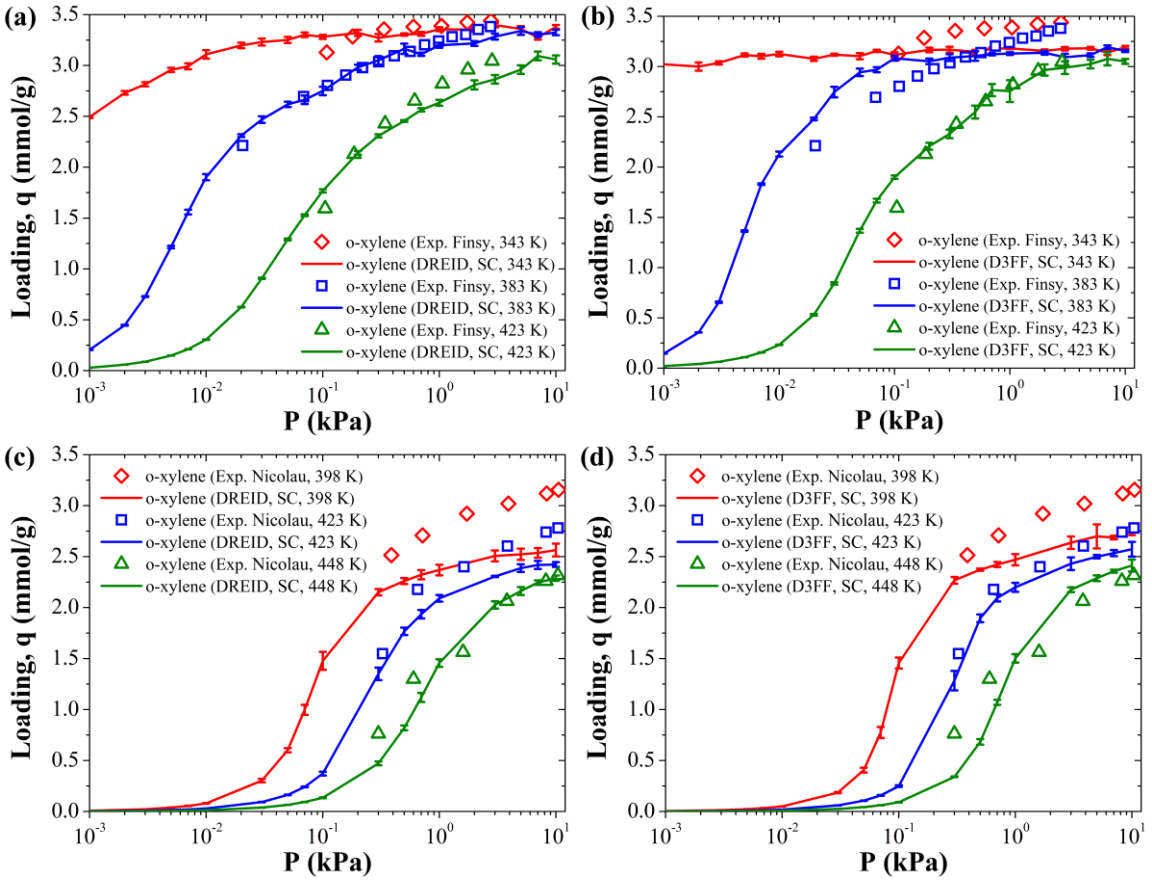

Figure A.3 Comparison of the temperature dependence of simulated and experimental isotherms for xylene isomers using DREIDING and D3FF in MIL-47 (a,b) and DMOF-1 (c,d), respectively. The simulated isotherms are scaled to match the saturation loadings of the experimental isotherms at T = 423 K and T = 448 K in MIL-47 and DMOF-1, respectively, for the purpose of comparison.

Appendix B

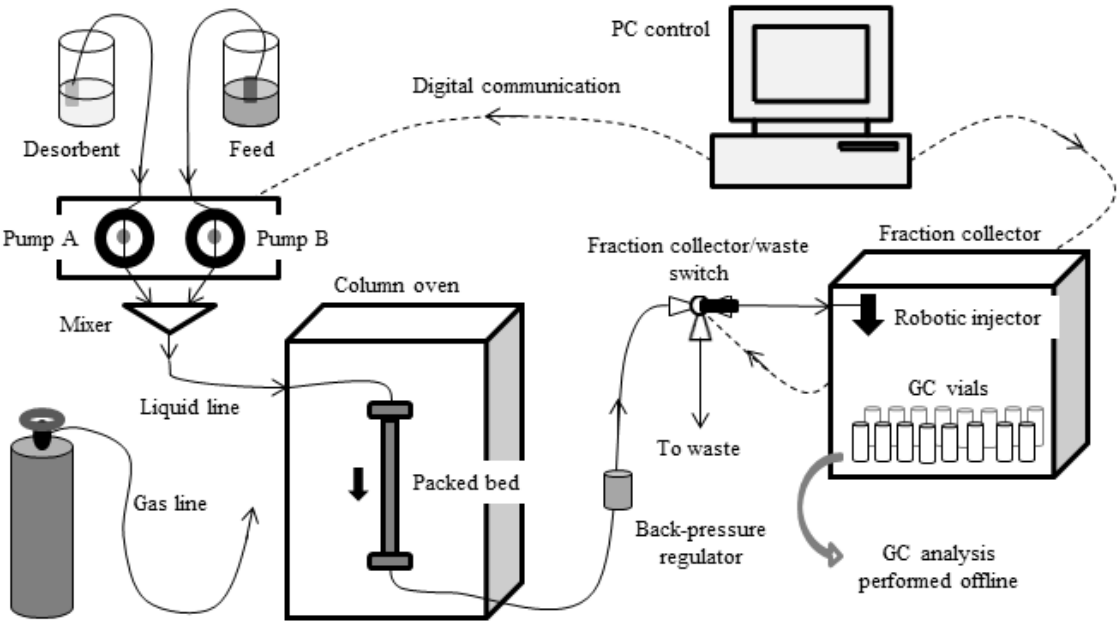

Figure B.1 A schematic of the liquid breakthrough apparatus.

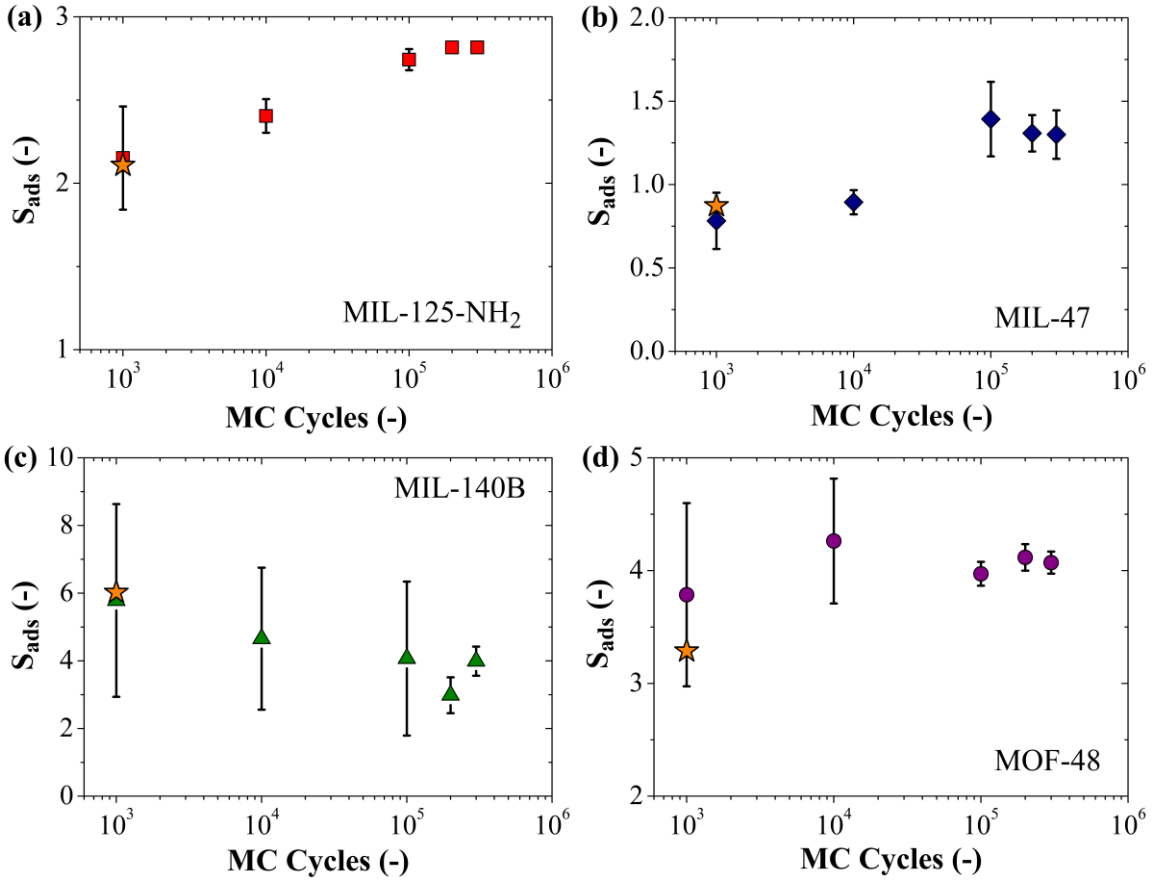

Figure B.2 Comparison of adsorption selectivity for *p*-xylene (S_{ads}) versus number of Monte Carlo (MC) cycles for (a) MIL-125-NH_2, (b) MIL-47, (c) MIL-140B, and (d) MOF-48 at a bulk liquid composition of 0.33:1:2:1 ethylbenzene/*o*-xylene/*m*-xylene/*p*-xylene at T = 50°C and P = 9 bar. The values from the short-cycle MC simulations are shown as orange stars. The error of the long-cycle MC simulations is computed from the standard deviation of 5 separate simulations and represents a 95% confidence interval.

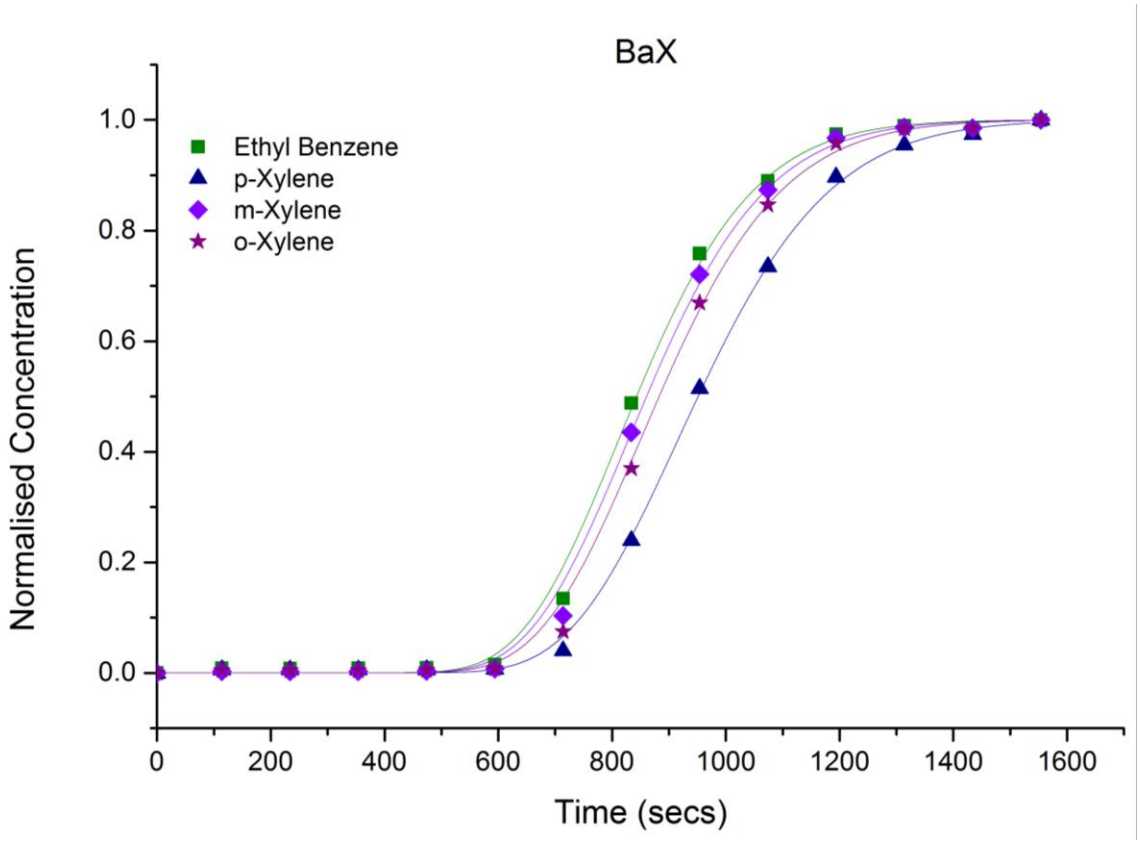

Figure B.3 Experimental (symbols) and model-fitted (solid lines) breakthrough curves for C_8 isomers in BaX zeolite at 180ºC and 9 bar at a bulk liquid composition of 0.33:1:2:1 ethylbenzene/*o*-xylene/*m*-xylene/*p*-xylene and volume flowrate of 0.1 ml/min.

Table B.1 Values of adsorption and dispersion-diffusion parameters obtained from model-based interval fitting of experimental breakthrough curves. All values shown correspond to the 95% confidence interval.

Adsorbent	Adsorption Coefficient $K_i = \partial q_i / \partial c_i$ (mmol/cc)				Dispersion -Diffusion Parameter D (10^{-7} m^2/s)
	EB	*p*X	*m*X	*o*X	
BaX	3.9 ± 0.0	6.6 ± 0.0	4.3 ±0.0	4.9 ±0.0	2.3 ± 0.0
MIL-140B	3.5 ±0.0	5.5 ±0.0	4.5±0.0	4.2 ±0.0	3.6 ±0.0
MIL-125-NH_2	9.3 ±0.0	9.6 ±0.0	8.3 ±0.0	8.1 ± 0.0	4.2 ±0.1
MIL-47	5.7 ± 0.0	13.1 ± 0.0	12.3 ± 0.0	18.8 ± 0.0	1.2 ± 0.0
MOF-48	5.5 ± 0.0	7.05 ± 0.0	4.7 ± 0.0	5.1 ± 0.0	3.9± 0.0

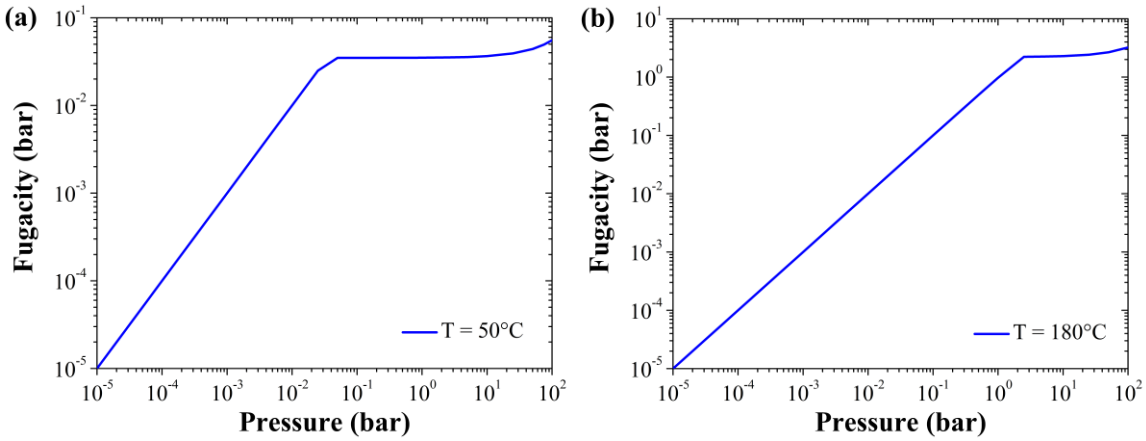

Figure B.4 Comparison of bulk fluid fugacity versus pressure for *o*-xylene at (a) T = 50°C and (b) T = 180°C. The fugacity was calculated at each pressure using the Peng-Robinson equation of state. Similar plots are also observed for the other xylene isomers (data not shown).

Appendix C[8]

Table C.1 Lattice constants for ZIF-8 and ZIF-90 predicted using GAFF and DREIDING force fields.

ZIF	L (Å)		
	Expt.	GAFF	DREIDING
ZIF-8	16.99	16.74 ± 0.03	16.28 ± 0.02
ZIF-90	17.27	16.95 ± 0.02	16.49 ± 0.01

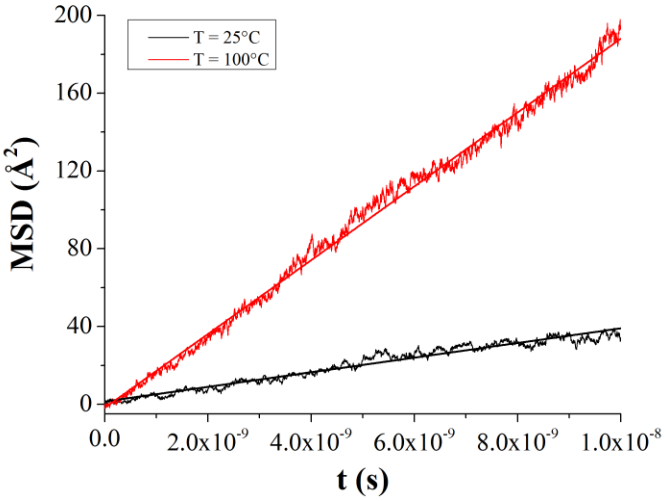

Figure C.1 Average mean square displacement (MSD) versus time plots for methanol in ZIF-90 at T = 25°C and T = 100°C during the MD production period using the GAFF force field including framework flexibility. The adsorbate loading used in these simulations was 14 molecules of CH_3OH /unit cell.

[8] Force field parameters and additional simulation details can be found in the Supporting Information of Gee, J. A.; Chung, J.; Nair, S.; Sholl, D. S. Adsorption and Diffusion of Small Alcohols in Zeolitic Imidazolate Frameworks ZIF-8 and ZIF-90. *The Journal of Physical Chemistry C* **2013**, *117*, 3169-3176.

Table C.2 Diffusion coefficients for methanol in ZIF-90 at T = 25°C and T = 100°C using the GAFF force field including framework flexibility using an MD production period of 10 ns and 50 ns.

	$D_{s,\ CH3OH}$ ($\times 10^{-12}$ m^2/s)	
MD Production Period (ns)	T = 25°C	T = 100°C
10	6.3 ± 2.4	20.83 ± 2.6
50	6.7 ± 0.5	24.16 ± 0.3

Appendix D[9]

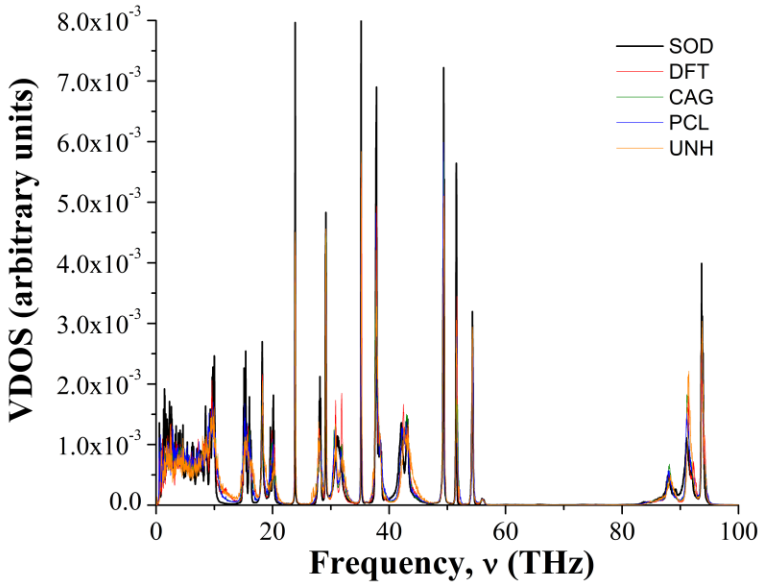

Figure D.1 Vibrational density of states (VDOS) plots for five $Zn(mIm)_2$ polymorphs at T = 25°C.

[9] Additional computational details including force fields, GCMC, and MD simulation parameters, discussion of the harmonic approximation, and GCMC-simulated adsorption isotherms can be found in the Supporting Information of Gee, J. A.; Sholl, D. S. Characterization of the Thermodynamic Stability of Solvated Metal–Organic Framework Polymorphs Using Molecular Simulations. *The Journal of Physical Chemistry C* **2013**, *117*, 20636-20642.

Table D.1 Comparison of the structural parameters for five $Zn(mIm)_2$ energy-minimized polymorphs using the GAFF force field and DFT calculations[183].

Polymorph	Lattice parameter (Å)			Zn-N distance (Å)[b]	Zn-N-Zn angle (θ)[b]
	a	b	c		
SOD (DFT)[a]	14.603	14.603	14.603	1.97	109.48 ± 1.33
SOD (GAFF)	14.596	14.596	14.596	2.01	109.51 ± 0.37
DFT (DFT)[a]	19.111	19.111	17.399	1.99	109.48 ± 5.62
DFT (GAFF)	19.008	19.006	17.407	2.00	109.45 ± 2.83
CAG (DFT)[a]	17.511	17.465	18.129	1.99	109.17 ± 6.48
CAG (GAFF)	17.503	17.457	18.121	2.00	109.53 ± 4.99
PCL (DFT)[a]	13.575	17.918	13.178	1.99	106.18 ± 2.48
PCL (GAFF)	13.558	17.896	13.162	2.00	108.72 ± 7.34
UNH (DFT)[a]	15.697	15.697	9.699	2.02	108.67 ± 10.61
UNH (GAFF)	15.748	15.748	9.730	1.99	109.34 ± 6.59

[a]Note: Lattice parameters for the Density Functional Theory (DFT) data were taken from the crystal structure files of the relaxed polymorph structures provided in the SI of the work of Baburin et al.[183]

[b]The values reported here are the mean and standard deviation calculated over all relevant bond lengths and angles in the unit cell of each structure.

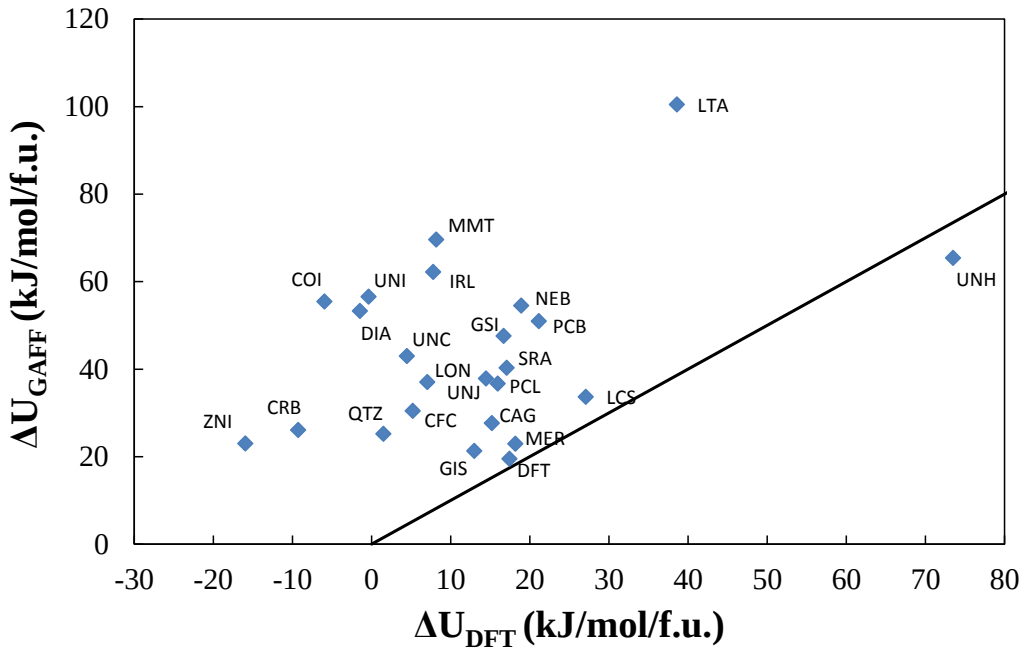

Figure D.2 Comparison of the configurational potential energies for 24 hypothetical polymorphs relative to the $Zn(mIm)_2$ (SOD) structure using the GAFF force field and DFT[183] calculations.

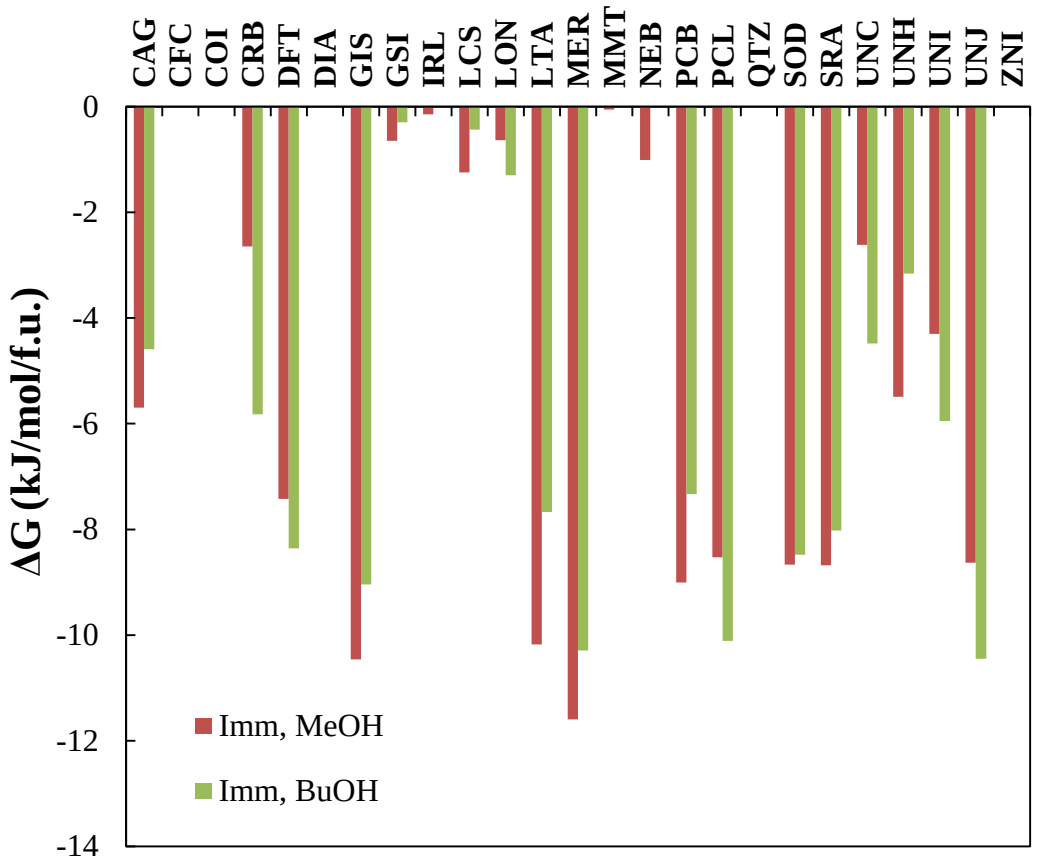

Figure D.3 Free energy of immersion of methanol and butanol in 25 $Zn(mIm)_2$ polymorphs at T = 25°C calculated using GCMC (methanol) and CBMC (butanol)-simulated isotherms using the GAFF force field.

Appendix E[10]

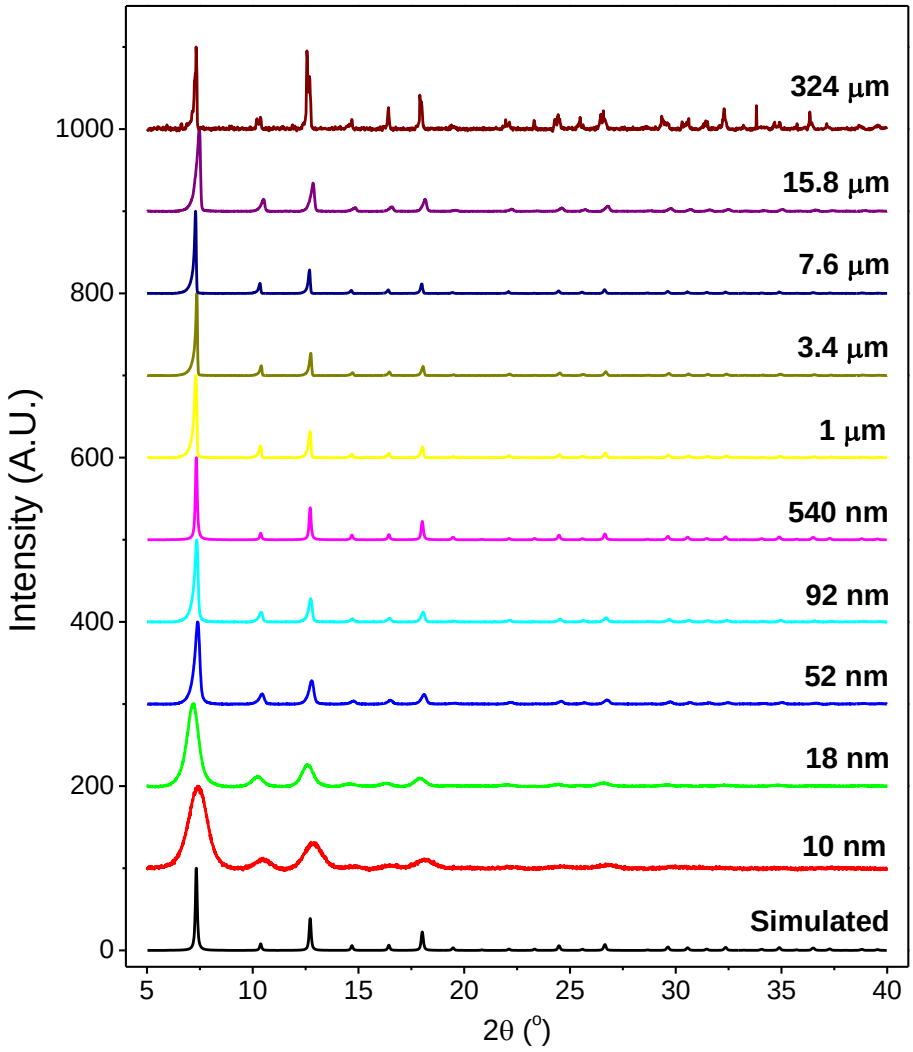

Figure E.1 PXRD patterns of synthesized ZIF-8 samples. The simulated pattern is shown for reference.

[10] Details of force field parameters, OFAST simulations, and synthesis and characterization can be found in the Supporting Information of Gee, J. A.; Zhang, C.; Sholl, D. S.; Lively, R. P. Crystal-Size-Dependent Structural Transitions in Nanoporous Crystals: Adsorption-Induced Transitions in ZIF-8. *The Journal of Physical Chemistry C* **2014**, *118*, 20727-20733.

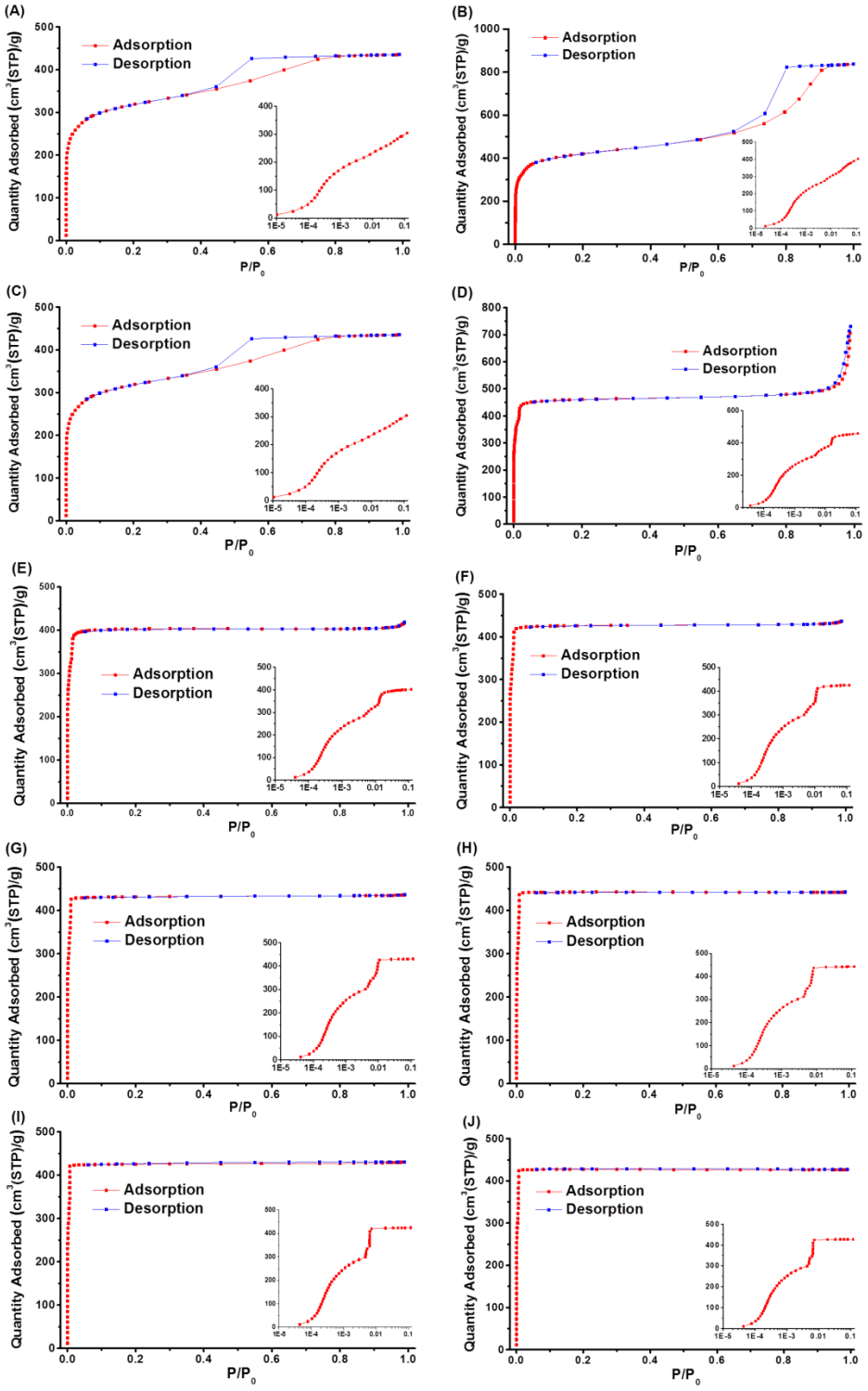

Figure E.2 N_2 physisorption isotherms (77K) of synthesized ZIF-8 samples (A) 10 nm (B) 18 nm (C) 52 nm (D) 92 nm (E) 540 nm (F) 1 micron (G) 3.4 micron (H) 7.6 micron (I) 15.8 micron (J) 324 micron.

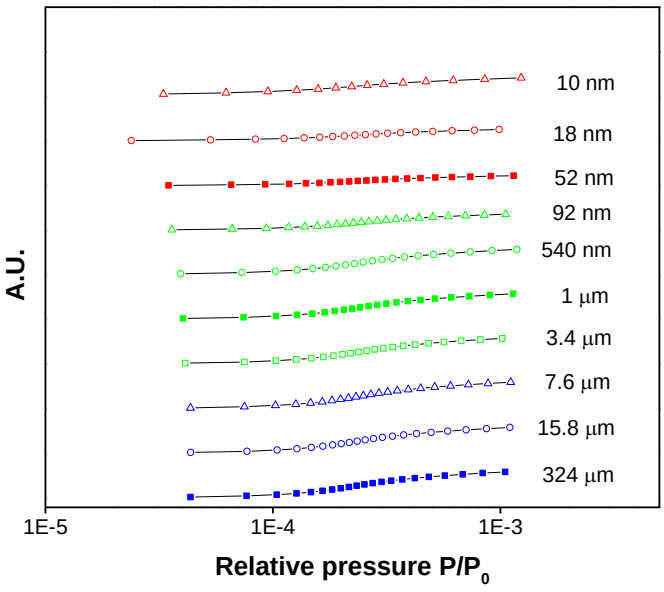

Figure E.3 Magnification at the low relative pressure region ($P/P0<10^{-3}$) of N_2 adsorption isotherms.

Table E.1 Surface area and micropore volume of synthesized ZIF-8 samples. Values of the commercial sample are shown as well for reference.

ZIF-8 sample	BET surface area (m^2/g)	t-plot micropore volume (cm^3/g)	Range of relative pressure (P/P_0) for BET analysis
10 nm	1172	0.290	0.0004-0.07
18 nm	1247	0.399	0.0004-0.005
52 nm	1374	0.582	0.0004-0.004
92 nm	1475	0.661	0.0004-0.005
540 nm	1303	0.603	0.0004-0.004
1 μm	1377	0.645	0.0004-0.005
3.4 μm	1390	0.658	0.0004-0.004
7.6 μm	1436	0.681	0.0004-0.004
15.8 μm	1364	0.650	0.0004-0.005
324 μm	1377	0.659	0.0004-0.004
Commercial sample	1327	0.625	0.0004-0.004

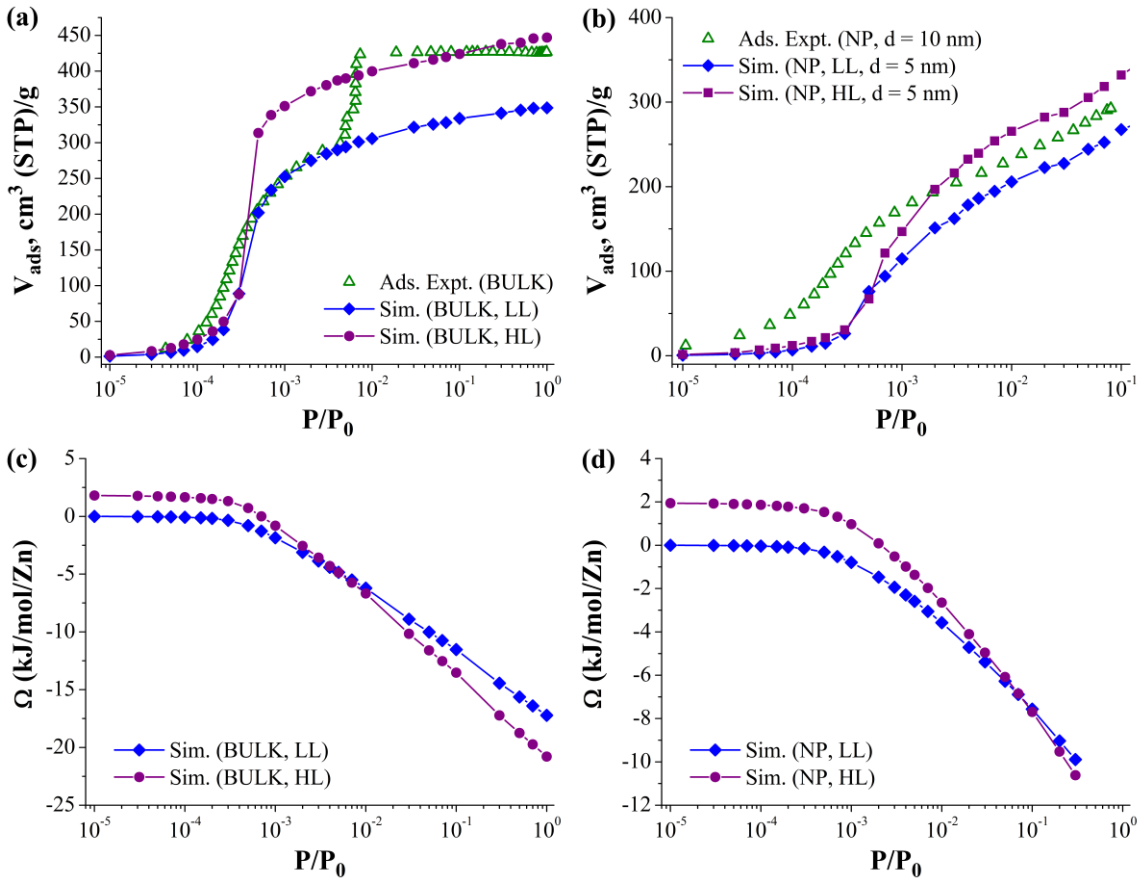

Figure E.4 Adsorption isotherms (a, b) and Ω (c, d) as a function of P/P_0 for N_2 in ZIF-8 high loading (HL) and low loading (LL) forms for the bulk ZIF-8 structure at T = 77 K.

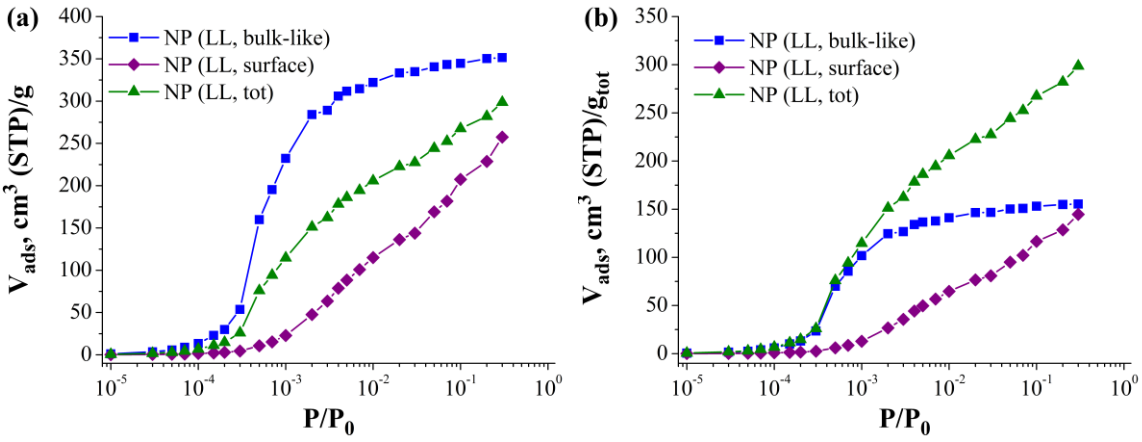

Figure E.5 Adsorption isotherms as a function of P/P_0 for N_2 in the ZIF-8 nanoparticle at T = 77 K. The adsorption uptake is normalized per framework mass in each region (a) and total framework mass (b).

Table E.2 Transition pressure (P/P_0) observed in different regions of the nanoparticle calculated using the OFAST method.

	Transition Pressure, P/P_0		
Normalization	**NP (bulk-like)**	**NP (surface)**	**Total**
Region	0.005	0.05	0.03
Total	0.05	0.20	0.12

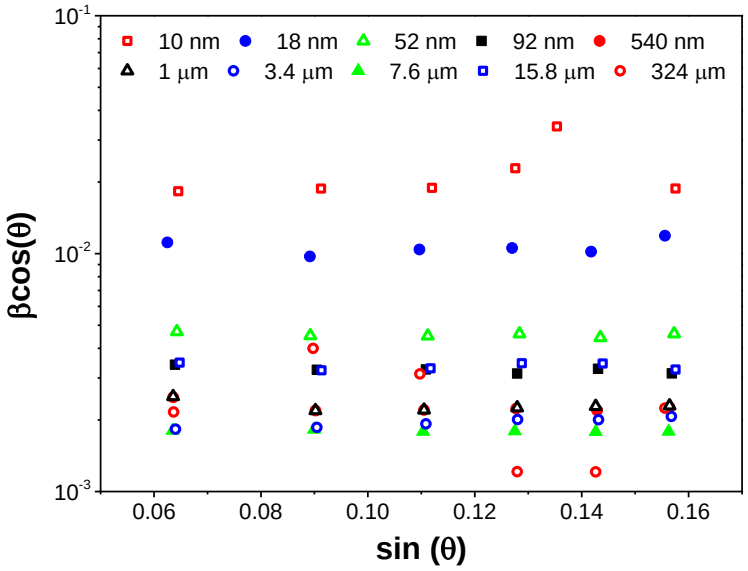

Figure E.6 Williamson-Hall plots of ZIF-8 samples.

REFERENCES

(1) Murray, L. J.; Dincă, M.; Long, J. R. Hydrogen storage in metal–organic frameworks. *Chemical Society Reviews* **2009**, *38*, 1294-1314.

(2) Millward, A. R.; Yaghi, O. M. Metal-organic frameworks with exceptionally high capacity for storage of carbon dioxide at room temperature. *Journal of the American Chemical Society* **2005**, *127*, 17998-17999.

(3) Czaja, A. U.; Trukhan, N.; Muller, U. Industrial applications of metal-organic frameworks. *Chemical Society Reviews* **2009**, *38*, 1284-1293.

(4) Keskin, S.; van Heest, T. M.; Sholl, D. S. Can Metal–Organic Framework Materials Play a Useful Role in Large-Scale Carbon Dioxide Separations? *ChemSusChem* **2010**, *3*, 879-891.

(5) Horcajada, P.; Chalati, T.; Serre, C.; Gillet, B.; Sebrie, C.; Baati, T.; Eubank, J. F.; Heurtaux, D.; Clayette, P.; Kreuz, C. Porous metal-organic-framework nanoscale carriers as a potential platform for drug delivery and imaging. *Nature materials* **2009**, *9*, 172-178.

(6) Lee, J. Y.; Farha, O. K.; Roberts, J.; Scheidt, K. A.; Nguyen, S. B. T.; Hupp, J. T. Metal–organic framework materials as catalysts. *Chemical Society Reviews* **2009**, *38*, 1450-1459.

(7) Meek, S. T.; Greathouse, J. A.; Allendorf, M. D. Metal-Organic Frameworks: A Rapidly Growing Class of Versatile Nanoporous Materials. *Advanced Materials* **2011**, *23*, 249-267.

(8) Allendorf, M.; Bauer, C.; Bhakta, R.; Houk, R. Luminescent metal–organic frameworks. *Chemical Society Reviews* **2009**, *38*, 1330-1352.

(9) Haldoupis, E.; Nair, S.; Sholl, D. S. Efficient Calculation of Diffusion Limitations in Metal Organic Framework Materials: A Tool for Identifying Materials for Kinetic Separations. *Journal of the American Chemical Society* **2010**, *132*, 7528-7539.

(10) First, E. L.; Floudas, C. A. MOFomics: Computational pore characterization of metal–organic frameworks. *Microporous and Mesoporous Materials* **2012**, *165*, 32-39.

(11) Wilmer, C. E.; Leaf, M.; Lee, C. Y.; Farha, O. K.; Hauser, B. G.; Hupp, J. T.; Snurr, R. Q. Large-scale screening of hypothetical metal–organic frameworks. *Nat Chem* **2012**, *4*, 83-89.

(12) Lin, L.-C.; Berger, A. H.; Martin, R. L.; Kim, J.; Swisher, J. A.; Jariwala, K.; Rycroft, C. H.; Bhown, A. S.; Deem, M. W.; Haranczyk, M., et al. In silico screening of carbon-capture materials. *Nat Mater* **2012**, *11*, 633-641.

(13) Krishna, R.; van Baten, J. M. In silico screening of metal–organic frameworks in separation applications. *Physical Chemistry Chemical Physics* **2011**, *13*, 10593-10616.

(14) Alaerts, L.; Kirschhock, C. E. A.; Maes, M.; van der Veen, M. A.; Finsy, V.; Depla, A.; Martens, J. A.; Baron, G. V.; Jacobs, P. A.; Denayer, J. F. M., et al. Selective Adsorption and Separation of Xylene Isomers and Ethylbenzene with the Microporous Vanadium(IV) Terephthalate MIL-47. *Angewandte Chemie International Edition* **2007**, *46*, 4293-4297.

(15) Castillo, J. M.; Vlugt, T. J. H.; Calero, S. Molecular Simulation Study on the Separation of Xylene Isomers in MIL-47 Metal−Organic Frameworks. *The Journal of Physical Chemistry C* **2009**, *113*, 20869-20874.

(16) Vermoortele, F.; Maes, M.; Moghadam, P. Z.; Lennox, M. J.; Ragon, F.; Boulhout, M.; Biswas, S.; Laurier, K. G. M.; Beurroies, I.; Denoyel, R., et al. p-Xylene-Selective Metal–Organic Frameworks: A Case of Topology-Directed Selectivity. *Journal of the American Chemical Society* **2011**, *133*, 18526-18529.

(17) Torres-Knoop, A.; Krishna, R.; Dubbeldam, D. Separating Xylene Isomers by Commensurate Stacking of p-Xylene within Channels of MAF-X8. *Angewandte Chemie* **2014**, *126*, 7908-7912.

(18) Frenkel, D.; Smit, B. *Understanding molecular simulation: from algorithms to applications*; Academic press, 2001; Vol. 1.

(19) Keskin, S.; Liu, J.; Rankin, R. B.; Johnson, J. K.; Sholl, D. S. Progress, Opportunities, and Challenges for Applying Atomically Detailed Modeling to Molecular Adsorption and Transport in Metal−Organic Framework Materials. *Industrial & Engineering Chemistry Research* **2008**, *48*, 2355-2371.

(20) Babarao, R.; Hu, Z.; Jiang, J.; Chempath, S.; Sandler, S. I. Storage and Separation of CO2 and CH4 in Silicalite, C168 Schwarzite, and IRMOF-1: A Comparative Study from Monte Carlo Simulation. *Langmuir* **2006**, *23*, 659-666.

(21) Dubbeldam, D.; Calero, S.; Vlugt, T. J. H.; Krishna, R.; Maesen, T. L. M.; Smit, B. United Atom Force Field for Alkanes in Nanoporous Materials. *The Journal of Physical Chemistry B* **2004**, *108*, 12301-12313.

(22) Siepmann, J. I.; Frenkel, D. Configurational bias Monte Carlo: a new sampling scheme for flexible chains. *Molecular Physics* **1992**, *75*, 59-70.

(23) Jiang, J.; Sandler, S. I. Monte Carlo Simulation for the Adsorption and Separation of Linear and Branched Alkanes in IRMOF-1. *Langmuir* **2006**, *22*, 5702-5707.

(24) Düren, T.; Snurr, R. Q. Assessment of Isoreticular Metal−Organic Frameworks for Adsorption Separations: A Molecular Simulation Study of Methane/n-Butane Mixtures. *The Journal of Physical Chemistry B* **2004**, *108*, 15703-15708.

(25) Pérez-Pellitero, J.; Amrouche, H.; Siperstein, F. R.; Pirngruber, G.; Nieto-Draghi, C.; Chaplais, G.; Simon-Masseron, A.; Bazer-Bachi, D.; Peralta, D.; Bats, N. Adsorption of CO2, CH4, and N2 on Zeolitic Imidazolate Frameworks: Experiments and Simulations. *Chemistry – A European Journal* **2010**, *16*, 1560-1571.

(26) Fang, H.; Kamakoti, P.; Zang, J.; Cundy, S.; Paur, C.; Ravikovitch, P. I.; Sholl, D. S. Prediction of CO2 Adsorption Properties in Zeolites Using Force Fields Derived from Periodic Dispersion-Corrected DFT Calculations. *The Journal of Physical Chemistry C* **2012**, *116*, 10692-10701.

(27) McDaniel, J. G.; Schmidt, J. R. Robust, Transferable, and Physically Motivated Force Fields for Gas Adsorption in Functionalized Zeolitic Imidazolate Frameworks. *The Journal of Physical Chemistry C* **2012**, *116*, 14031-14039.

(28) Skoulidas, A. I. Molecular Dynamics Simulations of Gas Diffusion in Metal−Organic Frameworks: Argon in CuBTC. *Journal of the American Chemical Society* **2004**, *126*, 1356-1357.

(29) Skoulidas, A. I.; Sholl, D. S. Self-Diffusion and Transport Diffusion of Light Gases in Metal-Organic Framework Materials Assessed Using Molecular Dynamics Simulations. *The Journal of Physical Chemistry B* **2005**, *109*, 15760-15768.

(30) Sarkisov, L.; Düren, T.; Snurr, R. Q. Molecular modelling of adsorption in novel nanoporous metal–organic materials. *Molecular Physics* **2004**, *102*, 211-221.

(31) Ford, D. C.; Dubbeldam, D.; Snurr, R. Q.; Künzel, V.; Wehring, M.; Stallmach, F.; Kärger, J.; Müller, U. Self-Diffusion of Chain Molecules in the Metal–Organic Framework IRMOF-1: Simulation and Experiment. *The Journal of Physical Chemistry Letters* **2012**, *3*, 930-933.

(32) Wehring, M.; Gascon, J.; Dubbeldam, D.; Kapteijn, F.; Snurr, R. Q.; Stallmach, F. Self-Diffusion Studies in CuBTC by PFG NMR and MD Simulations. *The Journal of Physical Chemistry C* **2010**, *114*, 10527-10534.

(33) Battisti, A.; Taioli, S.; Garberoglio, G. Zeolitic imidazolate frameworks for separation of binary mixtures of CO2, CH4, N2 and H2: A computer simulation investigation. *Microporous and Mesoporous Materials* **2011**, *143*, 46-53.

(34) Hertäg, L.; Bux, H.; Caro, J.; Chmelik, C.; Remsungnen, T.; Knauth, M.; Fritzsche, S. Diffusion of CH4 and H2 in ZIF-8. *Journal of Membrane Science* **2011**, *377*, 36-41.

(35) Pantatosaki, E.; Megariotis, G.; Pusch, A.-K.; Chmelik, C.; Stallmach, F.; Papadopoulos, G. K. On the Impact of Sorbent Mobility on the Sorbed Phase Equilibria and Dynamics: A Study of Methane and Carbon Dioxide within the Zeolite Imidazolate Framework-8. *The Journal of Physical Chemistry C* **2011**, *116*, 201-207.

(36) Zheng, B.; Sant, M.; Demontis, P.; Suffritti, G. B. Force Field for Molecular Dynamics Computations in Flexible ZIF-8 Framework. *The Journal of Physical Chemistry C* **2011**, *116*, 933-938.

(37) Hu, Z.; Zhang, L.; Jiang, J. Development of a force field for zeolitic imidazolate framework-8 with structural flexibility. *J Chem Phys* **2012**, *136*, 244703-244707.

(38) Dubbeldam, D.; Krishna, R.; Calero, S.; Yazaydın, A. Ö. Computer-Assisted Screening of Ordered Crystalline Nanoporous Adsorbents for Separation of Alkane Isomers. *Angewandte Chemie* **2012**, *124*, 12037-12041.

(39) Scheirs, J.; Long, T. E.; Wiley, J. *Modern polyesters: chemistry and technology of polyesters and copolyesters*; John Wiley & Sons Ltd.: Chichester, UK, 2003.

(40) Meyers, R. A. *Handbook of petroleum refining processes*; McGraw-Hill New York, 2004; Vol. 3.

(41) Ruthven, D. M.; Goddard, M. Sorption and diffusion of C8 aromatic hydrocarbons in faujasite type zeolites. I. Equilibrium isotherms and separation factors. *Zeolites* **1986**, *6*, 275-282.

(42) Hammond, P. D.; McArdle, E. H. Solvent Properties of C8Aromatic Hydrocarbons. *Industrial & Engineering Chemistry* **1943**, *35*, 809-810.

(43) Gomes, P. S.; Minceva, M.; Rodrigues, A. E. Simulated moving bed technology: old and new. *Adsorption* **2006**, *12*, 375-392.

(44) Moïse, J.-C.; Bellat, J.-P. Effect of Preadsorbed Water on the Adsorption of p-xylene and m-xylene Mixtures on BaX and BaY Zeolites. *The Journal of Physical Chemistry B* **2005**, *109*, 17239-17244.

(45) Finsy, V.; Verelst, H.; Alaerts, L.; De Vos, D.; Jacobs, P. A.; Baron, G. V.; Denayer, J. F. M. Pore-Filling-Dependent Selectivity Effects in the Vapor-Phase Separation of Xylene Isomers on the Metal−Organic Framework MIL-47. *Journal of the American Chemical Society* **2008**, *130*, 7110-7118.

(46) Bárcia, P. S.; Guimarães, D.; Mendes, P. A. P.; Silva, J. A. C.; Guillerm, V.; Chevreau, H.; Serre, C.; Rodrigues, A. E. Reverse shape selectivity in the adsorption of

hexane and xylene isomers in MOF UiO-66. *Microporous and Mesoporous Materials* **2011**, *139*, 67-73.

(47) Chang, N.; Yan, X.-P. Exploring reverse shape selectivity and molecular sieving effect of metal-organic framework UIO-66 coated capillary column for gas chromatographic separation. *Journal of Chromatography A* **2012**, *1257*, 116-124.

(48) Peralta, D.; Barthelet, K.; Pérez-Pellitero, J.; Chizallet, C.; Chaplais, G.; Simon-Masseron, A.; Pirngruber, G. D. Adsorption and Separation of Xylene Isomers: CPO-27-Ni vs HKUST-1 vs NaY. *The Journal of Physical Chemistry C* **2012**, *116*, 21844-21855.

(49) Nicolau, M. P.; Bárcia, P. S.; Gallegos, J. M.; Silva, J. A.; Rodrigues, A. E.; Chen, B. Single-and multicomponent vapor-phase adsorption of xylene isomers and ethylbenzene in a microporous metal− organic framework. *The Journal of Physical Chemistry C* **2009**, *113*, 13173-13179.

(50) Gu, Z.-Y.; Jiang, D.-Q.; Wang, H.-F.; Cui, X.-Y.; Yan, X.-P. Adsorption and separation of xylene isomers and ethylbenzene on two Zn− terephthalate metal− organic frameworks. *The Journal of Physical Chemistry C* **2009**, *114*, 311-316.

(51) Vermoortele, F.; Maes, M.; Moghadam, P. Z.; Lennox, M. J.; Ragon, F.; Boulhout, M.; Biswas, S.; Laurier, K. G.; Beurroies, I.; Denoyel, R. p-xylene-selective metal–organic frameworks: a case of topology-directed selectivity. *Journal of the American Chemical Society* **2011**, *133*, 18526-18529.

(52) Mayo, S. L.; Olafson, B. D.; Goddard, W. A. DREIDING: a generic force field for molecular simulations. *The Journal of Physical Chemistry* **1990**, *94*, 8897-8909.

(53) Granato, M. A.; Martins, V. D.; Ferreira, A. F. P.; Rodrigues, A. E. Adsorption of xylene isomers in MOF UiO-66 by molecular simulation. *Microporous and Mesoporous Materials* **2014**, *190*, 165-170.

(54) Lahoz-Martín, F. D.; Martín-Calvo, A.; Calero, S. Selective Separation of BTEX Mixtures Using Metal–Organic Frameworks. *The Journal of Physical Chemistry C* **2014**, *118*, 13126-13136.

(55) Fang, H.; Demir, H.; Kamakoti, P.; Sholl, D. S. Recent developments in first-principles force fields for molecules in nanoporous materials. *Journal of Materials Chemistry A* **2014**, *2*, 274-291.

(56) Han, S. S.; Deng, W.-Q.; Goddard, W. A. Improved Designs of Metal–Organic Frameworks for Hydrogen Storage. *Angewandte Chemie International Edition* **2007**, *46*, 6289-6292.

(57) Zang, J.; Nair, S.; Sholl, D. S. Prediction of Water Adsorption in Copper-Based Metal–Organic Frameworks Using Force Fields Derived from Dispersion-Corrected DFT Calculations. *The Journal of Physical Chemistry C* **2013**, *117*, 7519-7525.

(58) Dzubak, A. L.; Lin, L.-C.; Kim, J.; Swisher, J. A.; Poloni, R.; Maximoff, S. N.; Smit, B.; Gagliardi, L. Ab initio carbon capture in open-site metal–organic frameworks. *Nat Chem* **2012**, *4*, 810-816.

(59) Chen, L.; Morrison, C. A.; Düren, T. Improving Predictions of Gas Adsorption in Metal–Organic Frameworks with Coordinatively Unsaturated Metal Sites: Model Potentials, ab initio Parameterization, and GCMC Simulations. *The Journal of Physical Chemistry C* **2012**, *116*, 18899-18909.

(60) Fu, J.; Sun, H. An Ab Initio Force Field for Predicting Hydrogen Storage in IRMOF Materials. *The Journal of Physical Chemistry C* **2009**, *113*, 21815-21824.

(61) Fang, H.; Kamakoti, P.; Ravikovitch, P. I.; Aronson, M.; Paur, C.; Sholl, D. S. First principles derived, transferable force fields for CO2 adsorption in Na-exchanged cationic zeolites. *Physical Chemistry Chemical Physics* **2013**, *15*, 12882-12894.

(62) Snurr, R. Q.; Bell, A. T.; Theodorou, D. N. Prediction of adsorption of aromatic hydrocarbons in silicalite from grand canonical Monte Carlo simulations with biased insertions. *The Journal of Physical Chemistry* **1993**, *97*, 13742-13752.

(63) Jorgensen, W. L.; Laird, E. R.; Nguyen, T. B.; Tirado-Rives, J. Monte Carlo simulations of pure liquid substituted benzenes with OPLS potential functions. *Journal of Computational Chemistry* **1993**, *14*, 206-215.

(64) Rappe, A. K.; Casewit, C. J.; Colwell, K. S.; Goddard, W. A.; Skiff, W. M. UFF, a full periodic table force field for molecular mechanics and molecular dynamics simulations. *Journal of the American Chemical Society* **1992**, *114*, 10024-10035.

(65) Manz, T. A.; Sholl, D. S. Chemically Meaningful Atomic Charges That Reproduce the Electrostatic Potential in Periodic and Nonperiodic Materials. *Journal of Chemical Theory and Computation* **2010**, *6*, 2455-2468.

(66) Manz, T. A.; Sholl, D. S. Improved Atoms-in-Molecule Charge Partitioning Functional for Simultaneously Reproducing the Electrostatic Potential and Chemical States in Periodic and Nonperiodic Materials. *Journal of Chemical Theory and Computation* **2012**, *8*, 2844-2867.

(67) Watanabe, T.; Manz, T. A.; Sholl, D. S. Accurate Treatment of Electrostatics during Molecular Adsorption in Nanoporous Crystals without Assigning Point Charges to Framework Atoms. *The Journal of Physical Chemistry C* **2011**, *115*, 4824-4836.

(68) Kresse, G.; Furthmüller, J. Efficient iterative schemes for *ab initio* total-energy calculations using a plane-wave basis set. *Physical Review B* **1996**, *54*, 11169-11186.

(69) Sholl, D.; Steckel, J. A. *Density functional theory: a practical introduction*; John Wiley & Sons, 2011.

(70) Grimme, S.; Antony, J.; Ehrlich, S.; Krieg, H. A consistent and accurate ab initio parametrization of density functional dispersion correction (DFT-D) for the 94 elements H-Pu. *The Journal of Chemical Physics* **2010**, *132*, -.

(71) Grimme, S.; Ehrlich, S.; Goerigk, L. Effect of the damping function in dispersion corrected density functional theory. *Journal of Computational Chemistry* **2011**, *32*, 1456-1465.

(72) Grimme, S.; Antony, J.; Schwabe, T.; Muck-Lichtenfeld, C. Density functional theory with dispersion corrections for supramolecular structures, aggregates, and complexes of (bio)organic molecules. *Organic & Biomolecular Chemistry* **2007**, *5*, 741-758.

(73) Ghysels, A.; Vandichel, M.; Verstraelen, T.; van der Veen, M.; De Vos, D.; Waroquier, M.; Van Speybroeck, V. Host–guest and guest–guest interactions between xylene isomers confined in the MIL-47(V) pore system. *Theoretical Chemistry Accounts* **2012**, *131*, 1-13.

(74) Widom, B. Some topics in the theory of fluids. *The Journal of Chemical Physics* **1963**, *39*, 2808-2812.

(75) Karavias, F.; Myers, A. L. Isosteric heats of multicomponent adsorption: thermodynamics and computer simulations. *Langmuir* **1991**, *7*, 3118-3126.

(76) Marcus, Y. *The properties of solvents*; Wiley Chichester, 1998.

(77) Wong-Foy, A. G.; Matzger, A. J.; Yaghi, O. M. Exceptional H2 Saturation Uptake in Microporous Metal−Organic Frameworks. *Journal of the American Chemical Society* **2006**, *128*, 3494-3495.

(78) Barthelet, K.; Marrot, J.; Riou, D.; Férey, G. A Breathing Hybrid Organic–Inorganic Solid with Very Large Pores and High Magnetic Characteristics. *Angewandte Chemie* **2002**, *114*, 291-294.

(79) Wang, X.; Liu, L.; Jacobson, A. J. Intercalation of Organic Molecules into Vanadium(IV) Benzenedicarboxylate: Adsorbate Structure and Selective Absorption of Organosulfur Compounds. *Angewandte Chemie* **2006**, *118*, 6649-6653.

(80) Wang, X.; Eckert, J.; Liu, L.; Jacobson, A. J. Breathing and Twisting: An Investigation of Framework Deformation and Guest Packing in Single Crystals of a Microporous Vanadium Benzenedicarboxylate. *Inorganic Chemistry* **2011**, *50*, 2028-2036.

(81) *Sorbex: Industrial-scale adsorptive separation, Advances in Separation Processes*; Johnson, J. A.; Kabza, R. G., Eds.; Taylor & Francis, 1990.

(82) Peralta, D.; Barthelet, K.; Perez-Pellitero, J.; Chizallet, C.; Chaplais, G.; Simon-Masseron, A.; Pirngruber, G. D. Adsorption and Separation of Xylene Isomers: CPO-27-Ni vs HKUST-1 vs NaY. *Journal of Physical Chemistry C* **2012**, *116*, 21844-21855.

(83) Eddaoudi, M.; Moler, D. B.; Li, H. L.; Chen, B. L.; Reineke, T. M.; O'Keeffe, M.; Yaghi, O. M. Modular chemistry: Secondary building units as a basis for the design of

highly porous and robust metal-organic carboxylate frameworks. *Accounts of Chemical Research* **2001**, *34*, 319-330.

(84) Li, H.; Eddaoudi, M.; O'Keeffe, M.; Yaghi, O. M. Design and synthesis of an exceptionally stable and highly porous metal-organic framework. *Nature* **1999**, *402*, 276-279.

(85) Ferey, G. Hybrid porous solids: past, present, future. *Chemical Society Reviews* **2008**, *37*, 191-214.

(86) Li, J.-R.; Kuppler, R. J.; Zhou, H.-C. Selective gas adsorption and separation in metal-organic frameworks. *Chemical Society Reviews* **2009**, *38*, 1477-1504.

(87) Li, J.-R. S., Julian; Zhou, Hong-Cai Metal-Organic Frameworks for Separations. *Chemical Reviews* **2012**, *112*, 869-932.

(88) He, Y.; Zhou, W.; Krishna, R.; Chen, B. Microporous metal-organic frameworks for storage and separation of small hydrocarbons. *Chemical Communications* **2012**, *48*, 11813-11831.

(89) Herm, Z. R.; Bloch, E. D.; Long, J. R. Hydrocarbon Separations in Metal–Organic Frameworks. *Chemistry of Materials* **2013**, *26*, 323-338.

(90) Chung, Y. G.; Camp, J.; Haranczyk, M.; Sikora, B. J.; Bury, W.; Krungleviciute, V.; Yildirim, T.; Farha, O. K.; Sholl, D. S.; Snurr, R. Q. Computation-Ready, Experimental (CoRE) Metal-Organic Frameworks: A Tool to Enable High-Throughput Screening of Nanoporous Crystals. *Chemistry of Materials* **2014**.

(91) Dubbeldam, D.; Calero, S.; Ellis, D.; Snurr, R. RASPA 1.0. *Northwestern University* **2013**.

(92) Minceva, M.; Rodrigues, A. E. Understanding and revamping of industrial scale SMB units for p-xylene separation. *AIChE Journal* **2007**, *53*, 138-149.

(93) Wick, C. D.; Martin, M. G.; Siepmann, J. I. Transferable Potentials for Phase Equilibria. 4. United-Atom Description of Linear and Branched Alkenes and Alkylbenzenes. *The Journal of Physical Chemistry B* **2000**, *104*, 8008-8016.

(94) Barthelet, K.; Marrot, J.; Riou, D.; Ferey, G. A breathing hybrid organic-inorganic solid with very large pores and high magnetic characteristics. *Angewandte Chemie-International Edition* **2002**, *41*, 281-+.

(95) Guillerm, V.; Ragon, F.; Dan-Hardi, M.; Devic, T.; Vishnuvarthan, M.; Campo, B.; Vimont, A.; Clet, G.; Yang, Q.; Maurin, G., et al. A Series of Isoreticular, Highly Stable, Porous Zirconium Oxide Based Metal-Organic Frameworks. *Angewandte Chemie-International Edition* **2012**, *51*, 9267-9271.

(96) Phan, A.; Czaja, A. U.; Gandara, F.; Knobler, C. B.; Yaghi, O. M. Metal-Organic Frameworks of Vanadium as Catalysts for Conversion of Methane to Acetic Acid. *Inorganic Chemistry* **2011**, *50*, 7388-7390.

(97) Kim, S. N.; Kim, J.; Kim, H. Y.; Cho, H. Y.; Ahn, W. S. Adsorption/catalytic properties of MIL-125 and NH2-MIL-125. *Catalysis Today* **2013**, *204*, 85-93.

(98) Alaerts, L.; Maes, M.; Jacobs, P. A.; Denayer, J. F. M.; De Vos, D. E. Activation of the metal-organic framework MIL-47 for selective adsorption of xylenes and other difunctionalized aromatics. *Physical Chemistry Chemical Physics* **2008**, *10*, 2979-2985.

(99) Moreira, M. A.; Santos, J. C.; Ferreira, A. F. P.; Loureiro, J. M.; Ragon, F.; Horcajada, P.; Yot, P. G.; Serre, C.; Rodrigues, A. E. Effect of ethylbenzene in p-xylene

selectivity of the porous titanium amino terephthalate MIL-125(Ti)_NH2. *Microporous and Mesoporous Materials* **2012**, *158*, 229-234.

(100) Chen, D.-L.; Shang, H.; Zhu, W.; Krishna, R. Transient breakthroughs of CO2/CH4 and C3H6/C3H8 mixtures in fixed beds packed with Ni-MOF-74. *Chemical Engineering Science* **2014**, *117*, 407-415.

(101) Krishna, R.; van Baten, J. M. A comparison of the CO2 capture characteristics of zeolites and metal-organic frameworks. *Separation and Purification Technology* **2012**, *87*, 120-126.

(102) Silva, M. S. P.; Mota, J. P. B.; Rodrigues, A. E. Adsorption Equilibrium and Kinetics of the Parex' Feed and Desorbent Streams from Batch Experiments. *Chemical Engineering & Technology* **2014**, *37*, 1541-1551.

(103) Finsy, V.; Verelst, H.; Alaerts, L.; De Vos, D.; Jacobs, P. A.; Baron, G. V.; Denayer, J. F. M. Pore-filling-dependent selectivity effects in the vapor-phase separation of xylene isomers on the metal-organic framework MIL-47. *Journal of the American Chemical Society* **2008**, *130*, 7110-7118.

(104) Düren, T.; Millange, F.; Férey, G.; Walton, K. S.; Snurr, R. Q. Calculating Geometric Surface Areas as a Characterization Tool for Metal−Organic Frameworks. *The Journal of Physical Chemistry C* **2007**, *111*, 15350-15356.

(105) Myers, A. L.; Monson, P. A. Adsorption in Porous Materials at High Pressure: Theory and Experiment. *Langmuir* **2002**, *18*, 10261-10273.

(106) Talu, O.; Myers, A. L. Molecular simulation of adsorption: Gibbs dividing surface and comparison with experiment. *AIChE Journal* **2001**, *47*, 1160-1168.

(107) Alaerts, L.; Maes, M.; Giebeler, L.; Jacobs, P. A.; Martens, J. A.; Denayer, J. F. M.; Kirschhock, C. E. A.; De Vos, D. E. Selective Adsorption and Separation of ortho-Substituted Alkylaromatics with the Microporous Aluminum Terephthalate MIL-53. *Journal of the American Chemical Society* **2008**, *130*, 14170-14178.

(108) Kim, S.-N.; Kim, J.; Kim, H.-Y.; Cho, H.-Y.; Ahn, W.-S. Adsorption/catalytic properties of MIL-125 and NH2-MIL-125. *Catalysis Today* **2013**, *204*, 85-93.

(109) Guillerm, V.; Ragon, F.; Dan-Hardi, M.; Devic, T.; Vishnuvarthan, M.; Campo, B.; Vimont, A.; Clet, G.; Yang, Q.; Maurin, G., et al. A Series of Isoreticular, Highly Stable, Porous Zirconium Oxide Based Metal–Organic Frameworks. *Angewandte Chemie International Edition* **2012**, *51*, 9267-9271.

(110) Phan, A.; Czaja, A. U.; Gándara, F.; Knobler, C. B.; Yaghi, O. M. Metal–Organic Frameworks of Vanadium as Catalysts for Conversion of Methane to Acetic Acid. *Inorganic Chemistry* **2011**, *50*, 7388-7390.

(111) Beerdsen, E.; Smit, B.; Dubbeldam, D. Molecular Simulation of Loading Dependent Slow Diffusion in Confined Systems. *Physical Review Letters* **2004**, *93*, 248301.

(112) Czaja, A. U.; Trukhan, N.; Müller, U. Industrial applications of metal–organic frameworks. *Chemical Society Reviews* **2009**, *38*, 1284-1293.

(113) Ferey, G. Hybrid porous solids: past, present, future. *Chem Soc Rev* **2008**, *37*, 191-214.

(114) Mueller, U.; Schubert, M.; Teich, F.; Puetter, H.; Schierle-Arndt, K.; Pastre, J. Metal–organic frameworks—prospective industrial applications. *J. Mater. Chem.* **2005**, *16*, 626-636.

(115) Watanabe, T.; Sholl, D. S. Accelerating Applications of Metal–Organic Frameworks for Gas Adsorption and Separation by Computational Screening of Materials. *Langmuir* **2012**, *28*, 14114-14128.

(116) Ma, L.; Abney, C.; Lin, W. Enantioselective catalysis with homochiral metal–organic frameworks. *Chemical Society Reviews* **2009**, *38*, 1248-1256.

(117) Seo, J. S.; Whang, D.; Lee, H.; Jun, S. I.; Oh, J.; Jeon, Y. J.; Kim, K. A homochiral metal-organic porous material for enantioselective separation and catalysis. *Nature* **2000**, *404*, 982-986.

(118) Vilhelmsen, L. B.; Walton, K. S.; Sholl, D. S. Structure and Mobility of Metal Clusters in MOFs: Au, Pd, and AuPd Clusters in MOF-74. *Journal of the American Chemical Society* **2012**, *134*, 12807-12816.

(119) Park, K. S.; Ni, Z.; Côté, A. P.; Choi, J. Y.; Huang, R.; Uribe-Romo, F. J.; Chae, H. K.; O'Keeffe, M.; Yaghi, O. M. Exceptional chemical and thermal stability of zeolitic imidazolate frameworks. *Proceedings of the National Academy of Sciences* **2006**, *103*, 10186-10191.

(120) Bux, H.; Chmelik, C.; van Baten, J. M.; Krishna, R.; Caro, J. Novel MOF-Membrane for Molecular Sieving Predicted by IR-Diffusion Studies and Molecular Modeling. *Advanced Materials* **2010**, *22*, 4741-4743.

(121) McCarthy, M. C.; Varela-Guerrero, V.; Barnett, G. V.; Jeong, H.-K. Synthesis of Zeolitic Imidazolate Framework Films and Membranes with Controlled Microstructures. *Langmuir* **2010**, *26*, 14636-14641.

(122) Ordoñez, M. J. C.; Balkus Jr, K. J.; Ferraris, J. P.; Musselman, I. H. Molecular sieving realized with ZIF-8/Matrimid® mixed-matrix membranes. *Journal of Membrane Science* **2010**, *361*, 28-37.

(123) Luebbers, M. T.; Wu, T.; Shen, L.; Masel, R. I. Effects of Molecular Sieving and Electrostatic Enhancement in the Adsorption of Organic Compounds on the Zeolitic Imidazolate Framework ZIF-8. *Langmuir* **2010**, *26*, 15625-15633.

(124) Venna, S. R.; Carreon, M. A. Highly Permeable Zeolite Imidazolate Framework-8 Membranes for CO2/CH4 Separation. *Journal of the American Chemical Society* **2009**, *132*, 76-78.

(125) Amrouche, H.; Aguado, S.; Pérez-Pellitero, J.; Chizallet, C. l.; Siperstein, F.; Farrusseng, D.; Bats, N.; Nieto-Draghi, C. Experimental and Computational Study of Functionality Impact on Sodalite–Zeolitic Imidazolate Frameworks for CO2 Separation. *The Journal of Physical Chemistry C* **2011**, *115*, 16425-16432.

(126) Bux, H.; Liang, F.; Li, Y.; Cravillon, J.; Wiebcke, M.; Caro, J. r. Zeolitic Imidazolate Framework Membrane with Molecular Sieving Properties by Microwave-Assisted Solvothermal Synthesis. *Journal of the American Chemical Society* **2009**, *131*, 16000-16001.

(127) Amrouche, H.; Creton, B.; Siperstein, F.; Nieto-Draghi, C. Prediction of thermodynamic properties of adsorbed gases on Zeolitic Imidazolate frameworks. *RSC Advances* **2012**.

(128) Küsgens, P.; Rose, M.; Senkovska, I.; Fröde, H.; Henschel, A.; Siegle, S.; Kaskel, S. Characterization of metal-organic frameworks by water adsorption. *Microporous and Mesoporous Materials* **2009**, *120*, 325-330.

(129) Diestel, L.; Bux, H.; Wachsmuth, D.; Caro, J. Pervaporation studies of n-hexane, benzene, mesitylene and their mixtures on zeolitic imidazolate framework-8 membranes. *Microporous and Mesoporous Materials* **2012**, *164*, 288-293.

(130) Cousin Saint Remi, J.; Rémy, T.; Van Hunskerken, V.; van de Perre, S.; Duerinck, T.; Maes, M.; De Vos, D.; Gobechiya, E.; Kirschhock, C. E. A.; Baron, G. V., et al. Biobutanol Separation with the Metal–Organic Framework ZIF-8. *ChemSusChem* **2011**, *4*, 1074-1077.

(131) Chizallet, C.; Lazare, S.; Bazer-Bachi, D.; Bonnier, F.; Lecocq, V.; Soyer, E.; Quoineaud, A.-A.; Bats, N. Catalysis of Transesterification by a Nonfunctionalized Metal−Organic Framework: Acido-Basicity at the External Surface of ZIF-8 Probed by FTIR and ab Initio Calculations. *Journal of the American Chemical Society* **2010**, *132*, 12365-12377.

(132) Tran, U. P. N.; Le, K. K. A.; Phan, N. T. S. Expanding Applications of Metal−Organic Frameworks: Zeolite Imidazolate Framework ZIF-8 as an Efficient Heterogeneous Catalyst for the Knoevenagel Reaction. *ACS Catalysis* **2011**, *1*, 120-127.

(133) Pan, L.; Parker, B.; Huang, X.; Olson, D. H.; Lee; Li, J. Zn(tbip) (H2tbip= 5-tert-Butyl Isophthalic Acid): A Highly Stable Guest-Free Microporous Metal Organic Framework with Unique Gas Separation Capability. *Journal of the American Chemical Society* **2006**, *128*, 4180-4181.

(134) Lee, J. Y.; Olson, D. H.; Pan, L.; Emge, T. J.; Li, J. Microporous Metal–Organic Frameworks with High Gas Sorption and Separation Capacity. *Advanced Functional Materials* **2007**, *17*, 1255-1262.

(135) Düren, T.; Bae, Y. S.; Snurr, R. Q. Using molecular simulation to characterise metal–organic frameworks for adsorption applications. *Chemical Society Reviews* **2009**, *38*, 1237-1247.

(136) Nalaparaju, A.; Zhao, X. S.; Jiang, J. W. Molecular Understanding for the Adsorption of Water and Alcohols in Hydrophilic and Hydrophobic Zeolitic Metal−Organic Frameworks. *The Journal of Physical Chemistry C* **2010**, *114*, 11542-11550.

(137) Phan, A.; Doonan, C. J.; Uribe-Romo, F. J.; Knobler, C. B.; O'Keeffe, M.; Yaghi, O. M. Synthesis, Structure, and Carbon Dioxide Capture Properties of Zeolitic Imidazolate Frameworks. *Accounts of Chemical Research* **2009**, *43*, 58-67.

(138) Zhu, G.; Borjigin, T.; Sun, F.; Ren, H.; Cai, K.; Zhang, J. A Microporous Metal-Organic Framework with High Stability for GC Separation of Alcohols from Water. *Chemical Communications* **2012**.

(139) Stallmach, F.; Gröger, S.; Künzel, V.; Kärger, J.; Yaghi, O. M.; Hesse, M.; Müller, U. NMR Studies on the Diffusion of Hydrocarbons on the Metal-Organic Framework Material MOF-5. *Angewandte Chemie International Edition* **2006**, *45*, 2123-2126.

(140) Sholl, D. S. Understanding Macroscopic Diffusion of Adsorbed Molecules in Crystalline Nanoporous Materials via Atomistic Simulations. *Accounts of Chemical Research* **2006**, *39*, 403-411.

(141) Ford, D. C.; Dubbeldam, D.; Snurr, R. Q. The Effect of Framework Flexibility on Diffusion of Small Molecules in the Metal-Organic Framework IRMOF-1. *Diffusion-fundamentals. org* **2009**, *11*.

(142) Yashonath, S.; Santikary, P. Diffusion of Sorbates in Zeolites Y and A: Novel Dependence on Sorbate Size and Strength of Sorbate-Zeolite Interaction. *The Journal of Physical Chemistry* **1994**, *98*, 6368-6376.

(143) Leroy, F.; Rousseau, B.; Fuchs, A. Self-diffusion of n-alkanes in silicalite using molecular dynamics simulation: A comparison between rigid and flexible frameworks. *Phys. Chem. Chem. Phys.* **2004**, *6*, 775-783.

(144) Bouyermaouen, A.; Bellemans, A. Molecular dynamics simulation of the diffusion of n-butane and i-butane in silicalite. *The Journal of chemical physics* **1998**, *108*, 2170-2172.

(145) Férey, G.; Serre, C. Large breathing effects in three-dimensional porous hybrid matter: facts, analyses, rules and consequences. *Chemical Society Reviews* **2009**, *38*, 1380-1399.

(146) Uemura, K.; Matsuda, R.; Kitagawa, S. Flexible microporous coordination polymers. *Journal of Solid State Chemistry* **2005**, *178*, 2420-2429.

(147) Fletcher, A. J.; Thomas, K. M.; Rosseinsky, M. J. Flexibility in metal-organic framework materials: Impact on sorption properties. *Journal of Solid State Chemistry* **2005**, *178*, 2491-2510.

(148) Zhang, C.; Lively, R. P.; Zhang, K.; Johnson, J. R.; Karvan, O.; Koros, W. J. Unexpected Molecular Sieving Properties of Zeolitic Imidazolate Framework-8. *The Journal of Physical Chemistry Letters* **2012**, *3*, 2130-2134.

(149) Haldoupis, E.; Watanabe, T.; Nair, S.; Sholl, D. S. Quantifying Large Effects of Framework Flexibility on Diffusion in MOFs: CH4 and CO2 in ZIF-8. *ChemPhysChem* **2012**, *13*, 3449-3452.

(150) Allen, F. The Cambridge Structural Database: a quarter of a million crystal structures and rising. *Acta Crystallographica Section B* **2002**, *58*, 380-388.

(151) Kresse, G.; Hafner, J. Ab initio molecular dynamics for liquid metals. *Physical Review B* **1993**, *47*, 558.

(152) Perdew, J. P.; Emzerhof, M.; Burke, K. Rationale for Mixing Exact Exchange with Density-Functional Approximations. *Journal of Chemical Physics* **1996**, *105*, 9982-9985.

(153) Wang, J.; Wolf, R. M.; Caldwell, J. W.; Kollman, P. A.; Case, D. A. Development and testing of a general amber force field. *Journal of Computational Chemistry* **2004**, *25*, 1157-1174.

(154) Chen, B.; Potoff, J. J.; Siepmann, J. I. Monte Carlo Calculations for Alcohols and Their Mixtures with Alkanes. Transferable Potentials for Phase Equilibria. 5. United-Atom Description of Primary, Secondary, and Tertiary Alcohols. *The Journal of Physical Chemistry B* **2001**, *105*, 3093-3104.

(155) Gupta, A.; Chempath, S.; Sanborn, M. J.; Clark, L. A.; Snurr, R. Q. Object-oriented Programming Paradigms for Molecular Modeling. *Molecular Simulation* **2003**, *29*, 29-46.

(156) Wolf, D.; Keblinski, P.; Phillpot, S.; Eggebrecht, J. Exact method for the simulation of Coulombic systems by spherically truncated, pairwise r summation. *The Journal of chemical physics* **1999**, *110*, 8254.

(157) Chempath, S.; Clark, L. A.; Snurr, R. Q. Two general methods for grand canonical ensemble simulation of molecules with internal flexibility. *The Journal of chemical physics* **2003**, *118*, 7635-7643.

(158) Plimpton, S. Fast parallel algorithms for short-range molecular dynamics. *Journal of Computational Physics* **1995**, *117*, 1-19.

(159) Allen, M.; Tildesley, D. Oxford University Press; New York: 1987. *Computer Simulation of Liquids*.

(160) Hahn, E. L. Spin Echoes. *Physical Review* **1950**, *80*, 580-594.

(161) Stallmach, F.; Galvosas, P. In *Annual Reports on NMR Spectroscopy*; Webb, G. A., Ed.; Academic Press: 2007; Vol. Volume 61, p 51-131.

(162) Hurle, R. L.; Easteal, A. J.; Woolf, L. A. Self-diffusion in monohydric alcohols under pressure. Methanol, methan(2H)ol and ethanol. *Journal of the Chemical Society, Faraday Transactions 1: Physical Chemistry in Condensed Phases* **1985**, *81*, 769-779.

(163) Chmelik, C.; Bux, H.; Caro, J.; Heinke, L.; Hibbe, F.; Titze, T.; Kärger, J. Mass Transfer in a Nanoscale Material Enhanced by an Opposing Flux. *Physical Review Letters* **2010**, *104*, 085902.

(164) Dean, J. A. *Lange's handbook of chemistry*, 1985.

(165) Joseph, S.; Aluru, N. R. Why Are Carbon Nanotubes Fast Transporters of Water? *Nano Letters* **2008**, *8*, 452-458.

(166) Zang, J.; Chempath, S.; Konduri, S.; Nair, S.; Sholl, D. S. Flexibility of Ordered Surface Hydroxyls Influences the Adsorption of Molecules in Single-Walled Aluminosilicate Nanotubes. *The Journal of Physical Chemistry Letters* **2010**, *1*, 1235-1240.

(167) Hibbe, F.; Chmelik, C.; Heinke, L.; Pramanik, S.; Li, J.; Ruthven, D. M.; Tzoulaki, D.; Kärger, J. The Nature of Surface Barriers on Nanoporous Solids Explored

by Microimaging of Transient Guest Distributions. *Journal of the American Chemical Society* **2011**, *133*, 2804-2807.

(168) Sholl, D. S. Metal-organic frameworks: A porous maze. *Nat Chem* **2011**, *3*, 429-430.

(169) Chmelik, C.; Freude, D.; Bux, H.; Haase, J. Ethene/ethane mixture diffusion in the MOF sieve ZIF-8 studied by MAS PFG NMR diffusometry. *Microporous and Mesoporous Materials* **2012**, *147*, 135-141.

(170) Pan, Y.; Li, T.; Lestari, G.; Lai, Z. Effective separation of propylene/propane binary mixtures by ZIF-8 membranes. *Journal of Membrane Science* **2012**, *390–391*, 93-98.

(171) June, R. L.; Bell, A. T.; Theodorou, D. N. Transition-state studies of xenon and sulfur hexafluoride diffusion in silicalite. *The Journal of Physical Chemistry* **1991**, *95*, 8866-8878.

(172) Banerjee, R.; Phan, A.; Wang, B.; Knobler, C.; Furukawa, H.; O'Keeffe, M.; Yaghi, O. M. High-Throughput Synthesis of Zeolitic Imidazolate Frameworks and Application to CO2 Capture. *Science* **2008**, *319*, 939-943.

(173) Rosi, N. L.; Eddaoudi, M.; Kim, J.; O'Keeffe, M.; Yaghi, O. M. Advances in the chemistry of metal-organic frameworks. *CrystEngComm* **2002**, *4*, 401-404.

(174) Rowsell, J. L. C.; Yaghi, O. M. Metal–organic frameworks: a new class of porous materials. *Microporous and Mesoporous Materials* **2004**, *73*, 3-14.

(175) Wu, H.; Zhou, W.; Yildirim, T. Hydrogen Storage in a Prototypical Zeolitic Imidazolate Framework-8. *Journal of the American Chemical Society* **2007**, *129*, 5314-5315.

(176) Morris, W.; He, N.; Ray, K. G.; Klonowski, P.; Furukawa, H.; Daniels, I. N.; Houndonougbo, Y. A.; Asta, M.; Yaghi, O. M.; Laird, B. B. A Combined Experimental-Computational Study on the Effect of Topology on Carbon Dioxide Adsorption in Zeolitic Imidazolate Frameworks. *The Journal of Physical Chemistry C* **2012**, *116*, 24084-24090.

(177) Millward, A. R.; Yaghi, O. M. Metal−Organic Frameworks with Exceptionally High Capacity for Storage of Carbon Dioxide at Room Temperature. *Journal of the American Chemical Society* **2005**, *127*, 17998-17999.

(178) Dai, Y.; Johnson, J. R.; Karvan, O.; Sholl, D. S.; Koros, W. J. Ultem®/ZIF-8 mixed matrix hollow fiber membranes for CO2/N2 separations. *Journal of Membrane Science* **2012**, *401–402*, 76-82.

(179) Lewis, D. W.; Ruiz-Salvador, A. R.; Gómez, A.; Rodriguez-Albelo, L. M.; Coudert, F.-X.; Slater, B.; Cheetham, A. K.; Mellot-Draznieks, C. Zeolitic imidazole frameworks: structural and energetics trends compared with their zeolite analogues. *CrystEngComm* **2009**, *11*, 2272-2276.

(180) Hughes, J. T.; Bennett, T. D.; Cheetham, A. K.; Navrotsky, A. Thermochemistry of Zeolitic Imidazolate Frameworks of Varying Porosity. *Journal of the American Chemical Society* **2012**, *135*, 598-601.

(181) Navrotsky, A. Calorimetric insights into the synthesis of templated materials. *Current Opinion in Colloid & Interface Science* **2005**, *10*, 195-202.

(182) Navrotsky, A.; Trofymluk, O.; Levchenko, A. A. Thermochemistry of Microporous and Mesoporous Materials. *Chemical Reviews (Washington, DC, United States)* **2009**, *109*, 3885-3902.

(183) Baburin, I. A.; Leoni, S. The energy landscapes of zeolitic imidazolate frameworks (ZIFs): towards quantifying the presence of substituents on the imidazole ring. *Journal of Materials Chemistry* **2012**, *22*, 10152-10154.

(184) Demuth, T.; Jeanvoine, Y.; Hafner, J.; Angyan, J. Polymorphism in silica studied in the local density and generalized-gradient approximations. *Journal of Physics: Condensed Matter* **1999**, *11*, 3833.

(185) Teter, D. M.; Gibbs, G. V.; Boisen, M. B., Jr.; Allan, D. C.; Teter, M. P. First-principles study of several hypothetical silica framework structures. *Physical Review B* **1995**, *52*, 8064-8073.

(186) Astala, R.; Auerbach, S. M.; Monson, P. A. Density Functional Theory Study of Silica Zeolite Structures: Stabilities and Mechanical Properties of SOD, LTA, CHA, MOR, and MFI. *The Journal of Physical Chemistry B* **2004**, *108*, 9208-9215.

(187) Baburin, I. A.; Leoni, S.; Seifert, G. Enumeration of Not-Yet-Synthesized Zeolitic Zinc Imidazolate MOF Networks: A Topological and DFT Approach. *The Journal of Physical Chemistry B* **2008**, *112*, 9437-9443.

(188) Henson, N. J.; Cheetham, A. K.; Gale, J. D. Theoretical calculations on silica frameworks and their correlation with experiment. *Chemistry of Materials* **1994**, *6*, 1647-1650.

(189) Gale, J. D. Analytical Free Energy Minimization of Silica Polymorphs. *The Journal of Physical Chemistry B* **1998**, *102*, 5423-5431.

(190) Ford, M. H.; Auerbach, S. M.; Monson, P. A. On the mechanical properties and phase behavior of silica: A simple model based on low coordination and strong association. *The Journal of Chemical Physics* **2004**, *121*, 8415-8422.

(191) Ford, M. H.; Auerbach, S. M.; Monson, P. A. Further studies of a simple atomistic model of silica: Thermodynamic stability of zeolite frameworks as silica polymorphs. *The Journal of Chemical Physics* **2007**, *126*, 144701.

(192) Amirjalayer, S.; Snurr, R. Q.; Schmid, R. Prediction of Structure and Properties of Boron-Based Covalent Organic Frameworks by a First-Principles Derived Force Field. *The Journal of Physical Chemistry C* **2012**, *116*, 4921-4929.

(193) Hughes, J. T.; Navrotsky, A. MOF-5: Enthalpy of Formation and Energy Landscape of Porous Materials. *Journal of the American Chemical Society* **2011**, *133*, 9184-9187.

(194) Amirjalayer, S.; Tafipolsky, M.; Schmid, R. Exploring Network Topologies of Copper Paddle Wheel Based Metal–Organic Frameworks with a First-Principles Derived Force Field. *The Journal of Physical Chemistry C* **2011**, *115*, 15133-15139.

(195) Cravillon, J.; Münzer, S.; Lohmeier, S.-J.; Feldhoff, A.; Huber, K.; Wiebcke, M. Rapid Room-Temperature Synthesis and Characterization of Nanocrystals of a Prototypical Zeolitic Imidazolate Framework. *Chemistry of Materials* **2009**, *21*, 1410-1412.

(196) Pan, Y.; Liu, Y.; Zeng, G.; Zhao, L.; Lai, Z. Rapid synthesis of zeolitic imidazolate framework-8 (ZIF-8) nanocrystals in an aqueous system. *Chemical Communications (Cambridge, United Kingdom)* **2011**, *47*, 2071-2073.

(197) Coudert, F.-X.; Jeffroy, M.; Fuchs, A. H.; Boutin, A.; Mellot-Draznieks, C. Thermodynamics of Guest-Induced Structural Transitions in Hybrid Organic−Inorganic Frameworks. *Journal of the American Chemical Society* **2008**, *130*, 14294-14302.

(198) Brennan, J. K.; Madden, W. G. Phase Coexistence Curves for Off-Lattice Polymer−Solvent Mixtures: Gibbs-Ensemble Simulations. *Macromolecules* **2002**, *35*, 2827-2834.

(199) Banaszak, B. J.; Faller, R.; de Pablo, J. J. Simulation of the effects of chain architecture on the sorption of ethylene in polyethylene. *The Journal of Chemical Physics* **2004**, *120*, 11304-11315.

(200) Shen, J.; Monson, P. A. A molecular model of adsorption in a dilute semiflexible porous network. *Molecular Physics* **2002**, *100*, 2031-2039.

(201) Jeffroy, M.; Fuchs, A. H.; Boutin, A. Structural changes in nanoporous solids due to fluid adsorption: thermodynamic analysis and Monte Carlo simulations. *Chemical Communications (Cambridge, United Kingdom)* **2008**, *0*, 3275-3277.

(202) Coudert, F.-X.; Mellot-Draznieks, C.; Fuchs, A. H.; Boutin, A. Prediction of Breathing and Gate-Opening Transitions Upon Binary Mixture Adsorption in Metal−Organic Frameworks. *Journal of the American Chemical Society* **2009**, *131*, 11329-11331.

(203) Coudert, F.-X. The osmotic framework adsorbed solution theory: predicting mixture coadsorption in flexible nanoporous materials. *Physical Chemistry Chemical Physics* **2010**, *12*, 10904-10913.

(204) Gee, J. A.; Chung, J.; Nair, S.; Sholl, D. S. Adsorption and Diffusion of Small Alcohols in Zeolitic Imidazolate Frameworks ZIF-8 and ZIF-90. *The Journal of Physical Chemistry C* **2013**, *117*, 3169-3176.

(205) Straatsma, T. P.; Berendsen, H. J. C. Free energy of ionic hydration: Analysis of a thermodynamic integration technique to evaluate free energy differences by molecular dynamics simulations. *The Journal of Chemical Physics* **1988**, *89*, 5876-5886.

(206) Frenkel, D.; Smit, B.; Ratner, M. A. Understanding molecular simulation: from algorithms to applications. *Physics Today* **1997**, *50*, 66.

(207) Shirts, M. R.; Pitera, J. W.; Swope, W. C.; Pande, V. S. Extremely precise free energy calculations of amino acid side chain analogs: Comparison of common molecular mechanics force fields for proteins. *The Journal of Chemical Physics* **2003**, *119*, 5740.

(208) Redmill, P. S.; Capps, S. L.; Cummings, P. T.; McCabe, C. A molecular dynamics study of the Gibbs free energy of solvation of fullerene particles in octanol and water. *Carbon* **2009**, *47*, 2865-2874.

(209) Johnson, R. R.; Johnson, A. T. C.; Klein, M. L. The Nature of DNA-Base–Carbon-Nanotube Interactions. *Small* **2010**, *6*, 31-34.

(210) Kirkwood, J. G. Statistical Mechanics of Fluid Mixtures. *The Journal of Chemical Physics* **1935**, *3*, 300-313.

(211) Duane, S.; Kennedy, A. D.; Pendleton, B. J.; Roweth, D. Hybrid monte carlo. *Physics Letters B* **1987**, *195*, 216-222.

(212) Pohorille, A.; Jarzynski, C.; Chipot, C. Good Practices in Free-Energy Calculations. *The Journal of Physical Chemistry B* **2010**, *114*, 10235-10253.

(213) Beutler, T. C.; Mark, A. E.; van Schaik, R. C.; Gerber, P. R.; van Gunsteren, W. F. Avoiding singularities and numerical instabilities in free energy calculations based on molecular simulations. *Chemical Physics Letters* **1994**, *222*, 529-539.

(214) Zacharias, M.; Straatsma, T.; McCammon, J. Separation-shifted scaling, a new scaling method for Lennard-Jones interactions in thermodynamic integration. *Journal of Chemical Physics* **1994**, *100*, 9025-9031.

(215) van der Spoel, D.; Lindahl, E.; Hess, B.; Van Buuren, A.; Apol, E.; Meulenhoff, P.; Tieleman, D.; Sijbers, A.; Feenstra, K.; van Drunen, R. *Gromacs User manual version 3.3*, 2008.

(216) Myers, A. L. Thermodynamics of adsorption in porous materials. *AIChE Journal* **2002**, *48*, 145-160.

(217) Zang, J.; Nair, S.; Sholl, D. S. Osmotic ensemble methods for predicting adsorption-induced structural transitions in nanoporous materials using molecular simulations. *The Journal of Chemical Physics* **2011**, *134*, 184103.

(218) Pastorino, C.; Gamba, Z. Free-energy calculations of elemental sulphur crystals via molecular dynamics simulations. *The Journal of Chemical Physics* **2003**, *119*, 2147-2154.

(219) Born, M.; Huang, K.; Britain, G. *Dynamical theory of crystal lattices*; Clarendon Press Oxford, 1954.

(220) Humphrey, W.; Dalke, A.; Schulten, K. VMD: visual molecular dynamics. *Journal of Molecular Graphics* **1996**, *14*, 33-38.

(221) Mayo, S. L.; Olafson, B. D.; Goddard, W. A. DREIDING: a generic force field for molecular simulations. *Journal of Physical Chemistry* **1990**, *94*, 8897-8909.

(222) Bhunia, M. K.; Hughes, J. T.; Fettinger, J. C.; Navrotsky, A. Thermochemistry of Paddle Wheel MOFs: Cu-HKUST-1 and Zn-HKUST-1. *Langmuir* **2013**, *29*, 8140-8145.

(223) Jain, P. K.; Huang, X. H.; El-Sayed, I. H.; El-Sayed, M. A. Noble Metals on the Nanoscale: Optical and Photothermal Properties and Some Applications in Imaging, Sensing, Biology, and Medicine. *Accounts of Chemical Research* **2008**, *41*, 1578-1586.

(224) Osada, M.; Sasaki, T. Two-Dimensional Dielectric Nanosheets: Novel Nanoelectronics From Nanocrystal Building Blocks. *Advanced Materials* **2012**, *24*, 210-228.

(225) Podsiadlo, P.; Kaushik, A. K.; Arruda, E. M.; Waas, A. M.; Shim, B. S.; Xu, J. D.; Nandivada, H.; Pumplin, B. G.; Lahann, J.; Ramamoorthy, A., et al. Ultrastrong and stiff layered polymer nanocomposites. *Science* **2007**, *318*, 80-83.

(226) Roldan Cuenya, B. Metal Nanoparticle Catalysts Beginning to Shape-up. *Accounts of Chemical Research* **2012**, *46*, 1682-1691.

(227) Zhang, C.; Zhang, K.; Xu, L.; Labreche, Y.; Kraftschik, B.; Koros, W. J. Highly scalable ZIF-based mixed-matrix hollow fiber membranes for advanced hydrocarbon separations. *AIChE Journal* **2014**, *60*, 2625-2635.

(228) Park, K. S.; Ni, Z.; Cote, A. P.; Choi, J. Y.; Huang, R.; Uribe-Romo, F. J.; Chae, H. K.; O'Keeffe, M.; Yaghi, O. M. Exceptional chemical and thermal stability of zeolitic imidazolate frameworks. *Proc. Natl. Acad. Sci. U. S. A.* **2006**, *103*, 10186-10191.

(229) Phan, A.; Doonan, C. J.; Uribe-Romo, F. J.; Knobler, C. B.; O'Keeffe, M.; Yaghi, O. M. Synthesis, Structure, and Carbon Dioxide Capture Properties of Zeolitic Imidazolate Frameworks. *Acc. Chem. Res.* **2010**, *43*, 58-67.

(230) Fairen-Jimenez, D.; Moggach, S. A.; Wharmby, M. T.; Wright, P. A.; Parsons, S.; Duren, T. Opening the Gate: Framework Flexibility in ZIF-8 Explored by Experiments and Simulations. *J. Am. Chem. Soc.* **2011**, *133*, 8900-8902.

(231) Gücüyener, C.; van den Bergh, J.; Gascon, J.; Kapteijn, F. Ethane/Ethene Separation Turned on Its Head: Selective Ethane Adsorption on the Metal−Organic Framework ZIF-7 through a Gate-Opening Mechanism. *Journal of the American Chemical Society* **2010**, *132*, 17704-17706.

(232) Peralta, D.; Chaplais, G.; Simon-Masseron, A.; Barthelet, K.; Chizallet, C.; Quoineaud, A.-A.; Pirngruber, G. D. Comparison of the Behavior of Metal–Organic Frameworks and Zeolites for Hydrocarbon Separations. *Journal of the American Chemical Society* **2012**, *134*, 8115-8126.

(233) Herm, Z. R.; Bloch, E. D.; Long, J. R. Hydrocarbon Separations in Metal–Organic Frameworks. *Chemistry of Materials* **2013**, *26*, 323–338.

(234) Kwon, H. T.; Jeong, H.-K. In Situ Synthesis of Thin Zeolitic–Imidazolate Framework ZIF-8 Membranes Exhibiting Exceptionally High Propylene/Propane Separation. *Journal of the American Chemical Society* **2013**, *135*, 10763-10768.

(235) Zhang, K.; Lively, R. P.; Zhang, C.; Chance, R. R.; Koros, W. J.; Sholl, D. S.; Nair, S. Exploring the Framework Hydrophobicity and Flexibility of ZIF-8: From Biofuel Recovery to Hydrocarbon Separations. *The Journal of Physical Chemistry Letters* **2013**, *4*, 3618-3622.

(236) Sakata, Y.; Furukawa, S.; Kondo, M.; Hirai, K.; Horike, N.; Takashima, Y.; Uehara, H.; Louvain, N.; Meilikhov, M.; Tsuruoka, T., et al. Shape-Memory Nanopores Induced in Coordination Frameworks by Crystal Downsizing. *Science* **2013**, *339*, 193-196.

(237) Kumari, G.; Jayaramulu, K.; Maji, T. K.; Narayana, C. Temperature Induced Structural Transformations and Gas Adsorption in the Zeolitic Imidazolate Framework ZIF-8: A Raman Study. *The Journal of Physical Chemistry A* **2013**, *117*, 11006-11012.

(238) Bennett, T. D.; Tan, J.-C.; Moggach, S. A.; Galvelis, R.; Mellot-Draznieks, C.; Reisner, B. A.; Thirumurugan, A.; Allan, D. R.; Cheetham, A. K. Mechanical Properties of Dense Zeolitic Imidazolate Frameworks (ZIFs): A High-Pressure X-ray Diffraction, Nanoindentation and Computational Study of the Zinc Framework Zn(Im)2, and its Lithium-Boron Analogue, LiB(Im)4. *Chemistry – A European Journal* **2010**, *16*, 10684-10690.

(239) Haldoupis, E.; Watanabe, T.; Nair, S.; Sholl, D. S. Quantifying Large Effects of Framework Flexibility on Diffusion in MOFs: CH4 and CO2 in ZIF-8. *ChemPhysChem* **2012**, *13*, 3449-3452.

(240) Hu, Z.; Zhang, L.; Jiang, J. Development of a force field for zeolitic imidazolate framework-8 with structural flexibility. *The Journal of Chemical Physics* **2012**, *136*, 244703.

(241) Zheng, B.; Sant, M.; Demontis, P.; Suffritti, G. B. Force Field for Molecular Dynamics Computations in Flexible ZIF-8 Framework. *The Journal of Physical Chemistry C* **2012**, *116*, 933-938.

(242) Zhang, L.; Hu, Z.; Jiang, J. Sorption-Induced Structural Transition of Zeolitic Imidazolate Framework-8: A Hybrid Molecular Simulation Study. *Journal of the American Chemical Society* **2013**, *135*, 3722-3728.

(243) Coudert, F. X.; Boutin, A.; Fuchs, A. H.; Neimark, A. V. Adsorption Deformation and Structural Transitions in Metal–Organic Frameworks: From the Unit Cell to the Crystal. *The Journal of Physical Chemistry Letters* **2013**, *4*, 3198-3205.

(244) Gee, J. A.; Sholl, D. S. Characterization of the Thermodynamic Stability of Solvated Metal–Organic Framework Polymorphs Using Molecular Simulations. *The Journal of Physical Chemistry C* **2013**, *117*, 20636-20642.

(245) Triguero, C.; Coudert, F.-X.; Boutin, A.; Fuchs, A. H.; Neimark, A. V. Understanding adsorption-induced structural transitions in metal-organic frameworks: From the unit cell to the crystal. *The Journal of Chemical Physics* **2012**, *137*, 184702.

(246) Chizallet, C.; Lazare, S.; Bazer-Bachi, D.; Bonnier, F.; Lecocq, V.; Soyer, E.; Quoineaud, A.-A.; Bats, N. Catalysis of Transesterification by a Nonfunctionalized Metal− Organic Framework: Acido-Basicity at the External Surface of ZIF-8 Probed by FTIR and ab Initio Calculations. *Journal of the American Chemical Society* **2010**, *132*, 12365-12377.

(247) Lively, R. P.; Dose, M. E.; Thompson, J. A.; McCool, B. A.; Chance, R. R.; Koros, W. J. Ethanol and water adsorption in methanol-derived ZIF-71. *Chemical Communications* **2011**, *47*, 8667-8669.

(248) Dubbeldam, D.; Calero, S.; Ellis, D.; Snurr, R. RASPA 1.0; Northwestern University: Evanston, IL, 2008.

(249) Leofanti, G.; Padovan, M.; Tozzola, G.; Venturelli, B. Surface area and pore texture of catalysts. *Catalysis Today* **1998**, *41*, 207-219.

(250) Walton, K. S.; Snurr, R. Q. Applicability of the BET Method for Determining Surface Areas of Microporous Metal−Organic Frameworks. *Journal of the American Chemical Society* **2007**, *129*, 8552-8556.

(251) Ania, C. O.; García-Pérez, E.; Haro, M.; Gutiérrez-Sevillano, J. J.; Valdés-Solís, T.; Parra, J. B.; Calero, S. Understanding Gas-Induced Structural Deformation of ZIF-8. *The Journal of Physical Chemistry Letters* **2012**, *3*, 1159-1164.

(252) Torres-Knoop, A.; Balaji, S. P.; Vlugt, T. J. H.; Dubbeldam, D. A Comparison of Advanced Monte Carlo Methods for Open Systems: CFCMC vs CBMC. *Journal of Chemical Theory and Computation* **2014**, *10*, 942-952.

(253) Bludský, O.; Rubeš, M.; Soldán, P.; Nachtigall, P. Investigation of the benzene-dimer potential energy surface: DFT/CCSD(T) correction scheme. *The Journal of Chemical Physics* **2008**, *128*, 114102.

(254) Dybtsev, D. N.; Chun, H.; Kim, K. Rigid and Flexible: A Highly Porous Metal–Organic Framework with Unusual Guest-Dependent Dynamic Behavior. *Angewandte Chemie* **2004**, *116*, 5143-5146.

(255) Cavka, J. H.; Jakobsen, S.; Olsbye, U.; Guillou, N.; Lamberti, C.; Bordiga, S.; Lillerud, K. P. A New Zirconium Inorganic Building Brick Forming Metal Organic Frameworks with Exceptional Stability. *Journal of the American Chemical Society* **2008**, *130*, 13850-13851.

(256) Eddaoudi, M.; Kim, J.; Rosi, N.; Vodak, D.; Wachter, J.; O'Keeffe, M.; Yaghi, O. M. Systematic design of pore size and functionality in isoreticular MOFs and their application in methane storage. *Science* **2002**, *295*, 469-472.